TsAGI
SCIENCE JOURNAL

EDITOR-IN CHIEF

S.L. CHERNYSHEV

AIMS AND SCOPE

TsAGI Science Journal is a bimonthly publication that includes translations from the Central Aerohydrodynamic Institute which was established under the name of Professor N.E. Zhukovsky.

This journal publishes scholarly work that is submitted by the staff at TsAGI. Material is also accepted from other organizations in the areas of mechanics and control processes in the framework of fundamental problems, problems in the progress of aviation and cosmonautics, industrial aerodynamic, and hydrodynamics of rapid motion. One of the main undertakings for the present edition of the journal is the publication of methods which can be the basis for effective engineering computation and design. Essential topics for this journal are physical and mathematical modeling of real processes, numerical methods and algorithms, and optimization problems. Topics can also relate to corresponding problems in aerodynamics as well as hydrodynamics of high-speed motion, problems of flight mechanics and fluid mechanics, plasma mechanics, deformation mechanics, stability, vibration of bodies and constructions under various influences such as aerohydrodynamic, thermal, and others.

TsAGI Science Journal is intended to be of interest and use to scientists and engineers.

TsAGI Science Journal

TsAGI
SIENCE JOURNAL

CONTENTS

MIL L. MIKHAIL AND TSAGI

On November 22, 2009, 100 years had passed since the birth of the outstanding Russian scientist and helicopter designer M. L. Mil. During the period 1947 to 1970, first as design manager and then chief designer, Mikhail L. Mil was at the forefront in the engineering of outstanding helicopters, civil and military helicopters of the mark "Mi". Developed by the experimental design office (EDO), these helicopters are known all over the world and are in great demand on the domestic and foreign market. More than 90% of the helicopters currently produced in Russia are the "Mi" helicopters, having the basic design laid out by M. L. Mil. In Soviet times the "Mi" helicopters exceeded the helicopters of other countries by total capacity.

M. L. Mil was closely related to TsAGI throughout his extraordinarily creative career in the pursuit of multifaceted research interests.

GYROCOPTERS

Mikhail Mil, being a student of the Faculty of Aerodynamics of Novocherkassk Polytechnic Institute, was absorbed by the theory and practice of gyrocopter creation and studied with interest all the available works on the issue. In 1929 he wrote a letter to Nikolay I. Kamov, a known designer of gyrocopters, in which he demonstrated deep knowledge in this area, requesting a position which would allow him to work under his supervision during the student holidays. His request was granted. That summer he worked as an assistant engineer on the flight tests of the gyrocopter KASKR-1 of Kamov and Skrzhinsky design. In 1930 M. Mil, although he was currently in Taganrog, requested that he perform his pregraduation practical work at the Department of Experimental Aerodynamics of TsAGI, and in 1931 he began working in this department as a full staffer. His assignment was to perform calculations and experimental investigations with regard to gyrocopter aerodynamics. In 1933 the gyrocopter section in the Department of Experimental Aerodynamics was reorganized under the Department of Special Design of TsAGI, which was engaged in the design of helicopters and gyrocopters. Mikhail Mil was appointed head of the gyrocopter aerodynamic calculation team in the Department of Special Design.

Throughout 1940 a number of TsAGI gyrocopters were designed and constructed at the Department of Special Design. All these works were performed by Mil's team. But Mil was not restricted to the implementation of aerodynamic research, computational investigations, and wind tunnel tests; he literally "was in on" all the questions related to the development, flight test support, design, and construction. Thus, while developing the A-6, "ground resonance" type self-oscillations were successfully eliminated with

the active participation of Mil. These works successfully combined the talents of two outstanding scientists—V. A. Kuznetsov and M. L. Mil.

In March 1940 M. L. Mil was employed in factory no. 290 and became the deputy of the design manager N. I. Kamov. He participated in the production and organization of the A-7 gyrocopters used in the battles of Yelnya in August–September 1941, for which he was awarded the Order of Red Star and other medals.

AIRCRAFTS

In May 1943 M. L. Mil returned to TsAGI, where neither gyrocopter nor helicopter research and design existed at that time. Organized at the recommendation of I. V. Ostoslavskiy in laboratory no. 1 was the Aircraft Stability and Control Group. Mil had begun to study these issues in 1940. The vast experience he gained during his works on gyrocopters proved useful to him. In his role as chief of the Aircraft Stability and Control Group in laboratory no. 1 of TsAGI, Mil focused not only on control simplification and improvement of pilot comfort, but he also directed his efforts toward aircraft combat applications—increasing the accuracy of aircraft shooting and bombing—which was, of course, of special interest in wartime.

Theoretical analysis of the perturbed motion of the aircraft upon entrance to gusts and the definition of loads on the controls were carried out. The requirements to the loads on the control stick were formulated for the weakly stable aircraft in order "to connect" the pilot with the vehicle. Practical proposals to install special shock dampers on the control stick or springs on the control crank in the longitudinal channel were confirmed experimentally in the T-101 wind tunnel and on real aircrafts in flight tests.

During this period Mil and his colleagues studied the influence of friction in the control circuit on the flight performances of aircrafts in detail. They established that a significant friction in the longitudinal or transverse control channel was perceived by the pilot as a reduction of the longitudinal or, respectively, lateral aircraft stability and resulted in a decrease of the controllability estimation of the maneuverable aircrafts. Recommendations were made regarding acceptable friction force values in the control systems of different aircrafts, as well as acceptable relations between the value of friction forces and the gradient of load growth by the stick deflection, providing regular aircraft controllability. Standardized instructions on friction control in the aircraft control system were developed.

All these investigations were aimed at improving the lift-to-drag ratio of the serial military vehicles I-16, DB-3 (Il-4), SK-1, SK-2, OKO-6 bis, LAGG-3, Pe-2, La-5, and Il-2, which was extremely important during the war. During these years Mil worked closely with aircraft designers S. V. Ilyushin, S. A. Lavochkin, and A. I. Mikoyan. After the war M. L. Mil, as a member of staff, was sent to Germany from where they brought the T-107 wind tunnel which operates at TsAGI at present. In October 1943 M. L. Mil defended his PhD thesis on the issues surrounding aircraft stability and controllability. For his work in this area he was awarded the Order of the Patriotic War of 2nd Class.

HELICOPTERS

After World War II Mil's research focused on rotary wing aircrafts. Based on his works on rotor aerodynamics, in October 1945 he successfully defended his PhD thesis and became the head of the department in laboratory no. 1 of TsAGI, where he assembled a close-knit, like-minded group and aimed the work of his department toward helicopters. Together with V. I. Yaroshenko, in a short time he developed an original method of helicopter aerodynamic calculation based on direct consideration of the vehicle polar. This method was necessary for Mil for practical purposes. On his own initiative he began to develop the experimental three-seat helicopter EG-1 at TsAGI, which was designed in the classical single-rotor scheme with the tail rotor, an M-13 engine, and with an original device performing automatic increase of flight stability. April 9, 1946 this helicopter project was submitted to the Ministry of Aircraft Production Commission, which supported the project but with a number of recommendations.

Based on the decision of the Ministry of Aircraft Production Commission, Mil proposed to build a full-scale helicopter plant for the tests in the T-101 wind tunnel. In accordance with Mil's idea, this plant was created for single-rotor helicopter production, but without devices counteracting the reactive moment from the rotor, gear, and other units. This significantly reduced the time for this plant "conversion" to helicopters.

The laboratory for solving scientific problems related to helicopter construction and aircraft spin was created in 1947 based on the TsAGI T-105 vertical wind tunnel. M. L. Mil was appointed head of the laboratory and its helicopter sector. Of course, Mil's experience working with rotary-wing and aircraft equipment contributed to this decision of joining seemingly different directions. Employees of the helicopter sector (more than 20 people) formed the basis for the future EDO of Mil. Almost none of them had previous experience in the design and construction of rotary-wing equipment. Therefore, Mil's knowledge in the area of aerodynamics, design, and construction of both a vehicle as a whole and its individual units, as well as his experience in flight development of rotary-wing equipment, were overwhelmingly important. The cohesion and purposefulness of like-minded fellows contributed to the fact that in a very short time the full-scale helicopter was built and tested in the T-101 wind tunnel. In the autumn of 1947 the full-scale model of the three-seat helicopter EG-1, created in Mil's laboratory, was approved by the government commission.

December 12, 1947 the Council of Ministers of the USSR adopted a special resolution to create a communications helicopter for the Armed Forces of the USSR. According to this resolution, the design teams of A. S. Yakovlev, I. P. Bratukhin, and M. L. Mil were ordered to create prototypes of the new helicopters; thus, development of the communications helicopter was actually a competition. The resolution also obligated the deputy minister of aircraft production to organize at TsAGI the Experimental Design Office on Helicopters and to approve the design manager of this EDO, M. L. Mil. December 12 is the official date of creation of the EDO named after M. L. Mil. By the end

of July 1948 the EDO was located in the building of the T-105 vertical wind tunnel at TsAGI. It was later relocated in Tushino and after that to 3 Rybinskaya str. at Moscow. But Mil worked at TsAGI part-time until the mid-1950s.

Created under the leadership of M. L. Mil before 1970 were the helicopters Mi-1, Mi-4, Mi-6, Mi-10, V-7 (with the jet drive), Mi-2, Mi-8, Mi-14 (amphibian), V-12, Mi-20 (project), and Mi-24. The research and development for all these helicopters to a greater or lesser degree was carried out at TsAGI.

It should be noted that the close cooperation of TsAGI with EDO was sometimes accompanied by serious discussions on questions of principle. Discussions with regard to the transverse scheme helicopter V-12 were especially hot: TsAGI was in principle against this scheme. But Mil's leadership guided the discussion, ultimately ensuring that the correct decision was made—to proceed with plans to build the vehicle. Being the head of the EDO, M. L. Mil always promoted and advanced the ideas in which he believed. On important issues he was known to lobby the government directly, even making his case personally to Khrushchev. From this point of view, M. L. Mil was not only a designer, but by present standards, an excellent manager.

M. L. Mil's activity at TsAGI since 1943 and after in the EDO was of great importance to the formation and development of Russian science and helicopter engineering schools.

"We have a great future, but we remember our relationship. Conceptually we are the followers of the great Russian school of aerodynamics, founded by Nikolai E. Zhukovsky, and of his disciples B. N. Yuriev and A. M. Cheremukhin. Inherently we came out of TsAGI, and therefore we are related to the science by blood ties..." (From the speech of M. L. Mil on the meeting devoted to the 15th *Anniversary of EDO.)*

APPLICATION OF A NEW MATHEMATICAL TOOL (1D SPECTRAL PORTRAITS OF MATRICES) TO THE PROBLEM OF AEROELASTICITY VIBRATIONS OF TURBINE BLADE CASCADES

S. K. Godunov*, V. B. Kurzin, V. G. Bunkov & M. Sadkane

Sobolev Institute of Mathematics Siberian Branch of the Russian Academy of Sciences 4, Acad. Koptyug avenue, Novosibirsk, 630090, Russia

*Address all correspondence to S. K. Godunov E-mail: godunov@math.nsc.ru

Analysis of possibilities of current conventional programs for definition of the nonsymmetrical matrix spectrum, associated with the problems of dynamic stability in aeroelasticity, was fulfilled. The feature of bending-torsion flutter of a wing with multiple oscillation frequencies near the flutter boundary was educed. The problem of flutter was studied by using the method of dichotomy.

1. INTRODUCTION

Design of integral structures is always based on computations, simulating operations of these structures under certain conditions. Such conditions should be described by the limitations, providing operational efficiency and safety and avoiding structural failure. Admissible errors should be given for the numerical values of the limiting parameters, which guarantee reliability of recommendations, based on the calculations.

In aeroelasticity theory, the computational procedures dealing with spectral analyses of matrices are of great importance. It is well known that the stability criterion is reduced to the following statement: all eigenvalues of definite matrices, obtained during modeling, lie strictly in the left part of the complex plane. A natural question arises: "What accuracy is required for computing these eigenvalues?"

The examples, indicating that there is no clear-cut answer to this question, are presented below. The formulation of the question should be modified according to the classical Lyapunov theory. Based on this theory and on its modern generalizations, an algo-

rithm, using the spectral dichotomy criteria and 1D spectral portraits of matrices, illustrating spectrum fibration, is suggested.

Naturally, the used computational procedures should meet the following requirement: their results must satisfy the guaranteed accuracy estimates. This requirement can be met if standard algorithms included into public-domain software used in engineering computations are based on the following natural postulate.

Postulate: Only those numerical functions $f(A)$ of $N \times N$ or $N \times M$ matrices can be calculated, which satisfy the following inequality: $\|f(A) - f(B)\| \leq \omega \|A - B\|$. Here, $\omega = \omega[\|A\|, f(A)]$ is a known function, independent of N and M (matrix dimensions); $\|A\|$, $\|A - B\|$ are the matrix norms.

An example of admissible functions $\sigma_j(A)$ are the singular values of matrix A,

$$A = QDP^*, \ Q^*Q = I_N, \ P^*P = I_M, \ M < N$$

$$D = \underbrace{\left(\begin{array}{cccc} \sigma_M & 0 & \vdots & 0 \\ 0 & \sigma_{M-1} & \vdots & 0 \\ \cdots & \cdots & \ddots & \cdots \\ 0 & 0 & \vdots & \sigma_M \\ \cdots & \cdots & \cdots & \cdots \\ 0 & 0 & 0 & 0 \end{array} \right)}_{M} \Bigg\rangle N$$

The admissibility follows from the inequality $|\sigma_j(A + B) - \sigma_j(A)| \leq \sigma_{\max}(B) = \|B\|$.

An example of inadmissible functions: $\lambda_j = \lambda_j(A)$ are the eigenvalues of the quadratic $N \times N$ matrix A. This can be understood from the following numerical example with the integer-valued 7×7 matrix C:

$$C = \left(\begin{array}{rrrrrrr} 289 & 2044 & 336 & 128 & 80 & 32 & 16 \\ 1152 & 30 & 1312 & 512 & 288 & 128 & 32 \\ -29 & -1980 & 756 & 384 & 1008 & 224 & 48 \\ 512 & 128 & 640 & 0 & 640 & 512 & 128 \\ 1053 & 2136 & -604 & -384 & -856 & 800 & 108 \\ -287 & 4 & 1712 & -128 & 1968 & -30 & 2032 \\ -2176 & -187 & -1465 & -512 & -441 & -1152 & -189 \end{array} \right)$$

One can try to find its spectrum with the help of some MATLAB procedure, using the standard number representation. For matrices C and C^T, which must have identical spectra, the same procedure will give different results,

$$\begin{aligned}
\lambda_1\left(C\right) &= 6.5824 & \lambda_1\left(C^T\right) &= 8.0444 \\
\lambda_2\left(C\right) &= 4.0313 + 4.3421i & \lambda_2\left(C^T\right) &= 4.9557 + 5.6644i \\
\lambda_3\left(C\right) &= 4.0313 - 4.3421i & \lambda_3\left(C^T\right) &= 4.9557 - 5.6644i \\
\lambda_4\left(C\right) &= -1.4668 + 5.3883i & \lambda_4\left(C^T\right) &= -1.8107 + 7.0037i \\
\lambda_5\left(C\right) &= -1.4668 - 5.3883i & \lambda_5\left(C^T\right) &= -1.8107 - 7.0037i \\
\lambda_6\left(C\right) &= -5.8557 + 2.3387i & \lambda_6\left(C^T\right) &= -7.1672 + 3.0701i \\
\lambda_7\left(C\right) &= -5.8557 - 2.3387i & \lambda_7\left(C^T\right) &= -7.1672 - 3.0701i
\end{aligned}$$

The matrix C is obtained as $C = L^{-1}RL$, where

$$R = \begin{pmatrix}
1 & 2028 & 256 & 128 & 64 & 32 & 16 \\
0 & -2 & 1024 & 512 & 256 & 128 & 32 \\
0 & 0 & 4 & 512 & 1024 & 256 & 64 \\
0 & 0 & 0 & 0 & 512 & 512 & 128 \\
0 & 0 & 0 & 0 & -4 & 1024 & 156 \\
0 & 0 & 0 & 0 & 0 & 2 & 2048 \\
0 & 0 & 0 & 0 & 0 & 0 & -1
\end{pmatrix}$$

$$L = \begin{pmatrix}
1\,0\,0\,0\,0\,0\,0 \\
0\,1\,0\,0\,0\,0\,0 \\
1\,0\,1\,0\,0\,0\,0 \\
0\,0\,0\,1\,0\,0\,0 \\
0\,0\,1\,0\,1\,0\,0 \\
1\,0\,0\,0\,0\,1\,0 \\
0\,1\,1\,0\,1\,0\,1
\end{pmatrix}$$

From here, one can see that the actual eigenvalues of C are

$$\lambda_1 = 0,\ \lambda_2 = -1,\ \lambda_3 = +1,\ \lambda_4 = -2,\ \lambda_5 = +2,\ \lambda_6 = -4,\ \lambda_7 = +4$$

The reason for the demonstrated paradox is as follows. All eigenvalues, computed in MATLAB, are the precise eigenvalues of perturbed matrices appearing in the course of computation rather than those inherent in the matrix C itself. And the spectrum of perturbations of the matrix under consideration covers the entire domain where the computed values lie.

Here is another simple example. Consider 25×25 matrices $A + \omega B$, where

$$A = \begin{pmatrix}
-1 & 10 & & & \text{O} \\
& -1 & 10 & & \\
& & \ddots & \ddots & \\
\text{O} & & & \ddots & 10 \\
& & & & -1
\end{pmatrix}$$

is a two-diagonal matrix, while B has only one nonzero element, equal to unity, and is located in the lower-left corner:

$$B = \begin{pmatrix} 0 & 0 & \vdots & 0 \\ \cdots & \cdots & \ddots & \cdots \\ 0 & 0 & \vdots & 0 \\ 1 & 0 & \vdots & 0 \end{pmatrix}$$

If $\omega = 0$, then the spectrum of $A + \omega B$ lies in the left half-plane; if $\omega = 10 \times 8^{-25} \approx 2.6 \times 10^{-22}$, then the eigenvalues of $A + \omega B$ contain $\lambda = 1/4$.

These examples raise the following question: How should one use Lyapunov theorem, which asserts that the solutions of the system $dx/dt = A \cdot x$ are stable if, and only if, the spectrum of A lies strictly in the left half-plane? The point is that this formulation is, in fact, a vulgarization of the Lyapunov theorem. Lyapunov proved that the constraint $\text{Re}(\lambda_j) < 0$ (for all λ_j) is necessary and sufficient for a positive definite solution $H = H^T > 0$ of the Lyapunov matrix equation $HA + A^*H + C = 0$ to exist for all positive definite $C = C^* > 0$. The Lyapunov function (Hx,x) diminishes with increasing t on the solutions of $\dot{x} = Ax$; hence,

$$\|x(t)\| \leq \sqrt{\|H\| \|H^{-1}\|} \, \|x(0)\|$$

How can one compute the coefficient $\sqrt{\|H\| \|H^{-1}\|}$ [the ratio of the maximal and minimal axes of an Lyapunov ellipsoid, where the trajectory $x(t)$ lies]? This coefficient depends not only on matrix A, but also on the choice of the right part of C in the Lyapunov matrix equation. Therefore, the stability analysis should not only include the solvability of the equation $HA + A^*H + C = 0$, but also introduce some particular C, providing an acceptable value of $\sqrt{\|H\| \|H^{-1}\|}$.

On the basis of these arguments, mentioned in Ref. [1], it was suggested to find H from the equation $HA + A^*H + 2 \|A\| I = 0$ and to take as the characteristics of the stability quality the value of $\kappa = \|H\|$, which ensures the validity of the following estimate:

$$\|x(t)\| \leq \sqrt{\kappa} e^{-t\|A\|/\kappa} \|x(0)\| = \sqrt{\kappa} e^{-t/\tau} \|x(0)\|, \quad \tau = \frac{\kappa}{\|A\|}$$

Here, $\kappa = \kappa(A)$ is the solution of the extremal problem

$$\kappa(A) = \sup_{x(o)} \left\{ \frac{\displaystyle\int_0^\infty \|x(t)\|^2 \, dt}{\displaystyle\int_0^\infty \exp(-2t \|A\|) \|x(0)\|^2 \, dt} \right\}$$

The parameter $\tau = \kappa / \|A\|$ is the characteristic time of solution decay. The inequality $| \kappa (A + B) - \kappa (A)| < 13 \kappa^3 (A) (\|B\| / \|A\|) [\text{this holds if } (\|B\| / \|A\|) < 10^{-\kappa^{-2}}]$ shows that $\kappa = \kappa (A)$ is stable with respect to perturbations of the matrix considered in terms of the postulate formulated above.

It turned out [2, 3] that $H = H(A)$ can be represented as a matrix integral

$$H (A) = \frac{\|A\|}{\pi} \int_{-\infty}^{+\infty} [A^* + i\omega I]^{-1} [A - i\omega I]^{-1} d\omega$$

which makes sense not only for Gourwitz matrices with the spectrum, located strictly in the left half-plane. For the convergence of this integral, only the absence of eigenvalues at the imaginary axis is necessary. The value $\kappa = \|H\|$ can be considered as a criterion of spectral dichotomy with respect to the imaginary axis, a criterion estimating the distance of $\lambda_j (A)$ from this axis, regardless of the number of eigenvalues in the left half-plane and those in the right half-plane.

The curve of the dependence of the dichotomy criterion $\kappa (A - aI)$ on a illustrates spectrum fibration by straight lines $\text{Re}(\lambda) = a$, parallel to the imaginary axis. Examples illustrating the use of such graphs (1D spectral portraits) in some simple problems of aeroelasticity are given below.

The first example, illustrating the use of dichotomy criterion, is a simple flutter model, proposed by TsAGI [4], in which the plate-airfoil is considered as a system with four degrees of freedom. When ignoring the aerodynamic effects, the vibrations of the plate are described by

$$\frac{dx}{dt} = -Gy \qquad\qquad G = \begin{pmatrix} 37.7 & & & O \\ & 169 & & \\ & & 899 & \\ O & & & 1792 \end{pmatrix}$$
$$\frac{dy}{dt} = x$$

Aerodynamic effects are modeled by adding new elements, depending on the flow velocity v to the coefficients of the system. The system acquires the following form:

$$\frac{dx}{dt} = -vDx - (G + v^2 F)y$$

$$\frac{dy}{dt} = x$$

$$D = 0.73 \cdot 10^{-2} \begin{pmatrix} 1 & & & 0 \\ & 1 & & \\ & & 1 & \\ 0 & & & 1 \end{pmatrix}$$

$$F = \begin{pmatrix} 0 & -0.197 \cdot 10^{-2} & 0 & 0 \\ 0.12 \cdot 10^{-3} & 0 & -0.419 \cdot 10^{-2} & 0.171 \cdot 10^{-3} \\ 0 & 0.176 \cdot 10^{-3} & 0 & 0 \\ 0 & -0.154 \cdot 10^{-3} & 0 & 0 \end{pmatrix}$$

Fibration of the spectrum of this system with lines, parallel to the imaginary axis, for different velocities v is shown in Figs. 1a and 1b by the solid curve; the dashed curve shows $\tau = \kappa / \|A\|$. It is convenient to superimpose the spectral zones in one figure with $\mathrm{Re}(\lambda)$ as the abscissa axis and the velocity v as the ordinate. The shaded area in Fig. 1c (internal area, bounded by the dot-and-dashed curve) is the domain of $\mathrm{Re}(\lambda)$ values, such that $\lg \sqrt{\kappa} \geq 3.95$; the external area refers to $\lg \sqrt{\kappa} \geq 3.75$. The middle area, bounded by the white curve, is the domain where $\tau = \kappa / \|A\| \geq 3.75$.

The graphs presented allow one to evaluate the critical flutter velocity, obtained from the computed ratio $\mathrm{Re}(\lambda_j) / \|A\|$ and from the proposed criterion $\kappa(A)$. The admissible error for $\kappa(A)$ should be chosen by analyzing the accuracy of modeling the phe-
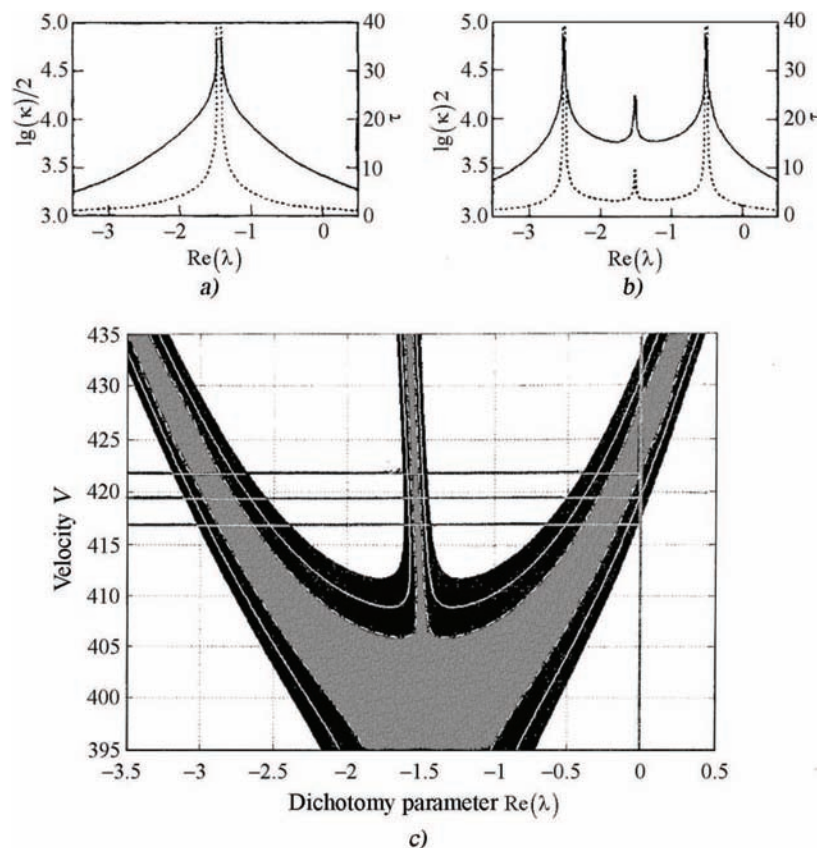
FIG. 1: Spectrum stratification by the straight lines of an imaginary axis at various velocities: (a) $V = 395$ m/s, (b) $V = 411$ m/s, and (c) spectral zones.

nomenon by differential equations and validated against experimental data. Subspaces, corresponding to clusters of eigenvalues (projections onto them or their bases), are computed simultaneously with the spectral portraits. This allows one to indicate the cell-diagonal canonical form of the matrix examined and, by computing the similar transform matrix, find its condition number.

The canonical form of matrix $A(v = 411)$ is

$$Q^{-1}AQ = \begin{pmatrix}
-3.67e+0 & -1.01e+2 & 0 & 0 & 0 & 0 & 0 & 0 \\
1.17e+0 & -1.32e+0 & 0 & 0 & 0 & 0 & 0 & 0 \\
0 & 0 & 4.30e+2 & 3.93e+2 & -2.64e+1 & 2.68e+0 & 0 & 0 \\
0 & 0 & -4.76e+2 & -4.33e+2 & 2.92e+1 & -2.96e+0 & 0 & 0 \\
0 & 0 & 7.85e-1 & 7.11e-1 & -1.79e+2 & 1.88e+1 & 0 & 0 \\
0 & 0 & 7.75e+0 & 7.01e+0 & -1.77e+3 & 1.76e+2 & 0 & 0 \\
0 & 0 & 0 & 0 & 0 & 0 & 6.73e-1 & 9.77e+1 \\
0 & 0 & 0 & 0 & 0 & 0 & -1.21e+0 & -1.67e+0
\end{pmatrix}$$

$$\|Q\|\,\|Q^{-1}\| = 267.0132$$

As an example for test computations of spectral portraits, let us consider coupled bending-torsion vibrations of blades in the cascades of turbomachinery in a gas flow. The system of differential equations that describes small vibrations of such a cascade has the form [5]

$$m_n \ddot{h}_n + S_n \ddot{a}_n + K_{nh} h_n = L_n + F_n$$
$$S_n \ddot{h}_n + J_n \ddot{a}_n + K_{na} a_n = M_n$$

$$(n = 1, 2, ..., N)$$

where h_n, a_n are the generalized coordinates of blade deformation owing to bending-torsion vibrations, m_n, J_n are the generalized masses and moments of inertia of the blades, K_{nh}, K_{na} are the coefficients of generalized bending and torsion stiffness, S_n are the coefficients of generalized coupling of bending and torsion vibrations, N is the number of blades in the cascade, F_n are the elastic coupling forces of blades with each other, and L_n, M_n are the generalized aerodynamic forces and moments acting on the nth blade. In the theory of cascades in an unsteady flow [6], the latter quantities can be presented as

$$L_n = q\sigma \sum_{r=1}^{N} \left(l'_{r-n,h}\frac{h_r}{b} + l''_{r-n,h}\frac{\dot{h}_r}{\omega b} + l'_{r-n,a}a_r + l''_{r-n,a}\frac{\dot{a}_r}{\omega} \right)$$

$$M_n = q\sigma \sum_{r=1}^{N} \left(m'_{r-n,h}\frac{h_r}{b} + m''_{r-n,h}\frac{\dot{h}_r}{\omega b} + m'_{r-n,a}a_r + m''_{r-n,a}\frac{\dot{a}_r}{\omega} \right)$$

where q is the free-stream dynamic pressure, σ and b are the surface area and chord of the blade, l_{r-n}, m_{r-n} are the aerodynamic coefficients of the blade effect, which are functions of the Strouhal number $k = \omega b/V$, V is the free-stream velocity, $\omega = Im\lambda$, and λ is the root of the corresponding characteristic equation of this system.

We now introduce the notation

$$\omega_{nh}^2 = \frac{K_{nh}}{m_n}, \quad \omega_{na}^2 = \frac{K_{na}}{J_n}, \quad \gamma_n = \frac{S_n}{m_n b}, \quad \rho_n^2 = \frac{J_n}{m_n b}$$

$$\nu = \frac{\omega_{na}^2}{\omega_{nh}^2}, \quad \varepsilon_n = \frac{q\sigma}{m_n b \omega^2}, \quad \bar{h}_n = \frac{h_n}{b}$$

and note that the estimate $\varepsilon_n < 1$ is valid because the unsteady aerodynamic forces acting on the blade are much smaller than the elastic forces and forces of inertia. With this notation, the system takes the form

$$\ddot{\bar{h}}_n + \gamma_n \ddot{a}_n + \omega_{nh}^2 h_n = \varepsilon_n \omega^2 \bar{L}_n + \frac{1}{m_n}F_n$$

$$\gamma_n \ddot{\bar{h}}_n + \rho_n \left(\ddot{a}_n + \nu\omega_{nh}^2 a_n \right) = \varepsilon_n \omega^2 \bar{M}_n \quad (n = 1,\ 2\ ...\ N)$$

where

$$\bar{L}_n = \sum_{r=1}^{N} \left(l'_{r-n,h}\frac{\bar{h}_r}{b} + l''_{r-n,h}\frac{\dot{\bar{h}}_r}{\omega b} + l'_{r-n,a}a_r + l''_{r-n,a}\frac{\dot{a}_r}{\omega} \right)$$

$$\bar{M}_n = \sum_{r=1}^{N} \left(m'_{r-n,h}\frac{\bar{h}_r}{b} + m''_{r-n,h}\frac{\dot{\bar{h}}_r}{\omega b} + m'_{r-n,a}a_r + m''_{r-n,a}\frac{\dot{a}_r}{\omega} \right)$$

Note that the matrix corresponding to the left-hand side of the system is a Hamiltonian, and the matrix corresponding to the right-hand side can be considered as its perturbing component. As the initial parameters required for solving the system, one can use the values of $\omega_{nh}, \gamma_n, \rho_n, \nu, \varepsilon_n, k$, and aerodynamic influence coefficients whose values are summarized in Gorelov et al. [7] as functions of cascade geometry and flow parameters (within the framework of the ideal fluid model).

Figures 2–6 show the 1D spectral portraits of matrices in a system that describes vibrations of a cascade of thin blades at $c = 0$ (cascade density $\tau = 1.5$; ejection angle $\beta = 30$ deg; deflection of the midline of the blade, related to its chord, $f = 0.025$; Strouhal number $k = 0.5$; and number of blades in the period $N = 10$) in a flow of an ideal incom-
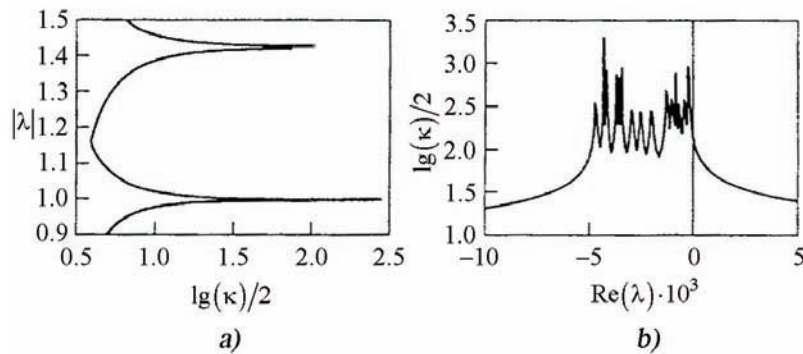
FIG. 2: Dichotomy criterion κ (a) and X_a (b) for the cascade of blades, having the same inertial and elastic parameters: $\gamma = -0.3, \nu = 2, \rho = 1, \varepsilon = 0.01$.
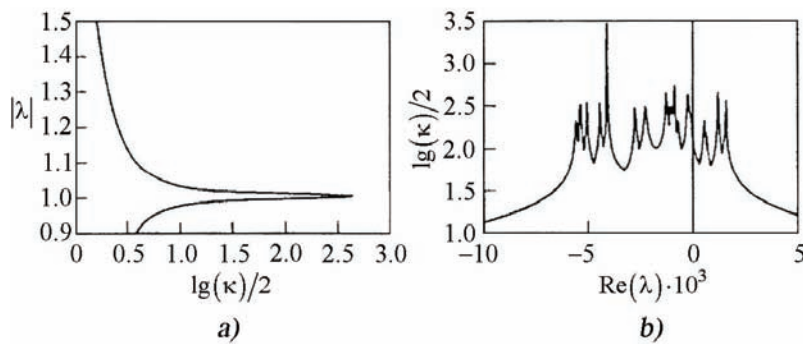
FIG. 3: Dichotomy parameters (a) κ and (b) X_a for the blades cascade with the characteristics $\gamma = 0, \nu = 1, \rho = 1, \varepsilon = 0.01$.

pressible fluid. The symbol κ is the criterion of dichotomy of the spectrum of matrices by concentric circles with the center at the origin of the complex plane of eigenvalues, depending on the circle radius, and the symbol X_a denotes the quality of dichotomy by lines, parallel to the imaginary axis, from the coordinate a of their intersection with the real axis. The values of R and a, for which κ and X_a are almost infinite, determine the absolute values and real parts of eigenvalues; more exactly, those intervals that are considered as reliable on the basis of the computations performed.

Figure 2 shows the dichotomy criteria κ (Fig. 2a) and X_a (Fig. 2b) for the above-mentioned cascade with blades possessing identical inertial and elastic parameters, equal to $\gamma = -0.3, \nu = 2, \rho = 1, \varepsilon = 0.01$.

Note that for these parameters of the cascade, the Hamiltonian component of the matrix has essentially different eigenvalues (Fig. 2a); therefore, the real values of the total matrix that describes cascade vibrations with allowance for aerodynamic interaction (Fig. 2b) can be fairly accurately determined by the perturbation method.

Figure 3 shows the dichotomy parameters κ and X_a for the cascade whose blades have the following characteristics: $\gamma = 0, \nu = 1, \rho = 1, \varepsilon = 0.01$. In this case, the absolute
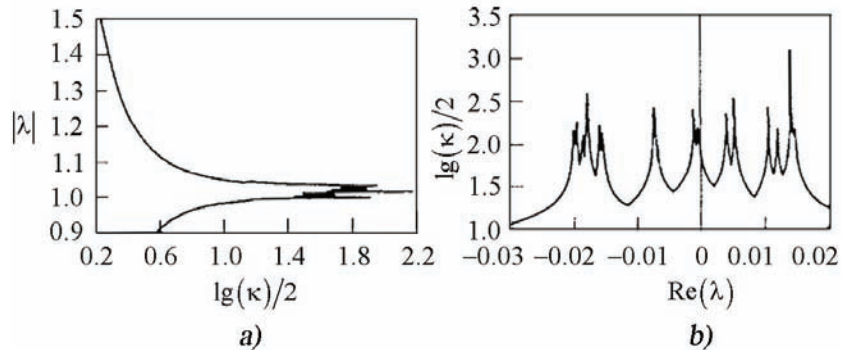
FIG. 4: The dichotomy quality for almost the same cascade as that in Fig. 3, but with additional allowance for elastic coupling of blades with each other.
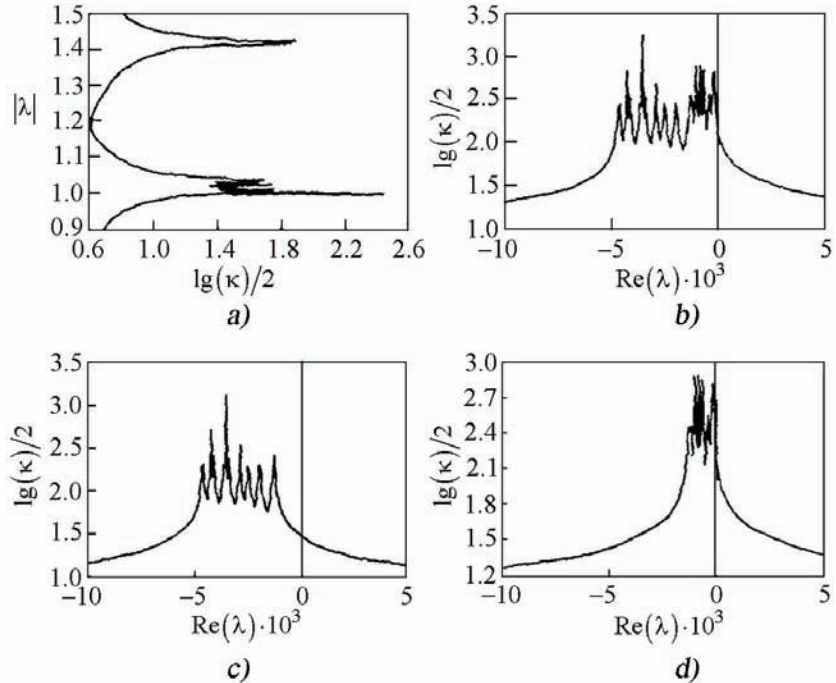
FIG. 5: (a,b) The dichotomy quality of the cascade in Fig. 2 and (c,d) its change while passing from the larger order matrices to the lower-order ones.

values of matrix eigenvalues almost coincide with each other (Fig. 3a); hence, the perturbation method cannot be used to determine the real parts of the eigenvalues. The curve of the dichotomy quality X_a characterizes the positions of these values with guaranteed accuracy (Fig. 3b). For this combination of blade parameters, several eigenvalues of the matrix are located in the right half-plane, i.e., the corresponding matrix is unstable.
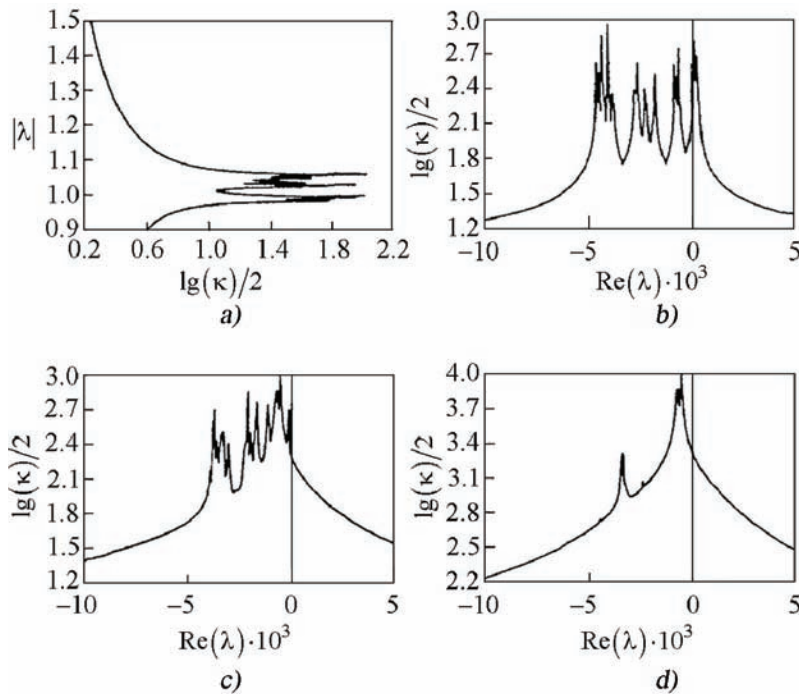
FIG. 6: The influence of a small perturbation of the Hamiltonian component of the matrix by the example of Fig. 3.

Figure 4 shows the dichotomy quality for almost the same cascade as that in Fig. 3, but with additional allowance for elastic coupling of blades with each other. The dichotomy parameter κ for the corresponding matrix with $c = 0.2\omega_n^2$ is plotted in Fig. 4a, which shows that this matrix consists of Jordan cells of dimension 2 and 4. According to available knowledge, such a matrix should be more sensitive to perturbations, which is evidenced by its dichotomy quality X_a (Fig. 4b).

One advantage of the spectral portraits of matrices is the possibility of reducing the analysis of stability of high-order matrices in some cases to the analysis of stability of their submatrices of lower order. The presence of clusters, representing the numerous eigenvalues, located close to each other, is the criterion of existence of this possibility. These clusters are well removed from each other in the complex plane at a good dichotomy quality.

As an example, consider a matrix whose dichotomy parameters are shown in Fig. 2. It follows from the dichotomy quality of this matrix κ, with allowance for elastic coupling F_n (Fig. 5a), that the criterion indicated above is satisfied in the case considered. A comparison of the dichotomy quality X_a for the total matrix (Fig. 5b) with similar dependencies for the corresponding submatrices (Figs. 5c and 5d) supports this statement.

The influence of a small perturbation of the Hamiltonian component of the matrix on the stability of the latter is illustrated in Fig. 6. As an example, consider the matrix

whose spectral portrait is shown in Fig. 3. Its perturbing component describes the action of blade coupling forces of the form $F_n = (-1)^n c(h_{n+1} + h_{n-1} - 2h_n)$.

Figure 6a shows the spectrum dichotomy by radial circles. Figure 6b illustrates the portrait of the same spectrum by dichotomy by straight lines, parallel to the imaginary axis; some part of the spectrum is seen to lie in the right half-plane. After detuning, the entire spectrum is located in the left half-plane, which is illustrated in Fig. 6c. As the detuning parameter increases, the spectrum is shifted to the left (Fig. 6d). This example illustrates the known fact of the influence of small geometric inhomogeneity of cascades on the stability of their vibrations.

The methods of stability analysis described in this paper are implemented with the use of simple iterative algorithms, proposed and described in Bulgakov [1] and Malyshev [8]. The algorithms solve Lyapunov matrix equations and their generalizations to the case of spectrum dichotomy. These generalizations, as we have learned, have appeared in the book [9]. Unfortunately, its content was not understood by us. This slowed the explanation, to which we paid less attention, than to the numerical schemes construction.

ACKNOWLEDGMENT

REFERENCES

1. Bulgakov, A. Ya., Effectively computed quality parameter of stability of a system of linear differential equations with constant coefficients, *Sib. Mat. Zh.*, vol. 21, no. 3. pp. 32–41, 1980.

2. Bulgakov, A. Ya. and Godunov, S. K, Circular dichotomy of a matrix spectrum, *Sib. Mat. Zh.*, vol. 29, no. 5, pp. 59–70, 1988.

3. Godunov, S. K., *Lectures on Advanced Aspects of Linear Algebra*, Nauchnaya Kniga, Novosibirsk, 2002.

4. Bunkov, V. G. and Mosunov, V. A., Application of Lyapunov action integral for estimating stability of a linear system, *Uch. Zap. TsAGI,* vol. 19, no. 2, pp. 110–113, 1988.

5. Bendiksen, O. and Friedmann, P., Coupled bending-torsion flutter in cascade, *AIAA*, vol. 18, no. 2, pp. 194–201, 1980.

6. Gorelov, D. N., Kurzin, V. B., and Saren, V. E., *Aerodynamics of Cascades in an Unsteady Flow*, Nauka, Novosibirsk, 1971.

7. Gorelov, D. N., Kurzin, V. B., and Saren, V. E., *Atlas of Unsteady Aerodynamic Cascades*, Nauka, Novosibirsk, 1974.

8. Malyshev, A. N., Guaranteed accuracy in spectral problems of linear algebra, *Collected Papers Inst. Math. (SB RAS)*, vol. 17, pp. 19–104, 1990.

9. Daletskii, Yu. A. and Krein, M. G., *Stability of Solutions of Differential Equations in the Banach Space*, Nauka, Fizmatgiz, Moscow, 1970.

INVESTIGATION OF THE BPR ENGINE NOZZLE WITH CONTROLLABLE CHEVRONS

A. A. Aleksentsev, D. B. Bekurin, E. V. Vlasov,
A. A. Inozemtsev, G. N. Lavrukhin, A. P. Paduchev &*
O. A. Umpeleva

Central Aerohydrodynamic Institute (TsAGI) 1, Zhukovsky str., Zhukovsky, 140180, Moscow region, Russia

*Address all correspondence to G. N. Lavrukhin E-mail: uzts@tsagi.ru

Results of 3D aerodynamic calculations concerning the influence of the turbojet nozzle chevron deflection angle into the flow on engine thrust characteristics are presented. The optimum deflection angle, at which the chevrons exert the minimum influence on the thrust losses, is chosen. The scheme of the deflection angle control by the ring, made of the shape-memory material nitinol is proposed. The investigation results of the aerogasdynamic and acoustic characteristics of the nozzle with the chevrons are given.

KEY WORDS: *3D analysis, experiment, nozzle, chevron, jet, thrust losses, engine, chevron deflection angle, optimization, noise, shape-memory materials*

1. INTRODUCTION

Nowadays, in order to decrease the noise from the reaction jet of the turbojet engine, the chevrons, being fixed on the nozzle exit (Fig. 1) and having sufficiently high acoustic efficiency at relatively easy structure, are widely spread. The jet noise decrease by the chevrons is known to be based on the intensification of the mixing process of the external flow and the nozzle jet. In addition, as experiments show [1], the transformation of the jet noise spectrum occurs—the noise level decreases at low frequencies and increases at high frequencies. The greater the deflection angle α of the chevrons in the nozzle, the stronger is the jet noise spectrum transformation, so at great chevron deflection angles, the negative effect of the noise increase at high frequencies can exceed the positive effect of the noise decrease at low frequencies, which results in the fact that the total noise level of the nozzle with chevrons is higher than that of one of the nozzles without chevrons. This implies that there is an optimum deflection angle $(\alpha_{\mathrm{opt}})_{\mathrm{ac}}$ at which the noise decrease at a chosen mode is maximum for every chevron configuration.
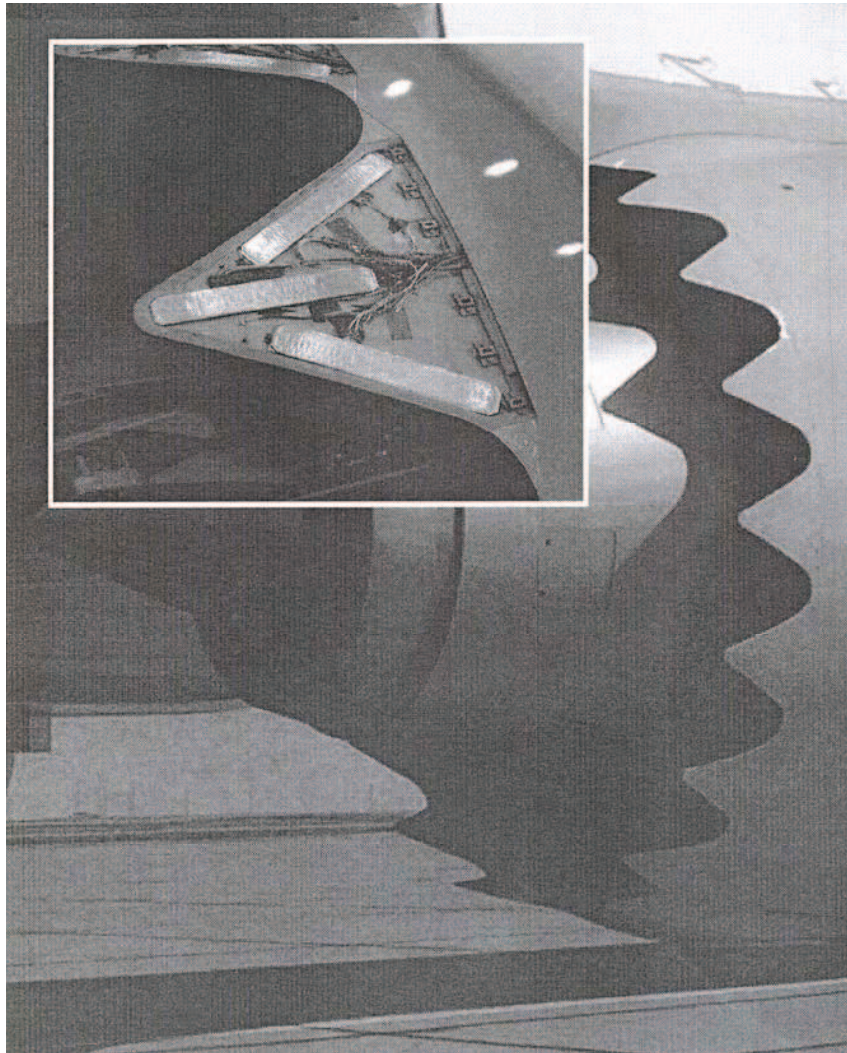
FIG. 1: Chevrons with nitinol drive.

The chevrons' effect on the jet leads to a change in the nozzle thrust characteristics. In addition, depending on the nozzle and chevrons' shape, there is an optimum deflection angle of the chevrons $(\alpha_{\mathrm{opt}})_t$ at which the thrust losses of the nozzle with chevrons at cruise mode are minimum. In the general case, the optimum acoustic and thrust angles are not equal, i.e., $(\alpha_{\mathrm{opt}})_{\mathrm{ac}} \neq (\alpha_{\mathrm{opt}})_t$, because even a small deflection of the chevrons' setting angle from $(\alpha_{\mathrm{opt}})_t$ during flight can lead to an essential loss of engine efficiency. Therefore, the investigations concerning the development of the schemes of the chevron deflection angle control during the flight are carried out in engine companies. This will allow setting $(\alpha_{\mathrm{opt}})_{\mathrm{ac}}$ and $(\alpha_{\mathrm{opt}})_t$ during the flight for the maximum decrease of noise.

Nowadays, the scheme, using shape-memory material, for example, titanium nickelide TiNi (nitinol) is the simplest and the most perspective for chevron control. The companies Boeing, General Electric, Goodrich Aerospace, and NASA within the framework of the program Quit Technologies Demonstrator 2 (QTD2) could decrease the noise level at takeoff by 3–4 dB and improve the fuel rate under the conditions of cruise flight by 1% by using shape-memory chevrons at the nozzle of the aircraft Boeing 777-300ER (see Fig. 1) [2–4].

Consequently, while designing the chevron control scheme, it is necessary to know both angles $(\alpha_{\mathrm{opt}})_{\mathrm{ac}}$ and $(\alpha_{\mathrm{opt}})_{t}$. The value of $(\alpha_{\mathrm{opt}})_{\mathrm{ac}}$ for the concrete engine with chevrons can be defined by the results of full-scale or model acoustic tests. As for the angle $(\alpha_{\mathrm{opt}})_{t}$, it can be defined both experimentally and by means of 3D calculations of the nozzle overflow [5].

Given in the present paper are the results of the calculations of flow over the triangle chevrons, fixed on the engine nozzle with mixing (with the annular mixer), with various chevron deflection angles α, by means of which the angle $(\alpha_{\mathrm{opt}})_{t}$ is specified. The authors propose and investigate the scheme of chevrons control by means of the ring, made of the nitinol, which changes its diameter ("remembers" its shape) as the temperature varies, and correspondingly changes the chevron deflection angles.

The scheme of the nozzle with triangular chevrons was considered. The chevron bases were situated close to each other on the nozzle exit.

The computational area was chosen from the condition of the periodical arrangement of the chevrons. Its beginning was displaced upstream, as is shown in Fig. 2, and the end was situated at a distance of ~ 7 diameters from the nozzle exit, the radius was ~ 8 nozzle
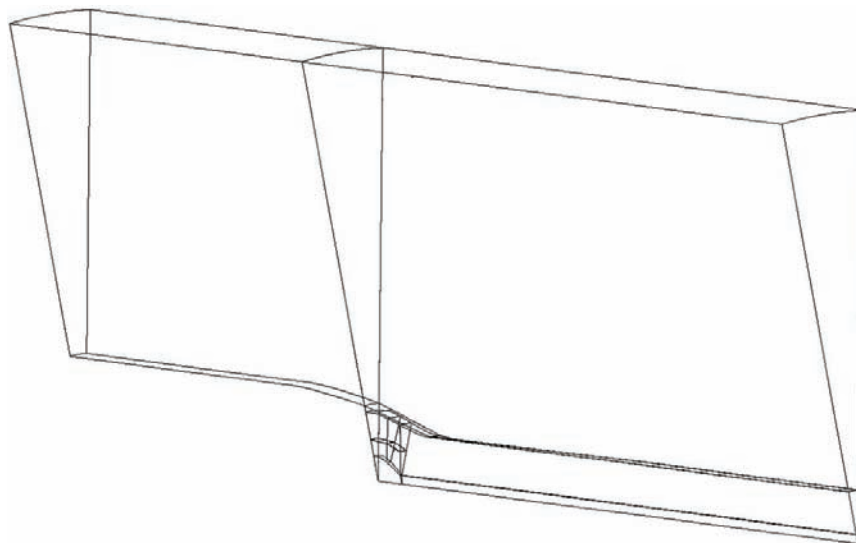

FIG. 2: Computational area.

exit radii. The computational grid contained $\sim$1 million nodes. All the calculations were fulfilled for the mode close to the cruise flight of an aircraft.

The ideal gas, which is close to the air in its characteristics, i.e., the gas constant is $R_g = 287.13$ J/kg K and the adiabatic coefficient is $k = 1.4003$, was taken to be the operating medium. In order to analyze various variants of the nozzles, we used the engine thrust losses $\Delta \bar{P}$ (%)

$$\Delta \bar{P} = \left(1 - \frac{P}{P_{\mathrm{id}}} \right) 100$$

where P is the real (measured or calculated) engine thrust (the thrust component directed along the engine axis), $P_{\mathrm{id}} = (P_{\mathrm{id.n}} - G_a V_\infty \cos \delta)$ is the ideal engine thrust specified by the real gas flow through the nozzle G_n (here, $P_{\mathrm{id.n}} = G_n V_{\mathrm{id}}$ is the ideal nozzle thrust, i.e., the thrust of an ideal nozzle where the gas extends up to atmospheric pressure p_∞ perfectly, without losses) at the same parameters at the nozzle entry $(p^*, T^*, \text{ and } G_n)$ as in the investigated real nozzle; $V_{\mathrm{id}} = a_{\mathrm{cr}} \lambda_{\mathrm{id}} = \sqrt{2k R_g T^* / (k+1)} \, \lambda_{\mathrm{id}}$ is the ideal velocity of the gas flow from the nozzle, $k = 1.4003$ is the specific heat ratio; $R_g = 287.13$ is the gas constant; λ_{id} is the ideal reduced velocity of the flow, which can be defined from the equation

$$\pi \left(\lambda_{\mathrm{id}} \right) = \left(1 - \frac{k-1}{k+1} \lambda_{\mathrm{id}}^2 \right)^{k/(k-1)} = \frac{p_\infty}{p^*};$$

where G_a is the airflow at the engine entry, V_∞ is the flight velocity, and δ is the angle between the free-stream direction $\vec{V}_\infty$ and the engine axis. The calculation results are presented in Fig. 3.

Among all the investigated variants of the nozzles with chevrons, the nozzle with the deflection angle $\alpha = 0$ (Fig. 4) has the minimum thrust losses, which are only 0.06% greater than that ones of the initial nozzle without chevrons. Therefore, the optimum thrust angle for the given nozzle $(\alpha_{\mathrm{opt}})_t = 0$.

Taking into account the fact that from the viewpoint of noise suppression, the optimum chevron deflection angles are 6–12 deg [5], it follows that the calculated engine thrust losses, while fixing the chevrons at the angle $\alpha \cong 6$ deg, are $\sim$10% greater than the thrust losses in the case of the nozzle without chevrons (see Fig. 3).

In order to reduce the thrust losses during the flight, the authors propose the following scheme of the chevron deflection angles' control by means of the ring, made of the shape-memory material nitinol. The use of this ring to provide the rigidity and connectivity of the entire chevron structure was already proposed in a patent [7] in 1995 (Fig. 5). The ring is fixed to every chevron. The operating principle of the proposed scheme consists of the following. The chevrons are fixed on the nozzle in such a way that in the free state without the ring, their deflection angle is close to zero ($\alpha \cong 0$). The initial length of the nitinol ring is chosen in such a way that while putting it on the chevrons during take-off, from the viewpoint of the noise suppression, the deflection angle becomes equal to the optimum angle. At the cruise mode, the ring temperature decreases to approximately
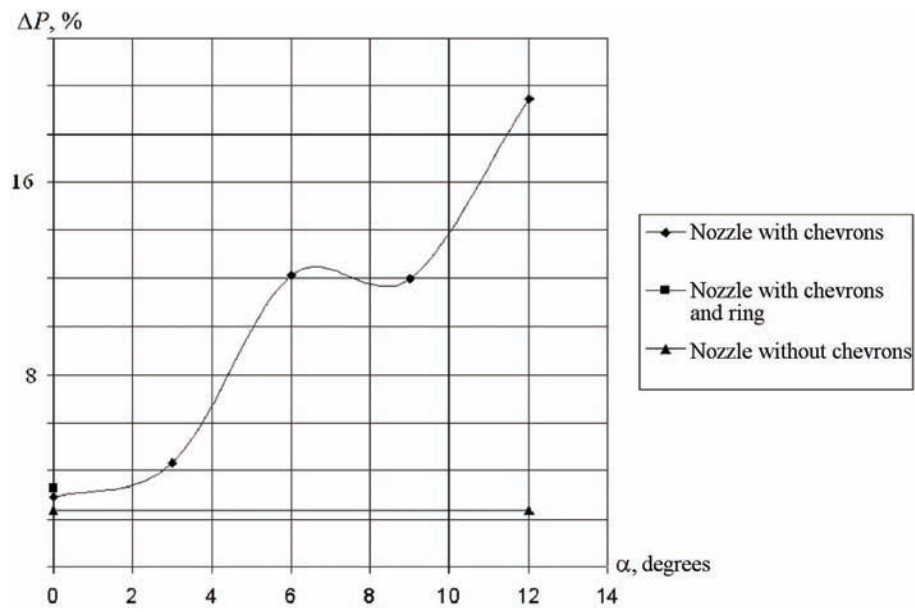
FIG. 3: Engine thrust losses efficient versus the chevron deflection angle.
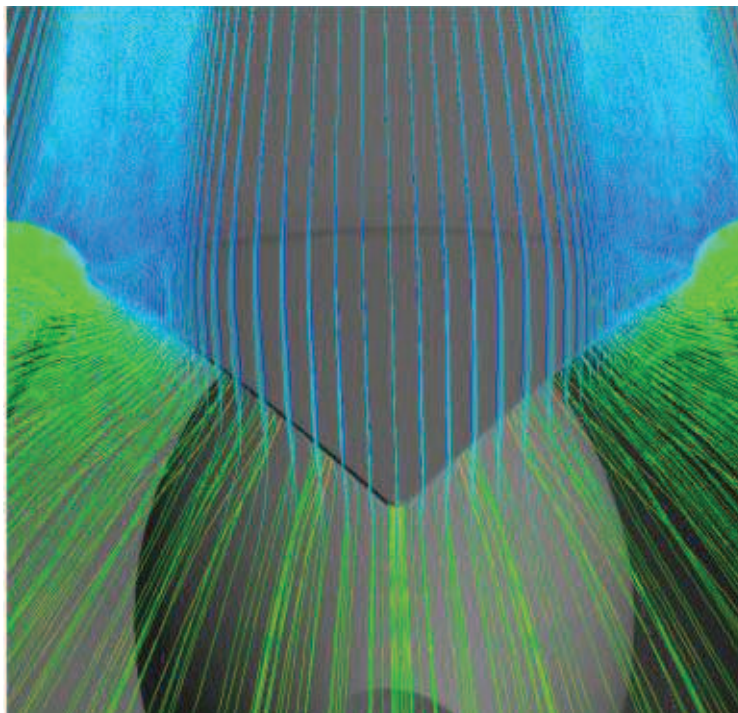
FIG. 4: The nozzle with chevrons, $\alpha = 0$.
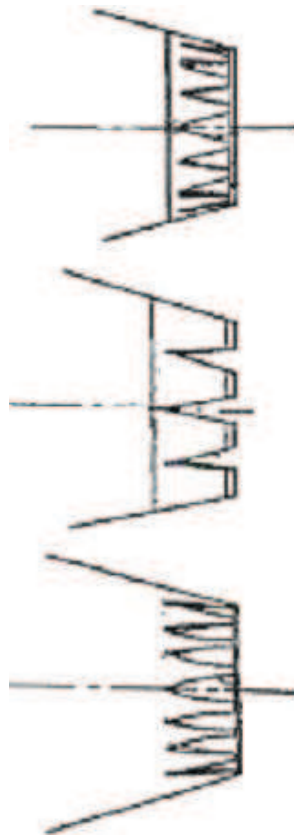
FIG. 5: The use of the ring for the rigidity and connectivity of the chevrons' structure from the patent 2289921 [6].

$0°C$, in this case the nitinol elasticity coefficient is decreased 2–3 times because of the transition from the austenitic to martensite state [6]. Consequently, the ring allows the chevrons to straighten up to $\alpha \cong 0$ owing to their own elasticity. This provides the minimum thrust losses at cruise mode. At landing mode, the ring is heated, and the reverse transition from the martensite to austenitic state to increase the nitinol elasticity coefficient occurs in it. As a result, the ring "remembers" its shape, namely, its initial length becomes shorter and deflects the chevrons inside the jet up to the optimum deflection angle.

According to the calculations fulfilled in this work, the thrust losses in the variant with the ring increased only by 0.15% in comparison to the variant of the nozzle without chevrons, and by 0.09% in comparison to the nozzle without ring, i.e., the ring leads to an increase of the thrust losses by $\sim$0.1%.

The additional thrust losses associated with the ring fixing essentially depend on its shape. For example, the thrust losses in the variant with the ring with the rectangular

cross section (Fig. 6b) at the optimum deflection angle are greater than in the variant of the ring of the aerodynamic shape (Fig. 6a) with $\alpha = 0$ by 2.11%.

In order to estimate the loads necessary for the optimum deflection angle of the chevrons, special calculations were completed. The chevron represented the bent sheet (Fig. 7). The forward part of the chevron was rigidly fixed, and in the area of the chevron contact with the ring, the load, equidistributed over the plane, was set. The shift of the chevron tip S and the equivalent deflection angle α_e were defined depending on the
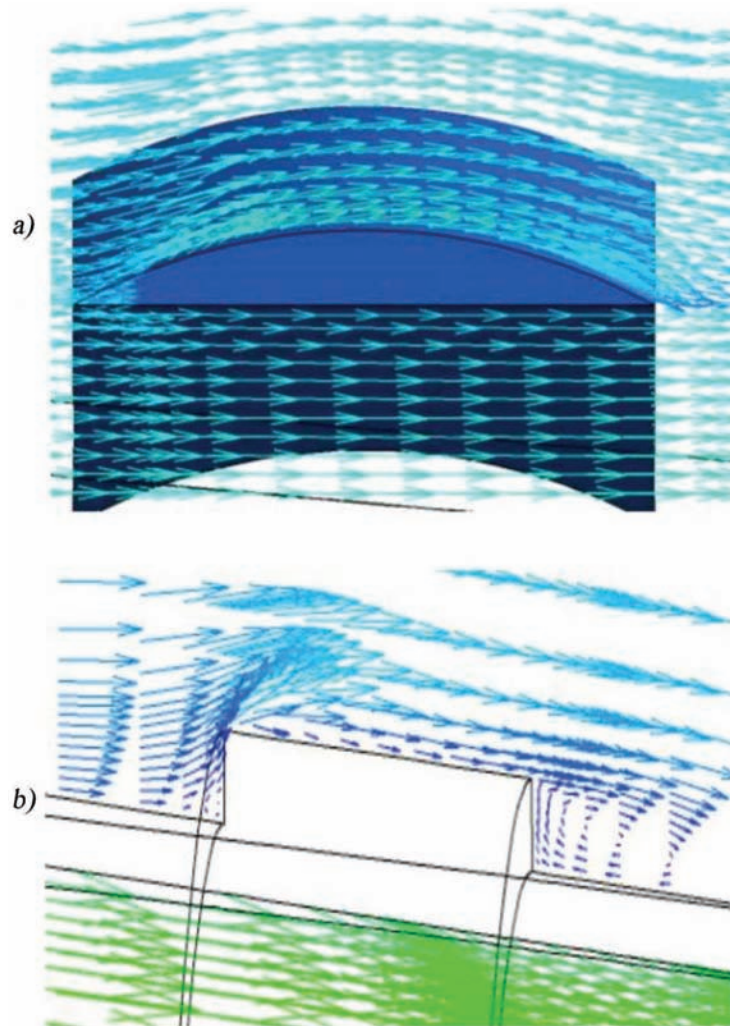
FIG. 6: Flow pattern: (a) the flow over the ring with the cross section of the streamlined shape (ring width 15 mm, maximum thickness 1.5 mm, external surface is made in form of the circle arc); (b) the flow over the ring with the rectangular cross section (10×2 mm).
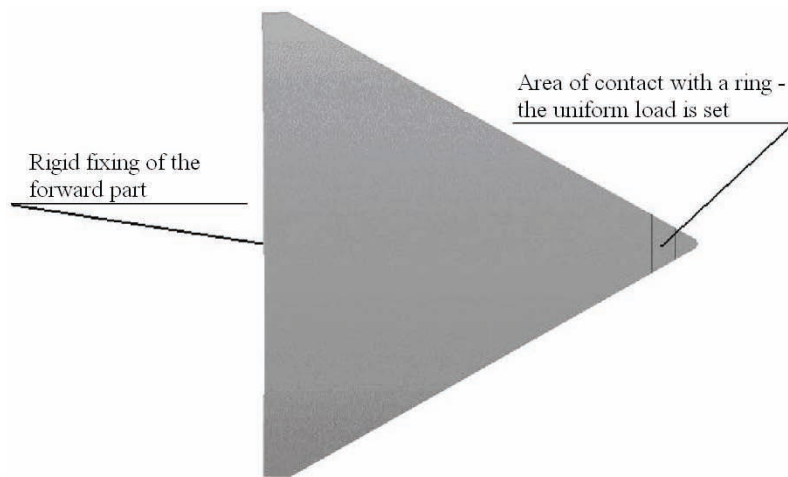
FIG. 7: The chevron computational scheme.

applied load (Fig. 8). Shown in Fig. 9 is the pattern of the chevron deformations and tensions obtained by the calculation.

In order to provide the deflection of the considered chevron at the optimum angle, it is necessary to apply some force. The decrease of this force can be achieved by diminishing the chevron thickness. For this purpose and also for the definition of the nitinol
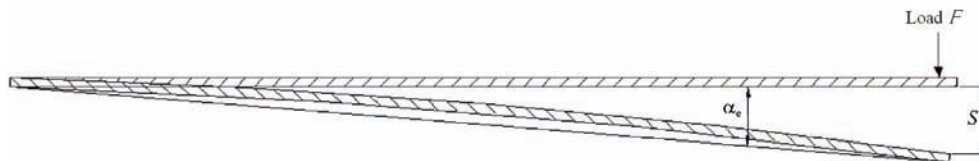
FIG. 8: Specification of the chevron tip shift S and of the equivalent deflection angle α_e under the action of the load F.
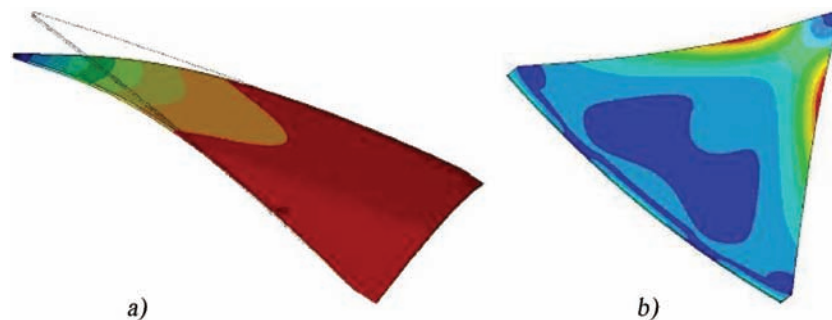
FIG. 9: Strength calculation of the chevron: (a) the chevron deformation (m); (b) stress spectrum in the chevron.

ring geometric parameters, providing the required force, it is necessary to complete calculations of the chevrons of various thickness with the nitinol ring.

In order to provide the optimum chevron deflection angle, the shift S should be on the order $Ltg\left(\alpha_e\right)$, i.e., the nitinol ring should elongate by the value $2\pi\left[(R+S)-R\right] = 2\pi S$, which equals ~4% of the initial ring length for the case considered in this paper. Ordinary metals cannot bear such deformations. The nitinol can reproduce its shape, even at deformations on the order of 10% owing to its superplasticity [6]. However, it is necessary to carry out special cyclic tests to check the performance of the drive during the given period of time.

Finally, it is worth noting the advantages and the shortcomings of this chevron control scheme in comparison with the initial variant, in which the chevron "control" was realized by means of nitinol plates. In the initial variant, the nitinol drive was made in the form of the plates, placed inside the chevron (see Fig. 1). The main advantage of the initial variant in comparison with the proposed scheme with the ring is the absence of the additional drag due to the drive.

The disagreement of the chevron deflection angles during the exploitation (because every drive is made and is working individually) and the absence of the possibility to adjust the scheme can be referred to as the shortcomings of the initial variant. In the scheme with the ring, all the chevrons and the drive are working in agreement with each other. This fact excludes the possibility of the angles' disagreement during the exploitation. In addition, the ring gives an additional rigidity to all the structure.

Both schemes can be considered to be approximately of the same mass. In the proposed scheme, the ring mass can be greater than the total mass of the nitinol plates in the initial variant, but owing to more rigid structure, one can make the chevrons thinner in the scheme with the ring. The complex of the experimental investigations concerning the analysis of the deflected chevrons' influence on the noise decrease, on the value of the angle of the jet axis deflection, and on the value of the nozzle effective thrust losses was carried out along with the numerical investigation.

It is worth noting that the complex solution of the problems, mentioned above, resulted in the necessity to choose the optimum chevrons' geometry, their amount and arrangement on the nozzle exit, the optimum deflection angle of the chevrons into the reaction jet, and so on. In addition, the complex experimental investigations of the nozzles with chevrons involved the specification of the aerogasdynamic and acoustic characteristics on the special facilities in TSAGI.

The illustration of the experimental results is presented in Fig. 10. The following results in Fig. 10 are the most important:

- The location of the chevrons along the nozzle exit contour allows for a decrease in the noise level by approximately 1–1.5 dB, whereas the deflections of the chevrons into the jet essentially increases its mixing with the ambient air and decreases the noise by ~7 dB.
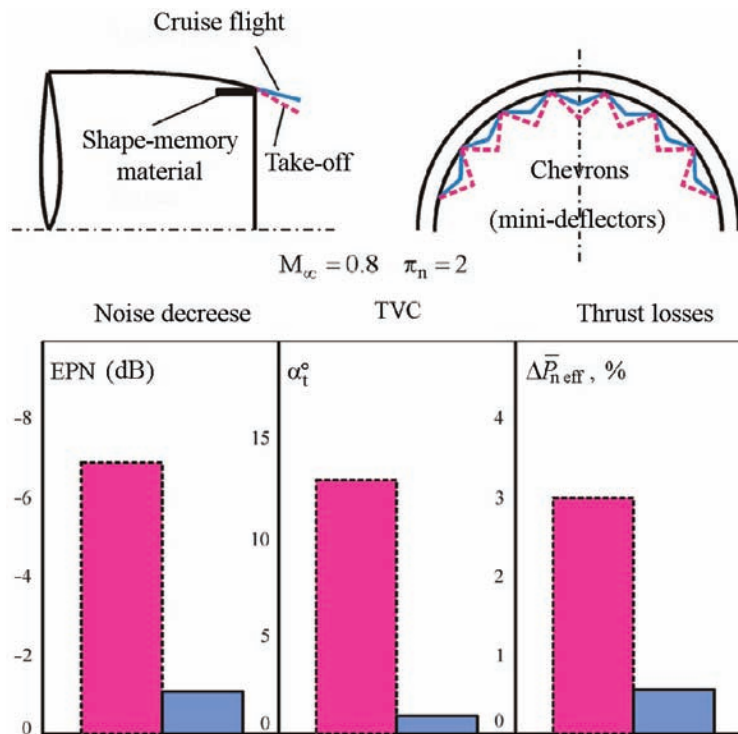
FIG. 10: Generalization of the results of the investigation of the nozzle with chevrons.

- In addition, the corresponding arrangement of the deflected chevrons allows the deflection of the engine jet axis (TVC) approximately at 12 deg, which allows an increase the stability and controllability of the aircraft during takeoff and landing.

- The price of the chevron deflection to solve the problems, mentioned above, is equivalent to an increase in the nozzle effective thrust losses by $\sim$3% of the ideal thrust (approximately 9–10% of the engine thrust losses) from the viewpoint of the aerogasdynamic efficiency, which is unacceptable in the presence of the uncontrollable chevrons.

- The use of the chevron location control by means of the memory-shaped materials allows obtaining the maximum effect from the chevrons' deflection during the takeoff/landing mode and to minimize the thrust losses at the cruise flight mode of the aircraft.

REFERENCES

1. CIAM, The experimental investigation of the acoustic efficiency of the chevron two-circuit nozzles of the BPR-2005C engines, Scientific Tech. Report of CIAM, No. 700-4413, Mos-

cow, 2004.

2. Craig, L., Boeing noise technology, Los Angeles World Airports Community Noise Roundtable, Sept. 13, Boeing, 2006.

3. Eury, S., Research and technology at Snecma to ensure sustained development of air transportation, AIAA/AAAF Aircraft Noise and Emissions Reduction Symposium, May 24–26, Monterey, CA, Snecma, 2005.

4. Gliebe, P. and Dodds, W., Practical technolog solutions for future aircraft engine noise and emissions reduction, AIAA/AAAF Aircraft Noise and Emissions Reduction Symposium, May 24–26, Monterey, CA, GE Transportation Aircraft Engines, 2005.

5. Brailko, I. A. and Krasheninnikov, S. U., The investigation of the aerodynamic characteristics of the chevron nozzles based on the numerical calculation of the flow, *Izv. RAN., MZhG.*, no. 2, pp. 76–88, 2005.

6. Stoeckel, D., The shape memory effect—Phenomenon, alloys and applications, *Proceedings: Shape Memory Alloys for Power Systems,* EPRI, 1995.

7. Herris, A. E., Nozzle for turbofan aeroengines, Patent Great Britain No. 2289921, January, 1995.

ASSYMETRY AND NONUNIQUENESS OF THE SOLUTION OF THE PROBLEM OF SEPARATED FLOW OVER A SLENDER CONICAL WING–BODY COMBINATION

A. V. Voevodin

Central Aerohydrodynamic Institute (TsAGI) 1, Zhukovsky str., Zhukovsky, 140180, Moscow region, Russia; E-mail: lyapunov@tsagi.ru

Performed are the numerical investigations of the separated flow over a slender circular cone-delta wing combination within a wide range of key parameters, with the combination being situated symmetrically relative to the free stream. Two approaches are used to solve the problem. Within the framework of the slender body theory, nonunique symmetrical and asymmetrical solutions are obtained. The area of existence of various solutions is specified. The 3D-RANS CFD calculations of the small aspect ratio combination with the forebody in the form of a circular cone and with the delta wing, taking into account the viscosity, are carried out. It is shown that in this case, the problem has unique solutions, which are symmetrical at small angles of attack and asymmetrical at greater ones. At relative angles of attack, being less than 2, the lift coefficients, obtained by two approaches, are very close. This fact estimates the application area of the slender body theory. The flow patterns in the section of the combination conical part, illustrating the flow peculiarities, are given.

KEY WORDS: *asymmetry, non-uniqueness, separated flow, cone-delta wing, low aspect ratio, calculations with account of viscosity*

1. INTRODUCTION

Many works are aimed at the investigation of inviscid stationary separated flow over a slender wing-body conical combination. Provided that the angle of attack and the apex angle of the delta wing are small, the initial 3D stationary problem is usually reduced to the 2D nonstationary problem and then one finds its self-similar solution. The various models of the vortex sheet getting off the trailing edge have been proposed and improved in Refs. [1–4]. In the most complete among these models, the sheet exterior was simulated by the finite number of intervals with distributed vorticity, and the vortex spiral interior was represented by the discrete vortex. The evolution equation of the sheet was used to specify its shape and intensity [5]. The use of the conformal transformation of

the body contour in the cross section on the interval, situated along the free stream, or on the circle, was a significant aspect of most of the works. This fact allowed to meet automatically the no-leakage boundary condition. It should be noted that also in Ref. [6], where the aerodynamic singularities, whose intensity was specified by the no-leakage condition, were distributed on the body contour. Such an approach allows to investigate the conical layouts, where the contour of the cross section cannot be conformally transformed to an interval or to a circle in a simple way. One used the iteration method or relaxation method to solve the obtained equations [7–9].

A lot of calculations were completed by the mentioned technique. For example, the calculations of the combination of the delta wing with the conical fuselage, having a half-circle in the cross section [10], and also the calculations of the wing, having the arc of a circle in the cross section [11]. Cited in Ref. [12] are the calculation results of the flow over the yawed delta wing.

The nonuniqueness of the problem solution within a certain range of the angle of attack and of the ratio of the fuselage diameter to the wing span was discovered while investigating the symmetrical flow over the circular cone–delta wing combination [13]. Shown in Ref. [14] is the fact that if the solution symmetry is not required previously (i.e., to solve the problem for the complete body, rather than for its half), then at the symmetrical position of the combination relative to the free stream, the problem has both symmetrical and asymmetrical solutions, including the unstable ones. However, the stability investigation was carried out for the simplest model of vortex sheet ("vortex cut") because in this case, such investigation can be fulfilled analytically.

The first part of the present work is aimed at the investigation within the framework of the slender-body theory of the existence of the area of the stable symmetrical and asymmetrical solutions of the problem concerning the separated flow over the circular cone–delta wing combination, situated symmetrically relative to the free stream. Carried out in the second part are the calculations of the finite length combination with the forebody in the form of the cone and the delta wing by means of the 3D-RANS method.

2. PROBLEM STATEMENT

The separated flow over the slender circular cone–delta wing combination is investigated. We will consider the fluid to be inviscid and incompressible, the shear layers to be represented by the velocity tangential discontinuity, and the separation lines to be attached to the wing sharp edge. The half-angle at the wing apex δ and the angle of attack α are small: $\delta \sim \alpha = o(1)$. The X-axis of the reference frame $OXYZ$ is directed along the combination axis, the Y-axis is directed upward, and the Z-axis is in the wing plane. According to the conventional procedure, the original 3D problem (in variables X, Y, Z) is reduced to the 2D nonstationary problem concerning the separated flow over the uniformly widening body, which represents the combination cross section (in variables $t = X/U_\infty, Y, Z$, where U_∞ is the free-stream velocity). The self-similar variables x

and y are introduced further so that $Y = yU_\infty ttg\delta$ and $Z = xU_\infty ttg\delta$, and the complex variable $z = x + iy$.

In the z plane, the free-stream velocity (relative angle of attack) $\alpha_0 = \sin\alpha/tg\delta \cong \alpha/\delta$, the wing edges are at the points –1 and 1, and the fuselage radius is denoted by $m < 1$ (Fig. 1).

Then, acco ... et, result-ing from the di ... nal to the sheet, and from

$$(1)$$

where $w(z)$ is ... nd $\Delta\varphi =$ Γ is the discon ... et. At the point (–1, 0), $\angle$ ... $_2$ are the total circulation ...

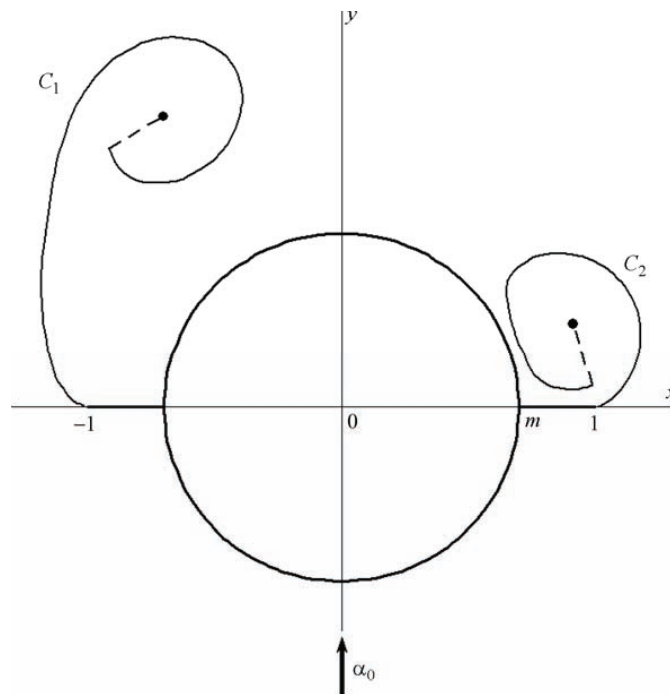In order to ... the body contour to the e ... variable $\mu = \zeta + i\eta$. Su ...

FIG. 1: The body contour and the vortex sheet in the z plane.

$$z = \frac{1+m^2}{4}\left(\mu + \frac{1}{\mu}\right) + \sqrt{\left[\frac{1+m^2}{4}\left(\mu + \frac{1}{\mu}\right)\right]^2 - m^2}$$

Taking into account that at infinity $d\mu/dz = 2/(1+m^2)$, and using the reflection method, we write the complex potential as follows:

$$w(\mu) = m^2 \ln z - i\alpha_0 \frac{m^2+1}{2}\left(\mu - \frac{1}{\mu}\right) + \frac{1}{2\pi i}\int\limits_{C_1} \ln \frac{\mu - \mu(\Delta\varphi)}{\mu - \left[1/\overline{\mu(\Delta\varphi)}\right]} d\Delta\varphi$$

$$+ \frac{1}{2\pi i}\int\limits_{C_2} \ln \frac{\mu - \mu(\Delta\varphi)}{\mu - \left[1/\overline{\mu(\Delta\varphi)}\right]} \, d\Delta\varphi \tag{2}$$

Thus, the constructed potential satisfies the no-leakage condition on the body and behaves at infinity as $-i\alpha_0 z$.

While taking into account Eq. (2) and introducing the new variable $\lambda = 1-(\Delta\varphi/G)$, Eq. (1) is reduced to the form

$$(1-\lambda)^2 \frac{d}{d\lambda}\left(\frac{\bar{z}}{1-\lambda}\right) = \frac{m^2}{z} - i\alpha_0 \frac{m^2+1}{2}\left(1 + \frac{1}{\mu^2}\right)\frac{d\mu}{dz} + \frac{1}{2\pi i}\left[G_1 \int\limits_0^1 \left(\frac{1}{\mu - \mu_1(\lambda)}\right.\right.$$

$$\left.\left. - \frac{1}{\mu - \left[1/\overline{\mu_1(\lambda)}\right]}\right)d\lambda + G_2 \int\limits_0^1 \left(\frac{1}{\mu - \mu_2(\lambda)} - \frac{1}{\mu - \left[1/\overline{\mu_2(\lambda)}\right]}\right)d\lambda\right]\frac{d\mu}{dz} \tag{3}$$

Subscripts 1 and 2 in the integration elements denote that the integration is over the contour of the left or right sheets.

The Chaplygin-Zhukovsky condition at the sharp wing edges, where the derivative $d\mu/dz$ becomes infinite, gives two additional real equations for the intensities G_1 and G_2, which are to be determined, provided that the sheet geometry is known,

$$2\pi\alpha_0(m^2+1) + G_1 \int\limits_0^1 \frac{\left[1 - \varsigma_1^2(\lambda) - \eta_1^2(\lambda)\right]}{\left[1 - \varsigma_1(\lambda)\right]^2 + \eta_1^2(\lambda)}d\lambda + G_2 \int\limits_0^1 \frac{\left[1 - \varsigma_2^2(\lambda) - \eta_2^2(\lambda)\right]}{\left[1 - \varsigma_2(\lambda)\right]^2 + \eta_2^2(\lambda)}d\lambda = 0 \tag{4}$$

$$2\pi\alpha_0(m^2+1) + G_1 \int\limits_0^1 \frac{\left[1 - \varsigma_1^2(\lambda) - \eta_1^2(\lambda)\right]}{\left[1 + \varsigma_1(\lambda)\right]^2 + \eta_1^2(\lambda)}d\lambda + G_2 \int\limits_0^1 \frac{\left[1 - \varsigma_2^2(\lambda) - \eta_2^2(\lambda)\right]}{\left[1 + \varsigma_2(\lambda)\right]^2 + \eta_2^2(\lambda)}d\lambda = 0 \tag{5}$$

3. NUMERICAL SOLUTION METHOD

For the numerical solution of the problem, every sheet was represented by the exterior part, being divided into the finite number of intervals N_1 and N_2, and the interior part,

being replaced by the discrete vortex (the core). The end of the last interval of the exterior part was connected to the discrete vortex by the cut to avoid the nonuniqueness of the velocity potential (shown in Fig. 1 by the dashed line). Accordingly, the integration in Eqs. (3)–(5) was fulfilled between the limits 0 and λ_{N_1} and between the limits 0 and λ_{N_2}, respectively, and the integrals over the interior parts of the sheets were replaced by the corresponding effect of the discrete vortices. The integrals over the sheet intervals, being adjacent directly to the edges $(\lambda \ll 1)$, were calculated using the asymptotes near the sharp edge of the slender wing, according to which in the problem considered is

$$\mu_1(\lambda) = -1 - a_1\lambda^{1/2} + ib_1\lambda + \cdots$$
$$\mu_2(\lambda) = 1 + a_2\lambda^{1/2} + ib_2\lambda + \cdots$$

The real constants a_1, a_2, b_1, and b_2 were specified numerically.

In order to specify the coordinates of the cores, the well-known condition of the absence of the total force, effecting the vortex-section system, was used. This condition is written as follows:

$$2\overline{z_C} - \overline{z_N} = \left.\frac{dw}{dz}\right|_C \tag{6}$$

where z_C are the coordinates of cores 1 or 2, and z_N are the coordinates of the end of the corresponding sheet exterior part. The complex conjugate velocity was calculated in the corresponding point z_C.

Equations (3)–(6) were solved by the iteration method. In this case, Eq. (3) was applied at the middle points of the sheet intervals, and the integration was fulfilled by the trapezoidal method, being of the second approximation order. The model of the sheet, the exterior part of which consisted only of the asymptotical area, adjoining to the edge, was used as the initial approximation. The solution for this model converged rapidly; and furthermore, the number of intervals of the exterior part and its length were successively increased up to the formation of approximately one spiral turn. After that, forces acting on the combination were calculated. A more detailed finite-difference interpretation of the equations and of the calculation algorithm is given in Ref [13].

4. CALCULATION RESULTS

As was mentioned above, the solution is nonunique at the symmetrical problem statement within the framework of the slender-body theory. Within a certain range of the angles of attack and of the relative fuselage radii, there are two stable solutions and one unstable solution to the symmetrical disturbance. Shown while investigating the solutions at a nonsymmetrical statement [14], is the fact that one of the symmetrical solutions is unstable to nonsymmetrical disturbances. In addition, a set of stable and unstable nonsymmetrical solutions exists. Since these investigations were fulfilled within the framework of the simplified model of the vortex sheet (vortex cut), there is still a

question about how the situation changes while using more a detailed model to answer. Carried out in the present work are the calculations of the flow within a wide range of the problem parameters for the complete sheet model (sheet–vortex cut) at a nonsymmetrical statement.

Let us consider the results of these investigations. Shown in Figs. 2 and 3 are the lift and lateral force coefficients versus the relative angle of attack α_0 for the various values of the fuselage radius m $(K = tg\delta)$. The symbol s corresponds to the symmetrical solution, and the symbol us corresponds to the nonsymmetrical one. The stable symmetrical solution exists for all the values m and $\alpha_0 < \alpha_{01}(m)$. If α_0 exceeds $\alpha_{01}(m)$, the symmetrical solution will lose stability. In this case, at $m < m^* \approx 0.8$, the solution becomes unstable to nonsymmetrical disturbances, but in the absence of these disturbances, the solution can be extended to greater angles of attack. If $m > m^*$ and $\alpha_0 > \alpha_{01}(m)$, the symmetrical solution is unstable both to nonsymmetrical and to symmetrical disturbances.

Based on the performed calculations, one can plot the diagram showing the existence areas of the problem stable solutions (Fig. 4). The curve $\alpha_{01}(m)$ in this diagram repeats qualitatively a similar dependence, cited in Ref. [14]. However, this dependence, as was expected, proved to be shifted down by the angles of attack. This difference is caused by the fact that the simplified vortex sheet model was used in Ref. [14]. In addition, the curve $\alpha_{02}(m)$, corresponding to the rise of the asymmetry, and the curves separating the existence areas of various asymmetrical solutions, are plotted in Fig. 4.

One can distinguish five areas with a various number of stable solutions in Fig. 4 (furthermore, we will consider two asymmetrical solutions, being the mirror reflection

FIG. 2: Lift coefficient versus the relative angle of attack.

$$\frac{c_z}{K^2}$$

- m = 0.3
- m = 0.4
- m = 0.5
- m = 0.7
- m = 0.75
- m = 0.9

α_0
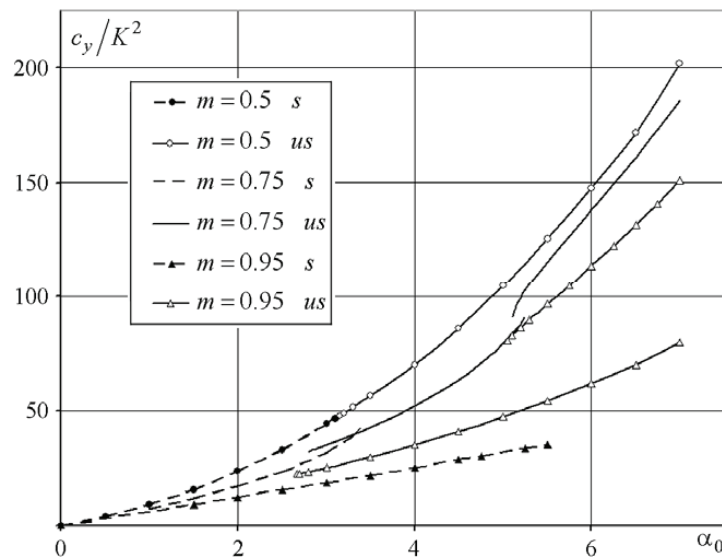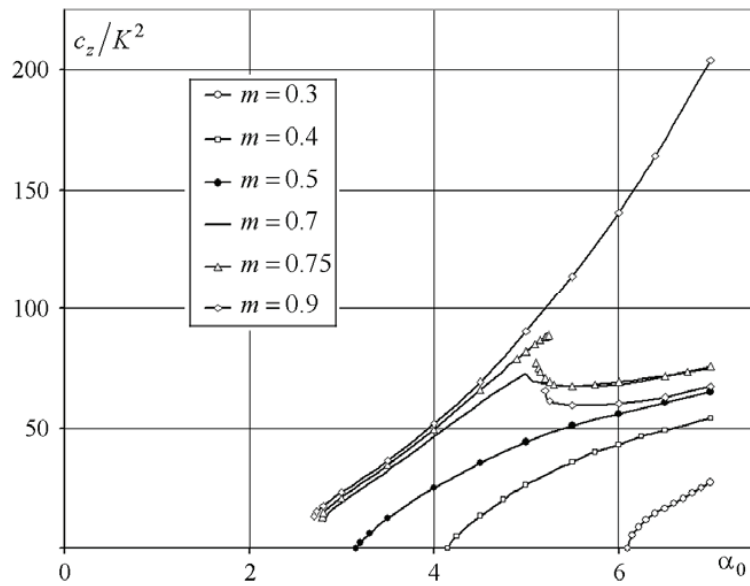
FIG. 3: Lateral force coefficient versus the relative angle of attack.

α_0

(4)

(5)

(2)

$\alpha_{01}(m)$

(3)

(1)

$\alpha_{02}(m)$

m
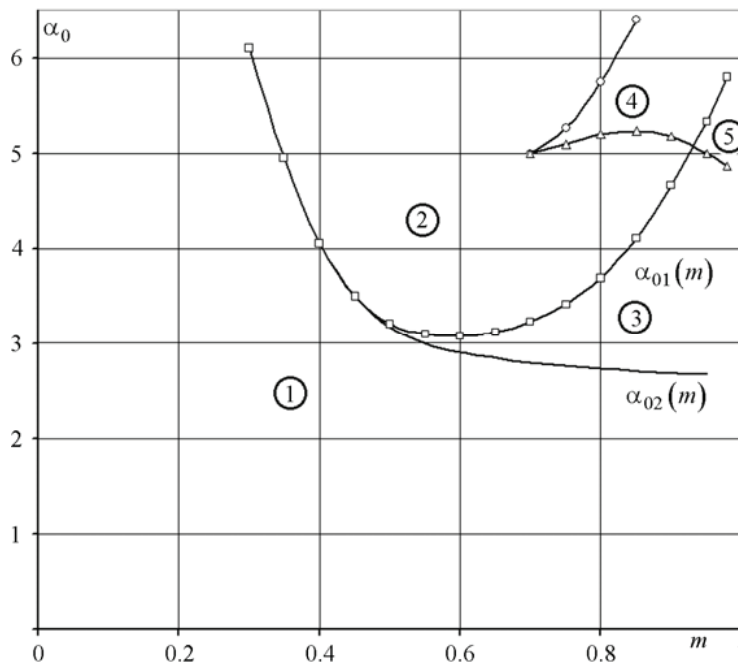
FIG. 4: Existence areas of the problem stable solutions: □, rise of the nonsymmetrical solution; —, loss of stability of the symmetrical solution; ○, nonsymmetrical solution 1; △, nonsymmetrical solution 2.

$$\frac{c_z}{K^2}$$

- m = 0.3
- m = 0.4
- m = 0.5
- m = 0.7
- m = 0.75
- m = 0.9

of each other relative to the y-axis, to be one solution), i.e., 1 represents one symmetrical solution, 2 represents one asymmetrical solution, 3 represents two solutions (one symmetrical and one asymmetrical solution), 4 represents two asymmetrical solutions, and 5 represents three solutions (one symmetrical and two asymmetrical solutions).

Shown in Fig. 5 is the shape of the vortex sheets for several values of the parameters α_0 and m, corresponding to the areas 3, 4, and 5. The configurations of the sheets, corresponding to the various solutions, are seen to be sufficiently different.

5. FLOW CALCULATION WITH ACCOUNT OF THE VISCOSITY

The problem nonunique solutions, mentioned above, take place at sufficiently great relative angles of attack. In this case, the assumption of the slender-body theory $\alpha \sim \delta = o(1)$ begins to be violated. In addition, the viscosity and the influence of the finite body length can play a sufficient role in the realization of one or another solution. Thus, to overcome the limitations of the slender-body theory and to take into account the viscosity the CFD calculations of the steady flow over two combinations, having the forebody in the form of a circular cone with the slender delta wing of zero thickness were carried out.

Both combinations have the same fuselage, namely, the conical part length is 1 m, the cylindrical part length is 0.5 m, and the tail part represents a half-sphere. The wing of the first combination (Fig. 6) has the apex half-angle $\delta = 5$ deg, with the ratio of the
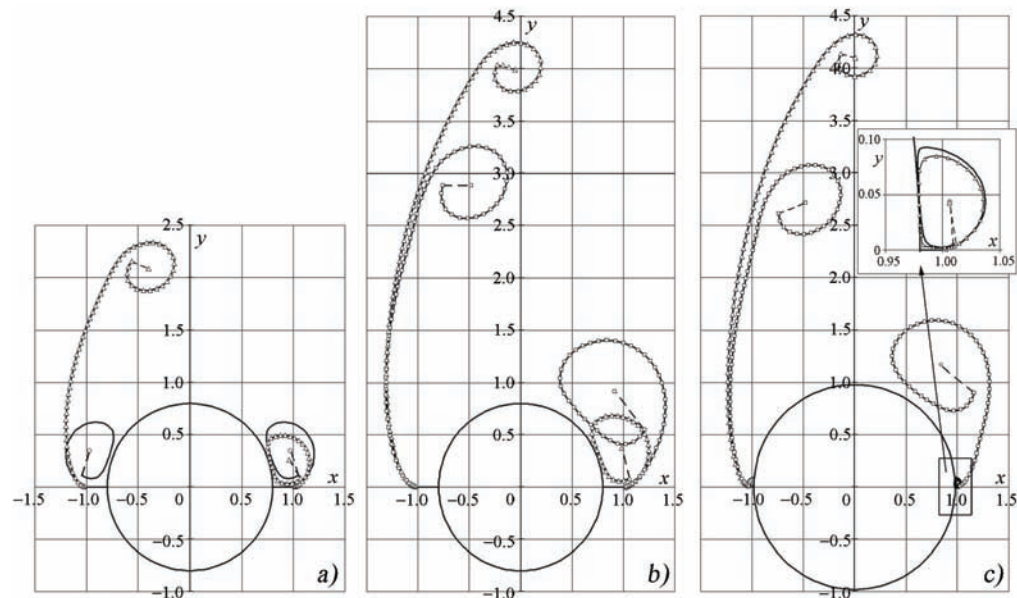
FIG. 5: Vortex sheet configuration: (a) $m = 0.8$, $\alpha_0 = 3.5$; (b) $m = 0.8$, $\alpha_0 = 5.4$; (c) $m = 0.98$, $\alpha_0 = 5.2$ —— — symmetrical solution, Δ — solution 1, $\square$ — solution 2.

FIG. 6: Geometry of the wing-fuselage combination.

fuselage diameter to the wing span being $m = 0.9$. The apex half-angle of the second wing is $\delta = 6$ deg, which corresponds to the parameter $m = 0.75$. Since the essential qualitative difference in the calculation results for these two variants has not been found out, further on, mainly the data for $m = 0.9$ are given. The calculation area had the following dimensions: from -1.5 to 5 m along the X-axis, from -1.3 to 1.3 m along the Y-axis, and from -1.5 to 1.5 m along the Z-axis, and contained about one million cells. The fuselage nose was situated at the origin.

The Reynolds-averaged Navier-Stokes equations with the SST turbulence model were solved. The free stream had the velocity 50 m/s, the density 1.2 kg/m^3, and the viscosity 1.83×10^{-5} kg/m s. The calculations were performed for the angles of attack up to 45 deg, which corresponded to $\alpha_0 = 8.082$.

Shown in Figs. 7 and 8 are the lift and lateral force coefficients in the section $X = 0.7$ m versus the relative angle of attack at $m = 0.9$. For convenience of the comparison with
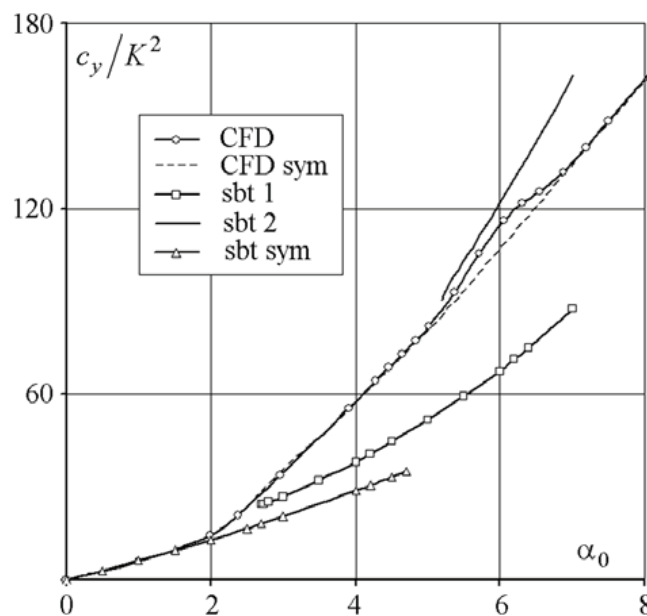
FIG. 7: Lift coefficient versus the relative angle of attack (m = 0.9).
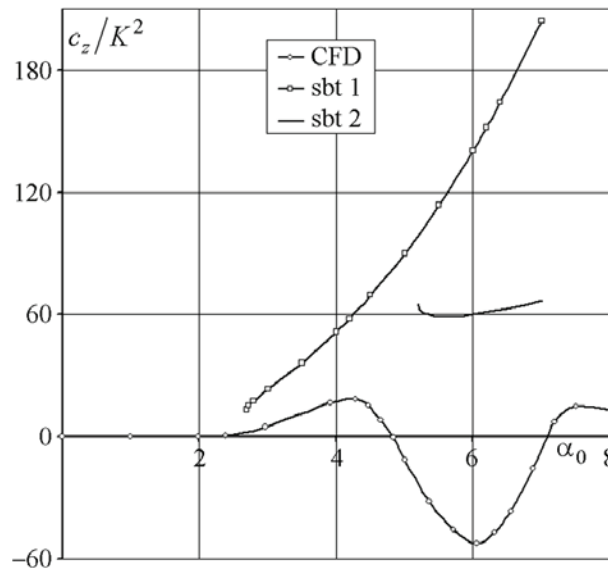
FIG. 8: Lateral force coefficient versus the relative angle of attack (m = 0.9).

the slender-body theory (sbt) results, their values are divided by K^2. Plotted in Fig. 7 by the dashed line is the curve corresponding to the calculation of the half-combination (symmetrical problem statement). The lift coefficients in the two considered cases are seen to be very close. The difference is observed only within the range $\alpha = 26$–37 deg, which corresponds to the maximum in absolute magnitude lateral force in the asymmetrical solution.

The unique solution is realized within the entire investigated range of the angle of attack. In this case, up to the angle of attack 12 deg ($\alpha_0 = 2.38$), it is symmetrical and the lift coefficients, obtained by the slender-body theory and by the CFD method, are almost the same. At greater angles of attack, the solution loses symmetry, and the lateral force appears. Its behavior corresponds to the experimental data [15, 16]. Any intermittent vortex structures, which are observed at the flow over the slender rotational bodies, have not been found out. Shown in Fig. 9 are the streamlines, getting off the wing edges on the conical part of the combination at $\alpha = 30$ deg, $m = 0.9$. The flow is seen to be asymmetrical and close to the conical one in this area, even at such a great angle of attack. It is known that in the conical flows, the streamlines near the vortex core are almost cylindrical. One can see in Fig. 9 a small deflection of these streamlines from the cylindrical surface (spreading), which can be caused by a great angle of attack, by the integration method of the streamlines, and by their great length.

Presented in Fig. 10 are the patterns of the vorticity fields for the layout with $m = 0.75$ in the cross section $X = 0.7$ m for the angles of attack 10 and 15 deg. The vortex sheets, calculated by the slender-body theory, are indicated by the dots. At small angles
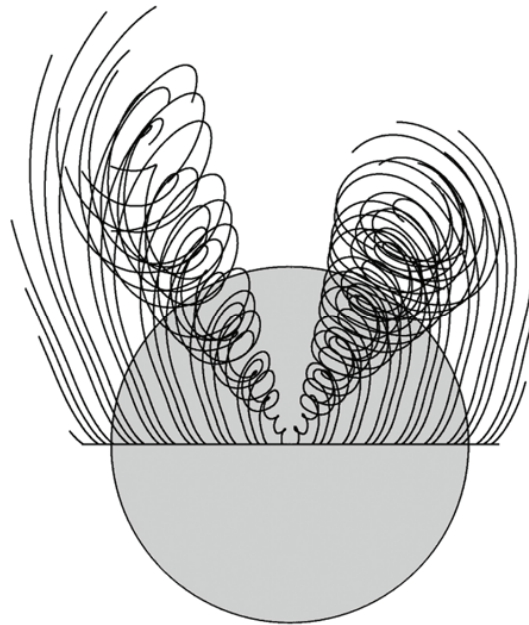
FIG. 9: Streamlines getting off the delta wing edges ($\alpha = 30$ deg, m = 0.9).

$\alpha= 10^\circ$

$\alpha= 15^\circ$
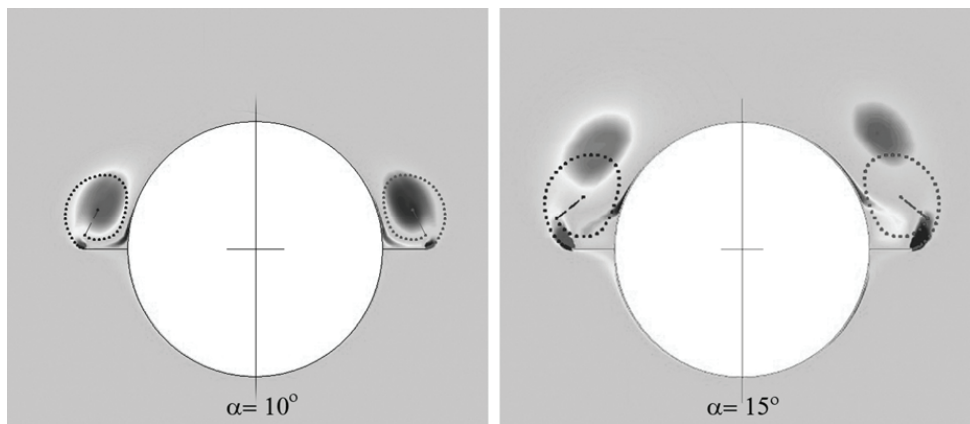
FIG. 10: Vorticity fields in the plane $X = 0.7$ m (m = 0.75).

of attack, both methods give very close flow structures as well as the integral character-istics. At $\alpha = 15$ deg in the CFD calculation, the main vorticity area is shifted upstream, and the asymmetry and the secondary separation from the cone surface become visible. At even greater angle of attack, the differences of the flow patterns increase.

For the investigation of the flow patterns in the section $X =$ constant, we form the following modified velocity field:

$\alpha= 10$

$\alpha= 20$

where U, V,
tion. Shown
$m = 0.9$, X
second sepa
motion in th
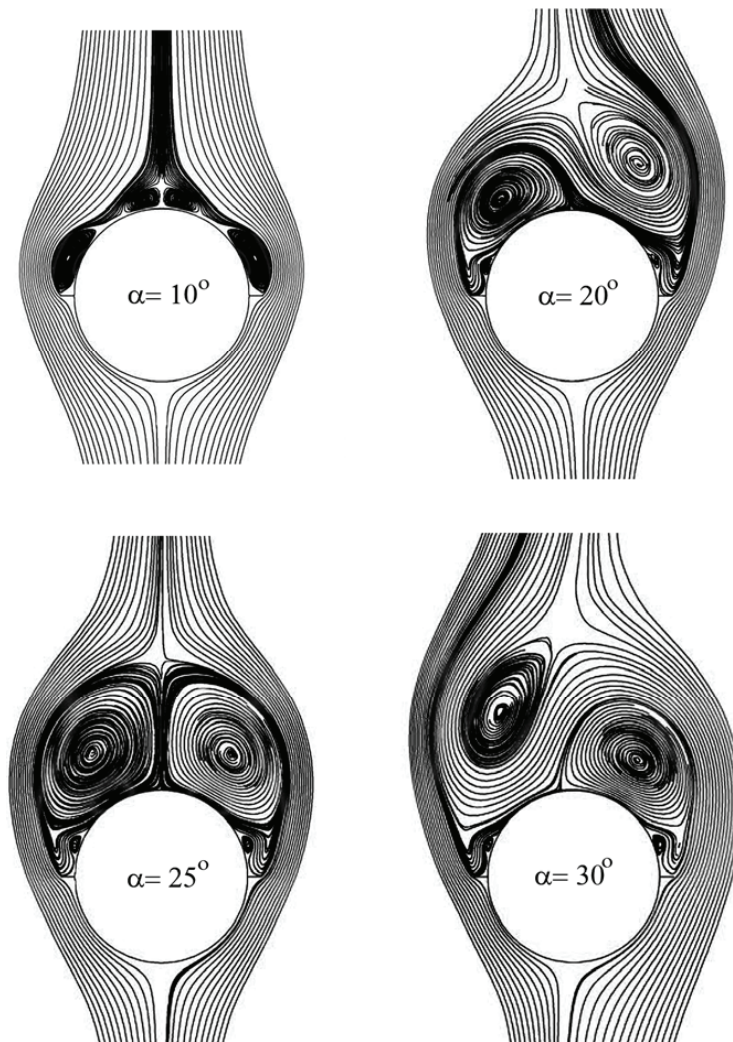
FIG. 11: Flow fields in the plane $X = 0.7$ m (m = 0.9).

As the angle of attack increases, the flow becomes asymmetrical, the second separation disappears, and the secondary separation from the fuselage, which is situated closer to the wing, arises. The curve $c_y(\alpha)$ in the vicinity of $\alpha = 12$ deg essentially changes the slope. At $\alpha \approx 25$ deg, the flow becomes more symmetrical and the lateral force disappears. Further on, the lateral force reverses sign, and at $\alpha \approx 32$ deg, achieves the minimum. Another transition of the lateral force through zero takes place at $\alpha \approx 38.5$ deg.

The steady symmetrical and asymmetrical solutions of the problem of the separated flow over the circular cone–delta wing combination at the symmetrical position relative to the free stream are obtained within the wide range of the key parameters. Shown is the fact that the use of the vortex sheet full model instead of the simplified "vortex-cut" model specifies both the flow characteristics and the existence areas of the various solutions.

The calculations of the finite length combination by the 3D RANS method are fulfilled. It is shown that the solution has an essentially different character at great angles of attack while taking into account the viscosity. The solution is unique, in addition, at small angles of attack, it is symmetrical, the lift coefficient is the same as that one obtained by the slender-body theory, and this theory application area is limited by the relative angles of attack about 2. As α increases, the solution transforms to the asymmetrical one and it differs from the results obtained by the slender-body theory. In addition, the qualitative coincidence of the lateral force behavior by the angle of attack with the experimental data is observed.

REFERENCES

1. Legendre, R., Ecoulement au voisinage de la point avant d'une aile á forte flèche aux incidences moynnes, *Rech. Aéron.*, no. 30, 1952.
2. Brown, C. E. and Michael, W. H., Effect of leading-edge separation on the lift of a delta wing, *JAS*, vol. 21, no. 2, 1954.
3. Zhigulev, V. N., Some problems of the wing non-linear theory, *Trudy TsAGI*, no. 688, 1955.
4. Smith, J. H. B., Improved calculation of leading-edge separation from slender delta wings, Royal Aircraft Establishment, Tech. Rep. No. 66070, 1966.
5. Nikolsky, A. A., About "second" type of the ideal fluid flow over the streamlined body (The investigation of the separated vortex flows), *Rep. USSR Acad. Sci.*, vol. 116, no. 2, pp. 193–196, 1957.
6. Voevodin, A. V. and Sudakov, G. G., Projective method of calculation of the characteristics of the separated flow over the bodies by the ideal fluid, *Uchenye zapiski TsAGI*, vol. XVII, no. 5, pp. 8–17, 1986.
7. Sacks, A. H., Lundberg, R. E., and Hanson, C. W., A theoretical investigation of the aerodynamics of slender wing-body combination exhibiting leading-edge separation, NASA, CR-719, 1967.
8. Molchanov, V. F., On the realization of the strip method in the wing nonlinear theory,

Uchenye zapiski TsAGI, vol. 5, no. 2, pp. 1–9, 1974.

9. Sudakov, G. G., Calculation of the separated flow over a slender thin delta wing, *Uchenye zapiski TsAGI*, vol. 5, no. 2, pp. 10–19, 1974.

10. Voevodin, A. V., Separated flow over a conical combination of a slender wing with non-symmetrical fuselage, *Uchenye zapiski TsAGI*, vol. XIV, no. 4, pp. 1–8, 1983.

11. Voevodin, A. V., On the influence of the slender wing shape in plan and of its surface curvature on the characteristics of its separated overflow, Trudy TsAGI, edit. 2317, pp. 22–32, 1986.

12. Pullin, D. I., Calculations of steady conical flow past a yawed slender delta wing with leading-edge separation, ARC R & M, no. 3767, pp. 1–47, 1975.

13. Voevodin, A. V., Investigation of the solution non-uniqueness of the problem about the separated flow over a slender wing-fuselage system, *Uchenye zapiski TsAGI*, vol. X, no. 1, pp. 10–18, 1979.

14. Goman, M. G., Zakharov, S. B., Khrabrov, A. N., Symmetrical and nonsymmetrical separated flow over a slender wing with a fuselage, *Uchenye zapiski TsAGI*, vol. XVI, no. 6, pp. 1–8, 1985.

15. Andrew B. and Wardlaw Jr., A. B., Multivortex model of asymmetrical shedding on slender bodies at high angle of attack, AIAA Paper No. 75–123, 1975.

16. Zakharov, S. B. and Zubtsov, A. V., Experimental investigation of the separated flow over a slender delta wing, *Uchenye zapiski TsAGI*, vol. XIX, no. 1, pp. 8–12, 1988.

SUPERSONIC FLOW OVER SHARP ELLIPTICAL CONES

V. A. Bashkin, I. V. Egorov*, D. V. Ivanov, & V. V. Pafnutiev

Central Aerohydrodynamic Institute (TsAGI) 1, Zhukovsky str., Zhukovsky, 140180, Moscow region, Russia

*Address all correspondence to I. V. Egorov E-mail: ivan_egorov@tsagi.ru

Completed in the present work are the calculations of supersonic viscous perfect gas flow over a set of sharp elliptical cones by means of a numerical simulation method [1,2] applied to the experiment conditions [3]. Carried out is the comparison of calculated and experimental local and integral characteristics of cones. The calculated and experimental data prove to be in a good agreement. Discussed is the influence of the angle of attack and of the cross-sectional shape on the behavior of local aerodynamic characteristics of the cone.

KEY WORDS: *elliptic cone, elliptic coefficient, angle of attack, numerical simulation, verification of the method*

1. INTRODUCTION

Worked out in Refs. [1, 2] is the approach to the numerical simulation of 3D supersonic flows over sharp bodies based on the nonstationary 3D equations of viscous gas dynamics. Given in Ref. [1] is the method of numerical simulation using Navier-Stokes equations, and carried out is its verification by means of comparison of the results of calculations of flow over a sharp circular cone (Mach number $M_\infty = 10.4$, cone half-angle $\theta_c = 15$ deg, angles of attack $0 \leq \alpha/\theta_c \leq 1.2$) with the experimental data [4]. Described in Ref. [2] is the procedure of numerical simulation using Reynolds equations on the assumption of Bussinesq about Reynolds stresses with the use of a two-parameter differential $(q - \omega)$ turbulence model [5], and fulfilled is the comparison of numerical and experimental data ($M_\infty = 4, \theta_c = 4$ deg, $0 \leq \alpha/\theta_c \leq 2$) by the integral characteristics of a sharp circular cone. In both papers, calculations are carried out on the assumption of flow symmetry, and a good agreement of computational and experimental data, both in a qualitative and in a quantitative sense, is obtained. This circumstance enables the use of the mentioned approach to investigate the supersonic viscous gas flow over sharp conic bodies. Particularly, supersonic ($M_\infty = 4$ and 5) flows over a sharp circular cone

$(\theta_c = 4 \ \mathrm{deg})$ with thermally insulated $[(\partial T/\partial n)_w = 0]$ and isothermal $(T_{w0} = 0.5)$ surfaces are examined in detail in Refs. [6, 7] within some range of angle of attack and of Reynolds number Re.

As was mentioned above, verification of the numerical simulation method is given in Refs. [1, 2] for supersonic flow over sharp circular cones having cross-sectional contours of a constant curvature. Naturally, this brings up the question about how this method works when the curvature of the body cross-sectional contour is variable. To answer this question is the goal of this work, in which the verification of the numerical method is fulfilled with the example of supersonic flow over a set of sharp elliptical cones with thermally insulated surface applied to the experiment conditions [1].

2. EXPERIMENTAL CONDITIONS

Cited in Ref. [1] are the results of experimental investigation of aerodynamic characteristics of a set of sharp elliptical cones at $\mathrm{Re} = V_\infty L / \nu_\infty = 8 \times 10^6$ and $\mathrm{M}_\infty = 1.97$ and 2.94 within the range of the angles of attack $0 \leq \alpha \leq 16$ deg. Here, V_∞ is the free-stream velocity, ν_∞ is the kinematic viscosity coefficient in the free stream, and L is the typical linear size (the model length). The Reynolds number is so great that the laminar-turbulent flow regime is realized in the experiment.

The body cross section represents an ellipse with ellipticity $\delta = b/a$, where a, b are major and minor semiaxes of the ellipse. The investigated set of elliptical cones $(1/6 \leq \delta \leq 1)$ has a fixed base area $L/d_* = 3.67$, where $d_* = 2\sqrt{ab} = 2a\sqrt{\delta}$ is the equivalent base diameter. In other words, one considers the set of cones to be of equal volume. So, the cone half-angles in the planes of major and minor semiaxes turn out to be variable values and are specified by the relations $\mathrm{tg}\theta_c = a/L = 0.13624/\sqrt{\delta}$ and $\mathrm{tg}\theta_{c2} = b/L = 0.13624\sqrt{\delta}$, accordingly, i.e., as the ellipticity decreases, the cone half-angle in the plane of the major semiaxis increases, and the one in the plane of the minor semiaxis decreases. Particularly, for the cones with $\delta = 1, 2/3, 1/3, 1/6$, we have $\theta_c = 7.7$, 9.5, 13.3, 18.5 deg and $\theta_{c2} = 7.7$, 6.4, 4.5, 3.2 deg, accordingly.

3. CALCULATION CONDITIONS

Based on the numerical integration of Reynolds equations according to the procedure [2] on the assumption of Bussinesq about Reynolds stresses use of a two-parameter differential $(q - \omega)$ turbulence model [5], we simulated the supersonic flow over a set of sharp elliptical cones of length L at an angle of attack α, with the flow velocity vector being located in the plane of the minor semiaxis (Fig. 1). In this case, the length L is taken as a typical linear size. The outflow boundary of the computational area falls on the base sharp edge so that the flow in the near wake behind the cone is not calculated. Such an approach to the problem corresponds to the consideration of flow over a half-infinite cone.
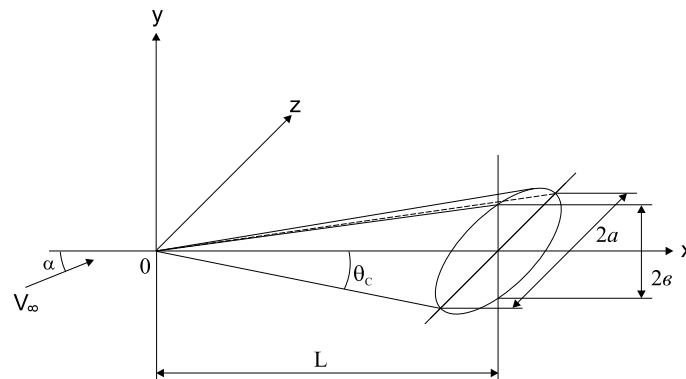
FIG. 1: Scheme of a sharp elliptical cone.

At the numerical simulation, the moving medium is considered to be a perfect gas with specific heat ratio $\gamma = 1.4$, Prandtl number $Pr = 0.7$, and dynamic viscosity coefficient depending only on temperature $[\mu/\mu_\infty = (T/T_\infty)^\omega, \; \omega = 0.7]$. Supposing the flow to be symmetrical with respect to the vertical plane, we calculate one half of the flow field on the nonuniform grid $41 \times 101 \times 81$ (in longitudinal, normal, and circular directions, accordingly). In this case, the surface of the cone is supposed to be thermally insulated.

We fulfilled two series of calculations for the considered set of elliptical cones with thermally insulated surface applied to the experiment conditions [3] at $Re = 8 \times 10^6$ in setting the following values of the free stream turbulence parameters: $q_\infty = q_\infty^*/V_\infty = 0.003$, and $\omega_\infty = \omega_\infty^* L/V_\infty = 1$. In the first series of calculations, we studied the supersonic flow ($M_\infty = 1.97$ and 2.94) over the elliptical cones at zero angle of attack; and in the second series, we considered the supersonic flow over the elliptical cones at an angle of attack of $0 \le \alpha \le 16 \;\; \deg$ and at Mach number $M_\infty = 2.94$.

4. AERODYNAMIC CHARACTERISTICS

The numerical analysis of the Reynolds equation resulted in the definition of the fields of gas dynamic variables near the considered cone, by which we calculated its aerodynamic characteristics, namely, pressure coefficient $c_p = (p - p_\infty)/q_\infty$, and friction drag coefficients in both the radial $c_{fr} = \tau_{rw}/q_\infty$ and circular $c_{f\theta} = \tau_{\theta w}/q_\infty$ directions. Here, $q_\infty = 0.5\rho_\infty V_\infty^2$ is the free-stream dynamic pressure.

Calculated by the known distributions of the local characteristics over the cone surface were its integral aerodynamic characteristics. First of all, we specified the axial T and the normal N components of the aerodynamic force vector

$$T = T_p + T_F, \quad N = N_p + N_F$$

Here, T_p, N_p and T_F, N_F are the projections of normal and tangential stresses applied to the cone streamlined surface, to the cone axis, and to its normal in the flow symmetry plane. We also calculated the moment M_z of aerodynamic forces about the z-axis, being orthogonal to the symmetry plane and passing through the cone apex. By these forces, we calculated the aerodynamic coefficients of axial c_x and normal c_y forces and of the moment m_z as

$$c_x = \frac{T}{q_\infty S_m} = c_{xp} + c_{xF}, \quad c_y = \frac{N}{q_\infty S_m} = c_{yp} + c_{yF}, \quad m_z = \frac{M_z}{q_\infty S_m L}$$

Here, $S_m = \pi ab$ is the cone base area (the midsection area). By means of the pointed-out aerodynamic coefficients, we calculated the lift coefficients c_{y_a}, the drag coefficients c_{x_a}, and the cone lift-drag ratio K by the relations

$$c_{y_a} = c_y \cos\alpha - c_x \sin\alpha, \quad c_{x_a} = c_x \cos\alpha + c_y \sin\alpha, \quad K = \frac{c_{y_a}}{c_{x_a}}$$

5. ZERO ANGLE OF ATTACK

According to the calculation results, the elliptical cone is streamlined without flow separation at zero angle of attack. In this case, the flow field near the circular cone ($\delta = 1$) is axisymmetric, and the flow field near the elliptical cones ($\delta < 1$) is essentially spatial, the flow divergence line situated on the body surface in the major semiaxis plane, and flow convergence line situated in the minor semiaxis plane. In other words, in the first case, the gas motion occurs in the longitudinal direction; and in the second case, the cross flow, being directed from the flow divergence line to the flow convergence line, takes place along with the longitudinal flow.

The local aerodynamic characteristics of cones at $M_\infty = 1.97$ and 2.94 qualitatively are the same, so let us consider them only at $M_\infty = 1.97$. The influence of the cross-sectional shape of the considered assemblage of cones on the distribution of pressure coefficient along the flow divergence and flow convergence lines is shown in Fig. 2. (Here, $\bar{x} = x/L$ is the dimensionless coordinate along the cone axis.) One can see that on the cone surface, the pressure coefficient in the longitudinal direction is approximately constant. The decrease of the ellipticity leads to the increase of pressure on the flow divergence line and to the decrease of pressure on the flow convergence line, and consequently enhances irregularity in the pressure coefficient distribution in the cone cross section. The comparison of pressure coefficient distribution in the base section of the cones with $\delta = 1/3$ and 1/6 with the experimental data [3] is presented in Fig. 3, which shows a good agreement between the calculation and the experiment. (Here, $\bar{z} = z/z_{\max}$ is the dimensionless coordinate, normalized by its maximum value in the considered cross section of the cone.)

The distributions of the longitudinal component of the friction drag coefficient on the flow divergence and flow convergence lines are presented in Fig. 4. According to
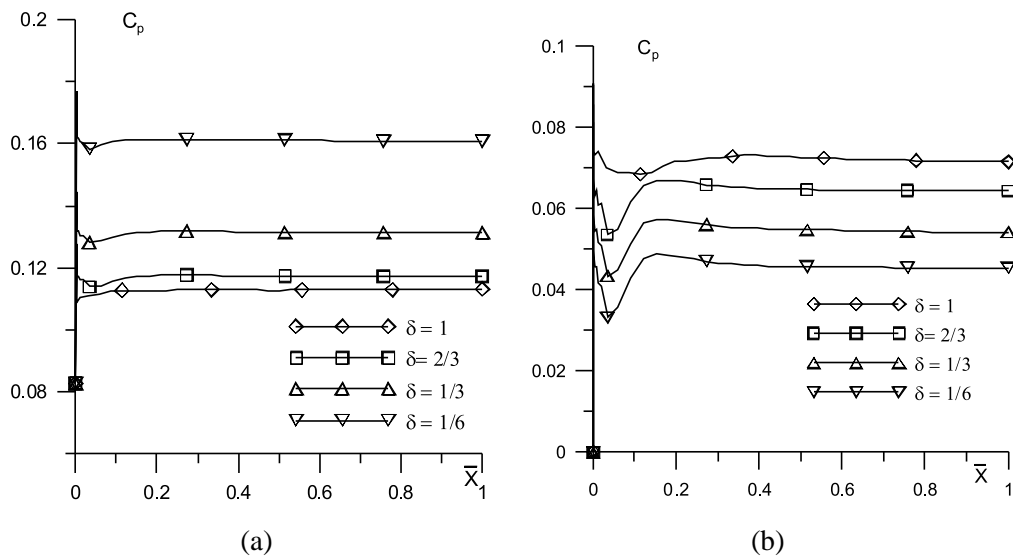
FIG. 2: Distribution of pressure coefficient c_p on the flow divergence lines (a) and on the flow convergence lines (b) of elliptical cones at zero angle of attack ($M_\infty = 1.97$, Re $= 8 \times 10^6$).
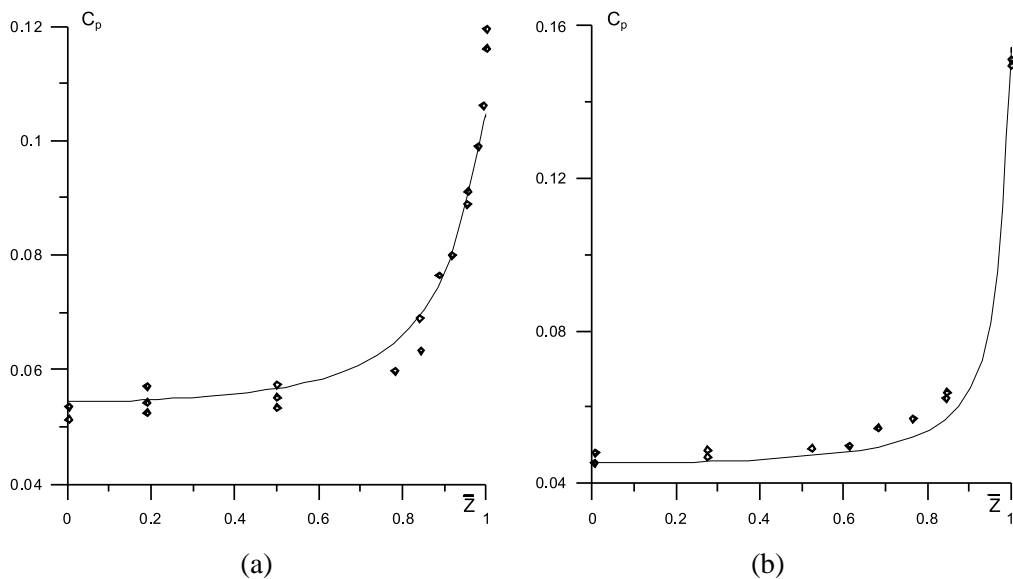
FIG. 3: Comparison of calculated and experimental distributions of pressure coefficient c_p in the midsection of an elliptical cone ($M_\infty = 1.97$, Re $= 8 \times 10^6$) (a) $\delta = 1/3$; (b) $\delta = 1/6$; —— — calculation; $\diamondsuit\diamondsuit\diamondsuit$ — experiment [3].
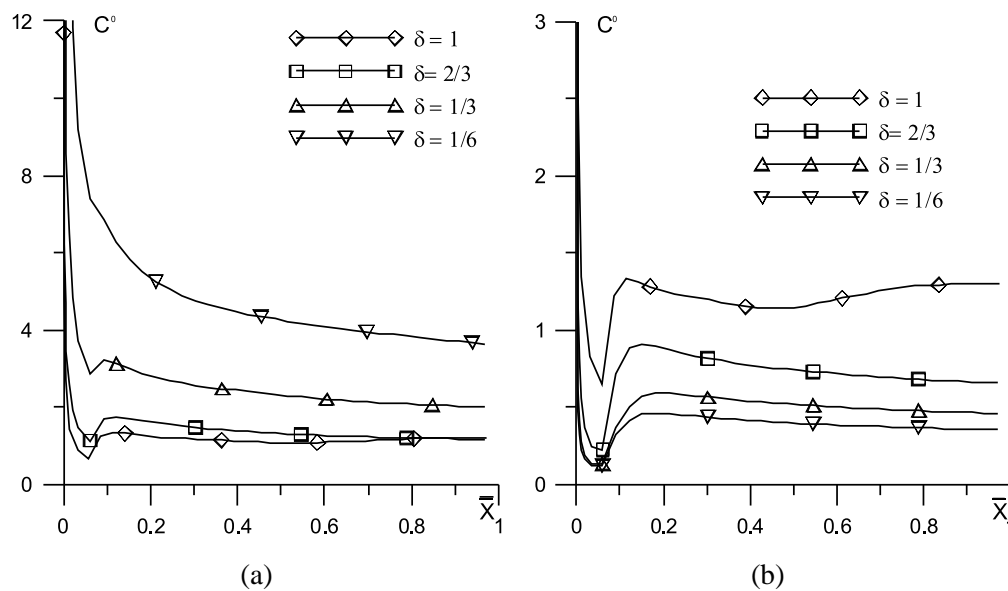
FIG. 4: Distribution of the value $C^\circ = c_{\mathrm{fr}}\sqrt{\mathrm{Re}}$ on the flow divergence lines (a) and on the flow convergence lines (b) of elliptical cones at zero angle of attack ($M_\infty = 1.97$, $\mathrm{Re} = 8 \times 10^6$).

the calculations, laminar-turbulent transition (LTT) on all the cones is observed in some vicinity of sharp body apex so that the established turbulent flow regime in the boundary layer takes place on the majority of the streamlined surface.

One can estimate how reasonably the used model of turbulence predicts the location of LTT in the boundary layer by the behavior of the integral aerodynamic characteristics of the elliptical cones. Shown in Fig. 5 is the comparison of the experimental data with the calculated pressure drag coefficients and the drag coefficients for both Mach numbers.

According to the mentioned results, frictional forces play a prominent part in the creation of drag for the considered set of elliptical cones at the given conditions of flow. The calculated results are in a good agreement with the experimental data for the pressure drag coefficient. At the same time, the results of calculations of cone drag coefficients are in a qualitative agreement with the corresponding experimental data, but exceed them quantitatively. In this case, the maximum difference between them is observed for the circular cone at $M_\infty = 1.97$ and comes to 15%. Note that the calculated data for the circular cone, the flow over which being axisymmetrical, were obtained by two different programs, namely, a 3D one and a 2D one. The results of these calculations differ somewhat by the local characteristics (the use of the 3D program leads to the slight disturbance of the flow axial symmetry) and coincide completely by the integral characteristics. Consequently, the observed difference between the calculations and the
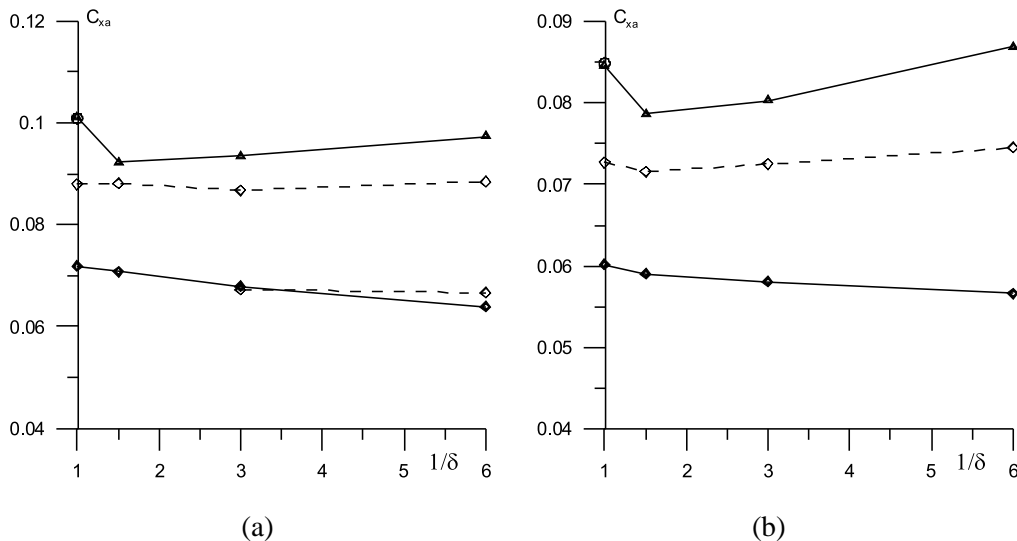
FIG. 5: Pressure drag coefficients c_{x_p} and drag coefficients c_{x_a} of sharp elliptical cones at zero angle of attack and at Mach numbers $M_\infty = 1.97$ (a) and 2.94 (b) ($Re = 8 \times 10^6$): —— — calculation; - - - - — experiment [3].

experiment is associated with the calculation of the friction drag force, which is defined by the location of LTT in the boundary layer. The following circumstance argues for this.

At $M_\infty = 1.97$, according to the calculations, the area of the transient flow on the windward side of the cone (see Fig. 4a) is situated within the limits $0.05 \leq \Delta x_{\rm tr} \leq 0.1$ and varies slightly depending on the ellipticity and the angle of attack. In Ref. [3], the location of the transition point was specified experimentally by means of the sublimator coating method. Mentioned as an instance are the pictures of the model at $\alpha = 15$ deg and $M_\infty = 1.97$ for the cones with ellipticities $\delta = 1, 2/3, 1/3$; according to these pictures, the transition points on the surface of mentioned cones are situated in the sections $\bar{x} \approx 0.31, 0.1, 0.23$, accordingly. If it is granted that this pattern is approximately the same for zero angle of attack, it becomes apparent that the maximum difference between the calculations and the experiment ($\sim 15\%$) takes place in the case of circular cone, and the minimum difference ($\sim 4\%$) takes place in the case of elliptical cone with $\delta = 2/3$.

6. NONZERO ANGLE OF ATTACK

In the presence of the angle of attack, the flow over all the elliptical cones ($\delta \leq 1$) is essentially spatial. In addition, at the angles of attack $\alpha \leq \alpha_S$, a cone is streamlined without separation and at $\alpha > \alpha_S$, one observes a transverse separation of flow on the leeward side of a cone. Here, α_S is the angle of attack at which a transverse separation of flow arises for the first time on the leeward side of a body; its value depends on the

key parameters of the problem. For example, $\alpha_S \approx 8 \ \mathrm{deg}$ for the circular cone at the considered flow conditions, and its value diminishes as the ellipticity decreases. At flow over a cone without separation, the flow convergence line is situated on its leeward side in the flow symmetry plane. In the presence of transverse separation on the leeward side, the flow convergence line is replaced by the flow divergence line. The different local characteristics respond to this change of the flow pattern in different ways, as will be shown later.
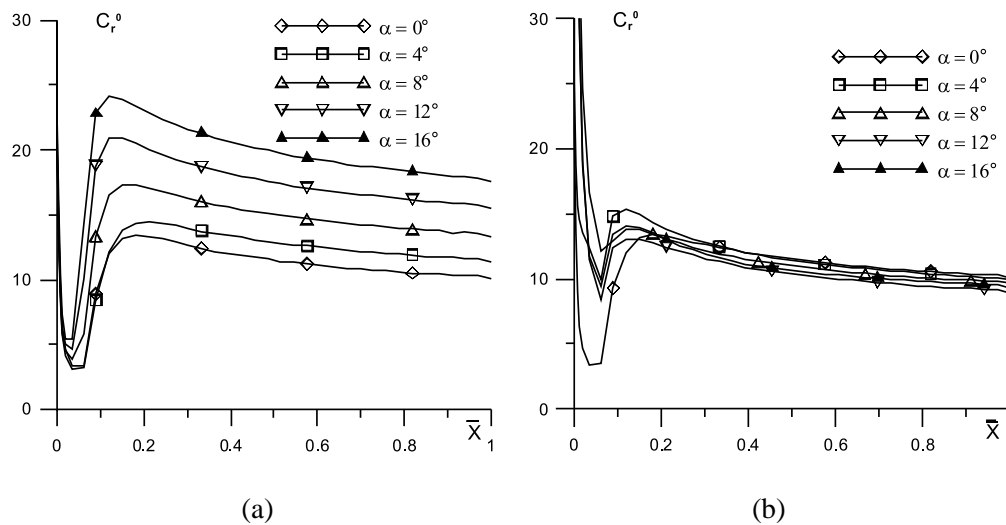
The influence of the angle of attack on the behavior of c_p is the same for all the cones—the increase of the angle of attack leads to the monotonous increase of the pressure coefficient on the windward side and to its monotonous decrease on the leeward side. Shown in Fig. 6 is the distribution of the pressure coefficient in the flow symmetry plane for the elliptical cone with $\delta = 1/6$. In this case, in the fixed meridian section of the cone, the value of c_p at $x > 0.1$ is approximately constant in the longitudinal direction, both on the windward and on the leeward sides of the cone.

Analysis of the calculated results showed that at all the angles of attack, the LTT was observed in the vicinity of the sharp apex for the considered cones, and at $x > 0.2$, the established turbulent regime of flow was realized in the boundary layer. This can be inferred from Fig. 7, where the behavior of the longitudinal friction drag coefficient in the symmetry plane on the surface of the elliptical cone with $\delta = 1/6$ is shown.

As was mentioned above, the flow convergence lines are situated in the considered symmetry plane on the elliptical cone surface at zero angle of attack. Starting with the same conditions, the longitudinal friction drag coefficient varies differently on the wind-
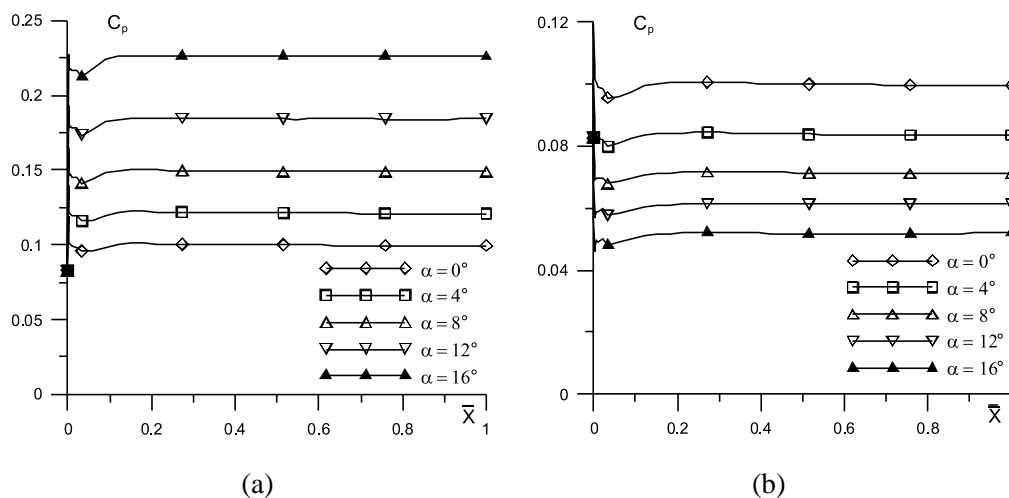
FIG. 6: Influence of the angle of attack α on the behavior of pressure coefficient c_p in the symmetry plane on the windward (a) and leeward (b) sides of the elliptical cone ($\delta = 1/6$, $M_\infty = 2.94$, $Re = 8 \times 10^6$) ——— calculation; ▲△ ◯ ◇ — experiment [3].

(a)   (b)

FIG. 7: Influence of the angle of attack α on the behavior of the value $C^\circ = c_{\mathrm{fr}}\sqrt{\mathrm{Re}}$ in the symmetry plane on the windward (a) and leeward (b) sides of the elliptical cone ($\delta = 1/6$, ($M_\infty = 2.94$, $\mathrm{Re} = 8 \times 10^6$) —— — calculation; ▲△ ◯ ◇ — experiment [3].

ward and leeward sides of a cone, depending on the angle of attack. As the angle of attack increases, it increases monotonously on the windward side and varies slightly on most of the leeward side, the corresponding curves being located in a quite narrow strip. This fact is associated with the variation of the flow pattern, which leads to the replacement of the flow convergence line by the flow divergence line, and of the pressure on the cone surface. Both factors act in the same direction on the windward side and in opposite directions on the leeward side.

The calculated results of the integral characteristics of the elliptical cones at $M_\infty = 2.94$ are compared with the corresponding experimental data in Ref. [3]. In Figs. 8–11, one can see that on the whole the calculation and the experiment are in a good agreement by all the considered characteristics. Note that at a fixed angle of attack, the elliptical cone provides higher values of aerodynamic characteristics than the circular one.

7. CONCLUSION

Fulfilled was the theoretical investigation of the supersonic perfect gas flow over the set of sharp elliptical cones at small and moderate angles of attack and $\mathrm{Re} = 8 \times 10^6$, where the laminar-turbulent regime of flow takes place. The comparison of calculated and experimental data for the integral aerodynamic coefficients of cones depending on the angle of attack showed good agreement on the whole. This circumstance points out the fact that the method of numerical simulation based on Reynolds equations with the
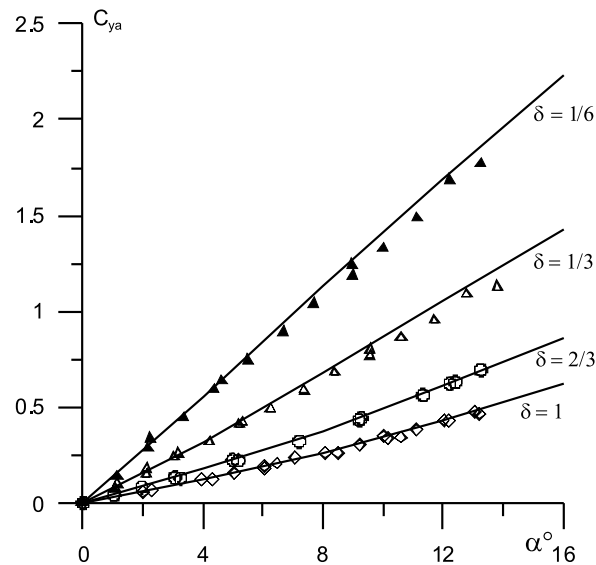
FIG. 8: Influence of the angle of attack α on the lift coefficient c_{y_a} of sharp elliptical cones ($M_\infty = 2.94$, $Re = 8 \times 10^6$):——— calculation; ▲△ ◯ ◇ — experiment [3].
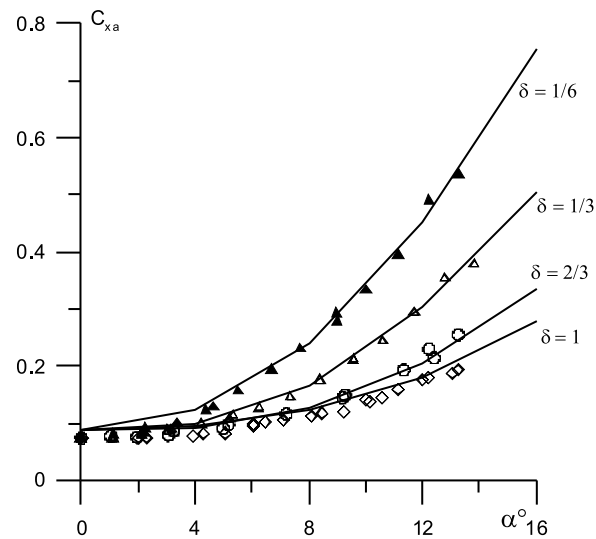
FIG. 9: Influence of the angle of attack α on the drag coefficient c_{x_a} of sharp elliptical cones ($M_\infty = 2.94$, $Re = 8 \times 10^6$): ——— calculation; ▲△ ◯ ◇ — experiment [3].

use of the differential two-parameter ($q - \omega$) turbulence model allows one to obtain reliable information about the local and integral aerodynamic characteristics of a body.

FIG. 10: Influence of the angle of attack α on the lift-drag ratio K of sharp elliptical cones ($M_\infty = 2.94$, Re $= 8 \times 10^6$):——— — calculation; ▲ $\triangle$ ◯ ◇ — experiment [3].
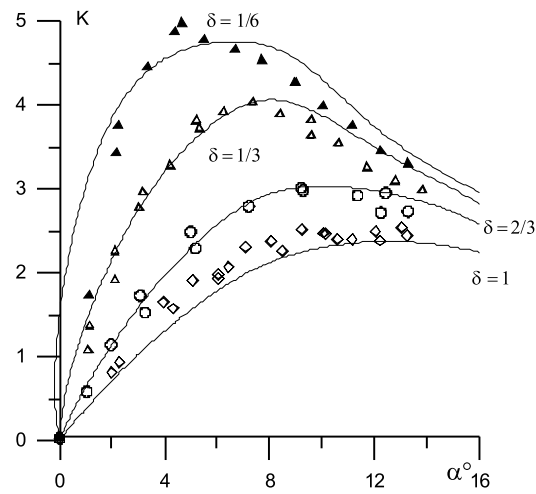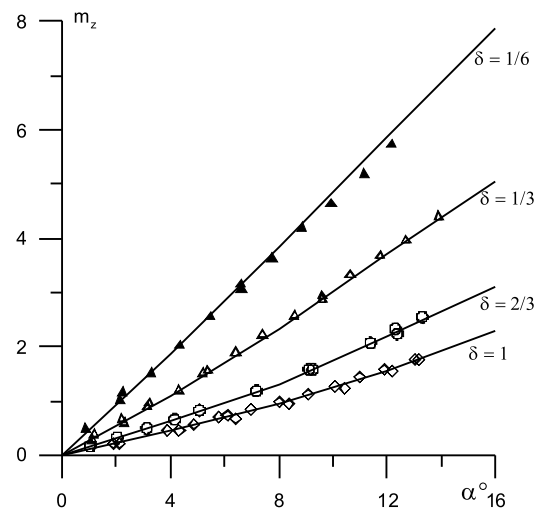

FIG. 11: IInfluence of the angle of attack α on the pitch moment coefficient m_z of sharp elliptical cones ($M_\infty = 2.94$, Re $= 8 \times 10^6$):——— — calculation; ▲ $\triangle$ ◯ ◇ — experiment [3].

ACKNOWLEDGMENT

REFERENCES

1. Bashkin, V. A., Egorov, I. V., Ivanov, D. V., and Pafnutiev, V. V., Spatial supersonic laminar flow over axially symmetrical bodies, *Comput. Math. Math. Phys.*, vol. 42, no. 12, pp. 1864–1874, 2002.

2. Bashkin, V. A., Egorov, I. V., Ivanov, D. V., and Plyashechnik, V. I., Theoretical and experimental investigation of the supersonic gas flow over a thin sharp circular cone at an angle of attack, *Proc. of Russian Acad. Sci., Fluid Dyn.*, no. 1, pp. 123–133, 2003.

3. Jorgensen, L. H., Elliptic cones alone and with wings at supersonic speeds, NACA Report No. 1376, 1957.

4. Chen, Yu. Yu., Experimental investigation of a circular cone, established at an angle of attack in the hypersonic flow, *AIAA J.,* vol. 7, no. 10, 1969.

5. Coakley, T. J. and Huang, P. G., Turbulence modeling for high speed flows, AIAA Paper No. 92-0436, 1993.

6. Bashkin, V. A., Egorov, I. V., Ivanov, D. V., and Pafnutiev, V. V., Sharp circular cone in the supersonic flow of viscous perfect gas, *Uchenye zapiski TsAGI*, vol. XXXIV, no. 3–4, pp. 3–14, 2003.

7. Bashkin, V. A., Egorov, I. V., and Pafnutiev, V. V., Aerodynamic heating of a thin sharp circular cone in the supersonic flow, *Proc. Russian Acad. Sci., High Temp.*, vol. 42, no. 5, pp. 732–744, 2005.

PECULIARITIES OF DGM APPLICATION FOR SOLUTION OF 3D EULER AND NAVIER–STOKES EQUATIONS ON UNSTRUCTURED HEXAHEDRAL GRIDS

A. V. Wolkov

Central Aerohydrodynamic Institute (TsAGI) 1, Zhukovsky str., Zhukovsky, 140180, Moscow region, Russia; Email: andrey.wolkov@mail.ru

A discontinuous Galerkin method (DGM) reported earlier in Refs. [1–3] has been developed for 3D Euler and Navier–Stokes equations on unstructured hexahedral grids. The algorithm enables calculations up to the fourth order and consideration of the curvature of the boundary. An ambitious approach combining the p-multigrid method and the conventional agglomeration h-multigrid method is applied as the convergence acceleration method. A variety of test cases is applied to validate the order of accuracy and to evaluate memory and central processing unit (CPU) requirements. Test cases shown in this paper cover the inviscid flow around a cylinder, the laminar flat plate, 3D flow in a bend duct, 3D turbulent flow over an isolated wing, as well as an aero-acoustic test case for the linearized Euler equations for propagation of a 3D acoustic wave. Results of calculations and CPU requirements are compared with the results obtained through the finite volume method.

KEY WORDS: *discontinuous Galerkin method, finite volume method, high-order scheme*

1. INTRODUCTION

An increase of the accuracy of calculation of flow over bodies with complex geometry requires very small computational grids. A convincing demonstration of this fact is presented in proceedings of a well-known forum dedicated to accurate calculations of the drag of aircraft cruiser configurations (drag prediction workshops—DPWs [4]). It is noticed there that even the grids with cells numbering more than 20 million nodes turn out to be insufficient for the description of such relatively simple geometries as "wing+fuselage". Not only do the type and density of computational grids critically impact the results, but also the turbulence model used. Therefore, the influence of different grid parameters and turbulent model parameters on the accuracy of calculations is usually investigated. Meanwhile, order of accuracy of schemes is not considered, since all the industrial computational codes are based on second-order finite volume methods.

The applicability of high-order schemes to the solution of outer aerodynamics problems is discussed in Ref. [5]. The possibility of creating a reliable, highly accurate algorithm of the Reynolds equations solutions of flow over bodies with complex geometry is investigated there. As an example, calculation of the Boeing 747-200 is considered on the basis of block-structured grids.

One of the most prospective approaches to high-precision approximation both on structured and on unstructured grids is a discontinuous Galerkin method (DGM) [6, 7]. In recent years this method has aroused high interest among investigators due to its generality, flexibility, and reliable theoretical validity. Therefore, it is not surprising that this method has been investigated intensively for the solution of three-dimensional (3D) flows. For example, the DGM is used on structured grids in Refs. [8–10] and on tetrahedral unstructured grids in Ref. [11]. Certainly, other high-order methods can be used as alternatives to the finite volume method of second order. Given in Ref. [12] is an overview of different approaches to a high-precision approximation.

The hexahedral unstructured grids are shown to be advantageous during the computation of 3D flows as compared to tetrahedral ones (Ref. [13]). That is why DGM is adapted to the solution of Euler and Navier–Stokes equations, especially on hexahedral unstructured grids.

The present paper shows the results of further development of investigations described in Refs. [1–3]. The DGM was applied for the first time to the solution of 3D Navier–Stokes equations using hexahedral unstructured grids. The computational scheme algorithm enables calculations to be fulfilled up to the fourth order. In order to achieve a higher order of precision, consideration of the curvature of the airfoil is added to the computational scheme. The original multigrid method of convergence acceleration (p-multigrid convergence acceleration method together with a conventional agglomeration h-multigrid approach) is implemented. The results of testing the algorithm precision order and the evaluation of central processing unit (CPU) requirements are shown in the paper in the examples of different test problems. Solutions of the problems of nonviscous flow over the cylinder, laminar flow over the plane, 3D viscous flow in a bend duct, and 3D turbulent flow over an isolated wing are considered. Propagation of a 3D acoustic wave described by the linearized Euler equations is shown too.

Computational results and CPU requirements are compared with the results of the industrial computational code FINE$^{\text{TM}}$/Hexa (NUMECA Int., Belgium) based on the second-order finite volume method that is widely used at the present time.

2. DGM AND CURRENT EQUATIONS

Let us consider the system of Navier–Stokes equations in a conservative form:

$$\frac{\partial \mathbf{U}\left(t,\ \mathbf{x}\right)}{\partial t} + \nabla\left(\mathbf{F} - \mathbf{F}_v\right) = \mathbf{S}. \tag{1}$$

Here $\mathbf{U}$ is a vector of conservative variables $\mathbf{U} = (\rho,\ \rho u, \rho v, \rho w, \rho E)$, $\mathbf{F(U)}$ is a non-viscous flow, $\mathbf{F}_v (\mathbf{U}, \nabla \mathbf{U})$ is a viscous flow, and $\mathbf{S}$ is a source term arising while using the turbulence model. The equation system (1) is solved computationally on the basis of the DGM, and the solution in each cell is stored in the primitive variables $\mathbf{Q} = (\rho, u, v, w, p)$. Meanwhile the pressure value p is related to the total energy value E by the state equation.

Navier–Stokes equations can be overwritten in primitive variables as follows:

$$\mathbf{\Gamma}\frac{\partial \mathbf{Q}}{\partial t} + \nabla \cdot (\mathbf{F}(\mathbf{U}) - \mathbf{F}_v (\mathbf{U}, \nabla \mathbf{U})) - \mathbf{S} = 0, \tag{2}$$

where

$$\mathbf{\Gamma} = \left(\frac{\partial \mathbf{U}}{\partial \mathbf{Q}} \right) \tag{3}$$

is a Jacobian matrix of transformation from the conservative variables to the primitive ones.

Local polynomial basic functions are determined in each cell of the grid:

$$\mathbf{Q}(t, \mathbf{x}) = \sum_{j=1}^{K_f} \mathbf{u}_j (t)\, \varphi_j (\mathbf{x}), \tag{4}$$

where $\mathbf{u}_j (t)$ are expansion coefficients determined in the solution process, and K_f is a number of basic functions in a cell. The K_f value is related to the maximum order of the basic polynomial K as follows:

$$K_f = \frac{(K+1)(K+2)(K+3)}{6}. \tag{5}$$

The polynomial order K possesses the values $K = 0, 1, 2, 3$ in the present paper, and thereby the number of basic functions takes on the values $K_f = 1, 4, 10, 20$. For $K = 3$ the following set of basic functions is used:

j	0	1	2	3	4	5	6	7	8	9
φ_j	1	X	y	z	x^2	y^2	z^2	xy	xz	yz
j	10	11	12	13	14	15	16	17	18	19
φ_j	x^3	y^3	z^3	x^2y	x^2z	y^2x	y^2z	z^2x	z^2y	xyz

Basic functions are normalized in the following way:

$$\varphi_1 = \frac{(x - x_0)}{h_x}, \quad \ldots, \quad \varphi_8 = \frac{(x - x_0)(z - z_0)}{h_x h_z},$$

$$\varphi_9 = \frac{(y - y_0)(z - z_0)}{h_y h_z}, \quad \ldots, \quad \varphi_{19} = \frac{(x - x_0)(y - y_0)(z - z_0)}{h_x h_y h_z}. \tag{6}$$

Here x_0, y_0, z_0 are the coordinates of the central point of the considered hexahedron, and the values h_x, h_y, h_z determine the cell dimensions along the corresponding axes. It is shown that it is this normalization that ensures superior accuracy and convergence, especially in the case of viscous problems with much extended grid cells.

The system of grid equations for the coefficients $\mathbf{u}_j(t)$ of Eq. (4) is obtained using the standard Galerkin finite element procedure when the orthogonality of misclosure of solved equations is required [left part of system (2)] to each basis function being used in the solution reconstruction. This requirement of orthogonality is formulated through the zero equality of the integral of the product of equation system on each of the basis functions $\varphi_i \, (i = 1, \ldots, K_f)$. After partial integration we have

$$\frac{d}{dt} \int_\Omega \varphi_i \boldsymbol{\Gamma} \mathbf{Q} d\Omega = - \int_\Sigma \varphi_i \left(\mathbf{F} - \mathbf{F}_v \right) d\Sigma + \int_\Omega \nabla \varphi_i \left(\mathbf{F} - \mathbf{F}_v \right) d\Omega + \int_\Omega \varphi_i \mathbf{S} d\Omega. \quad (7)$$

Here $d\Sigma$ is an area element oriented in the direction of the normal $\mathbf{n} = (n_x, n_y, n_z)$, and $d\Omega$ is the element of cell volume.

Equation (7) consists of volume integrals and of surface integrals over the cell boundary. The values of all dependent variables have discontinuity at the boundaries of elements; therefore, the rules of calculation of variables and of flows on these boundaries play a crucial role. Like in the finite volume method (FVM), the value of nonviscous flow through the boundary between two cells is determined in DGM from the solution of the Riemann problem for the decay of arbitrary discontinuity. An approximate, linearized technique of Riemann problem solution, proposed by Row, is used in the present paper:

$$\mathbf{F}_{\text{bound}} = \frac{1}{2} \left(\mathbf{F}^L + \mathbf{F}^R \right) - \frac{1}{2} |\mathbf{A}| \left(\mathbf{U}^L - \mathbf{U}^R \right). \quad (8)$$

Here the superscripts L and R designate that the corresponding values are calculated from the left and the right sides of the interface, respectively, and A is a Jacobian matrix of nonviscous flow:

$$\mathbf{A} = \frac{\partial \mathbf{F}}{\partial \mathbf{U}}. \quad (9)$$

The viscous flows are determined through the gradients of primitive variables $\mathbf{F}_v = \mathbf{F}_v \left(\mathbf{Q}_h, \nabla \mathbf{Q}_h \right)$, where $\nabla \mathbf{Q}_h = (\partial \mathbf{Q}_h / \partial x, \partial \mathbf{Q}_h / \partial y, \partial \mathbf{Q}_h / \partial z)$. The gradients of primitive variables can be obtained from the direct derivation of Eq. (4) for the solution reconstruction in a cell. However, as it is shown in Ref. [7], such a method of gradient calculations is a reason for the absence of approximation. Therefore in DGM the gradients of primitive variables are also presented as a linear combination of basis functions in order to calculate viscous flows:

$$\frac{\partial \mathbf{Q}}{\partial x_i} \left(t, \mathbf{x} \right) = \sum_{j=1}^{K_f} \mathbf{g}_{i,j} \left(t \right) \varphi_j \left(\mathbf{x} \right). \quad (10)$$

Here $i = 1, 2, 3$ corresponds to x, y, and z coordinates. After multiplication of Eq. (10) on test functions (for the Galerkin method the test functions are the basis ones) and after the partial integration, we obtain the following system of linear equations for the expansion coefficients $\mathbf{g}_{i,j}$:

$$\int\limits_{\Omega} \sum_{j=1}^{K_f} \mathbf{g}_{i,j}\varphi_j\varphi_k d\Omega + \int\limits_{\Sigma} \varphi_k \mathbf{Q} n_i d\Sigma - \int\limits_{\Omega} \frac{\partial\varphi_k}{\partial x_i}\mathbf{Q}d\Omega = 0; \quad k = 1, \ ..., \ K_f. \quad (11)$$

The solution of this system determines the gradients of primitive variables (10) and allows calculating viscous flows in a cell.

Both gradients of primitive variables and values of flows have discontinuities at cell boundaries in DGM. However, these values are required for calculation of contour integrals and they cannot be found through averaging. The approximation rules [7] require alternating choice of left and right cell for the solution reconstruction at the boundary. Thus, if the values of primitive variables and their gradients are selected from the left cell while calculating viscous flows (7)

$$\mathbf{F}_v|_b = \mathbf{F}_v\left(\mathbf{Q}^L, \nabla\mathbf{Q}^L\right), \quad (12)$$

then in Eq. (11) the values of primitive variables while calculating the contour integral should be chosen from the right cell

$$\mathbf{Q}|_b = \mathbf{Q}^R. \quad (13)$$

Finally, the system of nonlinear equations for the coefficients $\mathbf{u}_i\left(t\right)$ of Eq. (4) is obtained from Eq. (7) under the assumption of a small variation of Jacobian matrix $\mathbf{\Gamma}$ (3) inside the cell:

$$\frac{du_i}{dt} = \mathbf{\Gamma}^{-1}\mathbf{M}^{-1}\left[-\int_{\Sigma}\varphi_i\left(\mathbf{F}-\mathbf{F}_v\right)d\Sigma + \int_{\Omega}\nabla\varphi_i\left(\mathbf{F}-\mathbf{F}_v\right)d\Omega + \int_{\Omega}\varphi_i\mathbf{S}d\Omega\right]. \quad (14)$$

Here $\mathbf{M}$ is a matrix of masses, $i = 1, \ \ldots, \ K_f$.

3. CALCULATION OF INTEGRALS AND ACCOUNTING OF CURVATURE

The high order of approximation of DGM assumes the accurate calculation of volume and of surface integrals in the system of equations (14). In order to calculate the integrals, quadrature Gauss formulas are applied. Calculation of the volume integral inside a hexahedron of arbitrary form is executed in a parametrical space in which every hexahedral element has the form of a unit cube. This triquadratic isoparametric transformation is built on the basis of 20 nodes, 8 of which are cube corners, and 12 nodes at the centers of all cube edges. The presence of central nodes on edges enables the curvature of the

streamlined boundary to be taken into account. With this approach the surface and the volume integrals contain nonlinear Jacobian transformations, which demands higher requirements to quadrature formulas of integration and requires more Gauss points. Thus, calculation of the volume integrals requires application of quadratures that are accurate for the polynomials of 3 K order.

The amount of calculations can be reduced when using the nonquadrature approach proposed in Ref. [14]. This approach was used only for rough levels of the multigrid solver.

It is commonly known that obtaining a high order of accuracy requires consideration of the streamlined boundary curvature. The application of a 20-point transformation for boundary integrals can be avoided while calculating the flows of nonviscous fluid. Meanwhile the original approach proposed in Ref. [15] can be used. In nonviscous flow, the boundary condition on the streamlined body is formulated as the requirement of equality to zero velocity component normal to the body. Shown in Ref. [15] is the fact that for account of the correct curvature in nonviscous flow it would be sufficient to use only the "proper" direction of normals, oriented strictly normally to the true curved boundary at every Gauss point. Meanwhile the integration itself is implemented on a hexahedron, disregarding its curvature near the boundary.

The right direction of normals to the streamlined boundary can be obtained either during the construction of biquadratic transformation of a curved surface quadrangle into a plane square, or from calculation of the normals of the original surface set in a system of automated design.

Shown in Fig. 1 is the approximation of the leading edge of the airfoil LANN [21], where a polygonal presentation of contour, biquadratic interpolation of surface, and real
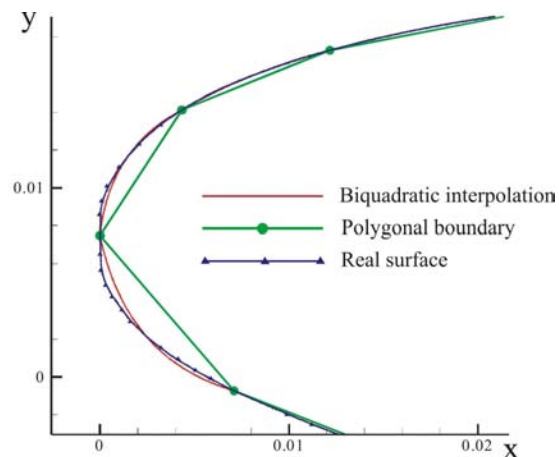

FIG. 1: The leading edge of the airfoil LANN [21]. Comparison of the polygonal boundary of the grid with biquadratic interpolation of the surface and with the real surface.

geometry are compared. Presented in Fig. 2 is the value of error in the calculation of the normal to the cylinder surface in the case of polygonal presentation of the boundary and of biquadratic interpolation. Here the value of error $\sqrt{\left(\sum_{i=1,M}\left(1-\mathbf{n}_i\mathbf{N}_i\right)^2\right)/M}$ depends on the number of cylinder surface partitions. $\mathbf{N}_i$ designates the normal at i point, $\mathbf{n}_i$ is a precise normal, and M is the total number of checkpoints on the cylinder surface. It is seen that the biquadratic interpolation ensures a more precise description of the surface.

4. SOLUTION OF A SYSTEM OF GRID EQUATIONS AND A MULTIGRID SOLUTION ACCELERATION METHOD

The solution of a system of grid equations (14) is executed by means of an explicit method of time integration. The search for a stationary solution enables use of the local time step depending on cell dimension; this fact accelerates the convergence process appreciably, i.e., the misclosure tendency [right part of Eq. (7)] to computer zero. A five-step Runge–Kutta method is used. This method ensures maximum stability of the procedure, or, in other words, rapid diminishing of misclosure during the time iteration process.

The implementation of an explicit Runge–Kutta method of solution search requires virtually no additional memory resources. However, in spite of the local time step and the presence of a multistep scheme, the number of iterations required for attainment of
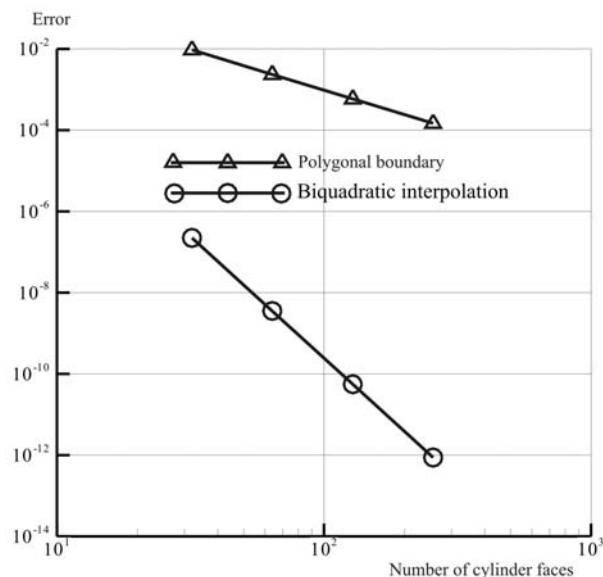
FIG. 2: Error in the determination of a normal to the cylinder surface as a function of the number of boundary points.

the stationary solution is too high. Significant acceleration of solution is achieved by implementation of a multigrid method.

The multigrid method is an effective approach for solution acceleration of mathematical physics problems. The main idea of this method consists of the quick transmission of information between different parts of the computational grid. For this purpose in the classical multigrid method (a so-called h-multigrid method) the solution of determinative equations is fulfilled on a set of successively finer grids. A coarse grid solution is used for determination of a fine grid solution and vice versa, and the fine grid solution is used as an initial approximation for the coarse grid solution. Meanwhile, the determinative equations on a coarse grid are modified in order to take into account the approximation inaccuracy on coarse cells. On each grid level the Runge–Kutta method (or other solution method) ensures effective suppression of high-frequency errors. However, high-frequency errors on a coarse grid are low-frequency ones on a fine grid. Therefore, a few variables on a coarse grid enable quick determination of all low-frequency peculiarities of flow. The conversion of the coarse grid solution to the fine grid solution allows acceleration of information transmission and correction of the low-frequency component of the basis solution.

In the finite element method the solution in each element is a linear combination of basis functions. This combination forms a polynomial reconstruction of maximum order K. The coefficients before basis functions are the required degrees of freedom. The hierarchical basis functions are used in the present paper. This means that the coefficients before basis functions in the solution expansion have clear mathematical meaning, notably, they express the value of averaged solution in a cell, the value of solution gradient in three directions, the second derivative of solution, etc. Therefore, given these basis functions, the solution is presented in terms of Taylor expansion in a cell. In other words, the coefficients in the solution reconstruction express the contribution of different harmonics in the solution.

The ideas of the p-multigrid method (Refs. [16–18]) for the finite element approach are similar to the ideas of the classical multigrid method described above. The decrease or increase of maximum order (K) of the polynomials of basis functions or, in other words, the variation of a set of basis functions in the element is similar to the coarsening or to the refinement of cells inside the grid. The application of basis functions of low order ($K = 0$) enables quick determination of the low-frequency solution component and correction of the total solution at a maximum set of basis functions.

In the present paper, the greatest gain in convergence acceleration resulted from combining the conventional multigrid method with the p-multigrid method. The agglomeration multigrid method [19] realized in the solver of industrial code [22] is used as the basis of the conventional multigrid method. This method is used in solving using the simplest approximation scheme ($K = 0$, one piecewise constant function). Then the successive increase of the number of basis functions is executed on the finest grid, i.e., the p-multigrid method is realized.

5. TEST CALCULATIONS

The peculiarities of the DGM scheme up to the fourth order ($K = 3$) are investigated in the process of solving of a series of test problems that cover 3D nonviscous, viscous, and turbulent flows. The results are compared with data obtained through the FVM (finite volume method) [22].

The agglomeration three-level multigrid method is used for the solution acceleration in the second-order FVM. The four-level method is implemented in DGM ($K = 1$). The first three levels represent the conventional multigrid method where piecewise constant functions are used ($K = 0$). On the fourth level the approximation of equation system is fulfilled on a fine grid but on the basis of piecewise linear functions ($K = 1$). The solution for DGM ($K = 2$) is found using the fifth level, the sixth level implemented for DGM ($K = 3$). In all cases the five-step Runge–Kutta method is used as a smoothing procedure for the high-frequency component of error.

5.1. Nonviscous Flow Over a Cylinder at Mach Number M = 0.15

Nonviscous potential flow over a circular cylinder is a known test case enabling the determination of numerical scheme precision order. The computation is made at low Mach numbers of incident flow (M = 0.15) when the compressibility influence is negligible. All numerical tests are fulfilled on a set of four analytical grids with dimensions varying from 16×4 to 128×32 by doubling the number of points in each direction (Fig. 3). N concentric circles contain M uniformly distributed nodes in the X-Y plane. The radius of each circle is determined by the following relationship:

$$r_j = r_0 \left(1 + \frac{2\pi}{M} \sum_{k=0}^{j-1} \alpha^k \right), \quad j = 0, \, ..., \, N. \tag{15}$$

The cylinder radius is equal to 0.5. The α parameter from Eq. (15) is determined from the condition that the radius of the maximum circle constraining the computational area is equal to 20. On the external boundary, the distant field condition based on Riemann invariants is imposed.

Presented in Fig. 4 is a computational pressure distribution coefficient in comparison with an analytical incompressible solution (dotted line). Shown in Fig. 4a are the pressure fields along the cylinder surface obtained on the most coarse grid (16×4) using DGM of the second order ($K = 1$), of the third order ($K = 2$), and of the fourth order ($K = 3$). Presented in the same figure are the results of computations using FVM [22]. Shown in Fig. 4b is the comparison of pressure fields calculated on different grids under the condition of using approximately the same quantity of unknown variables or, in other words, equal number of degrees of freedom $\Re$, determined by the product of a quantity of cells and a number of variables in a cell. The results presented demon-
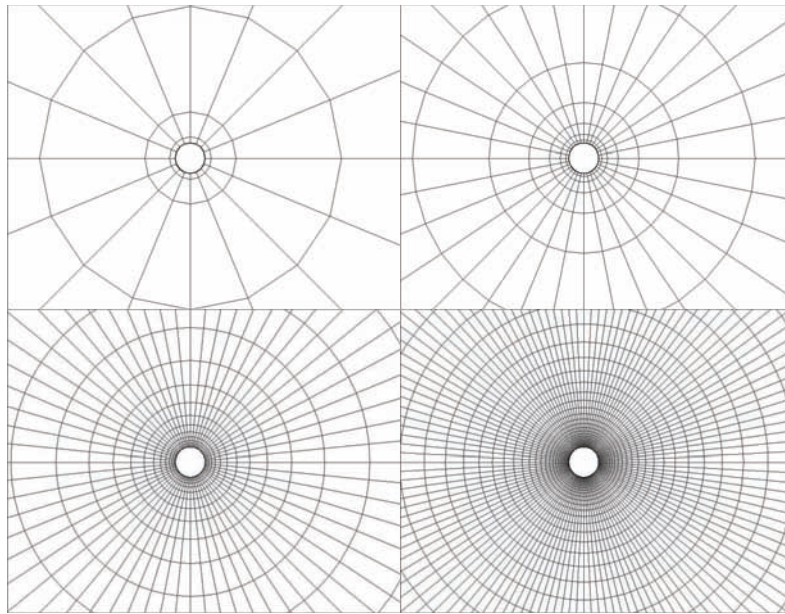
FIG. 3: Error in the determination of a normal to the cylinder surface as a function of the number of boundary points.

(a)   (b)
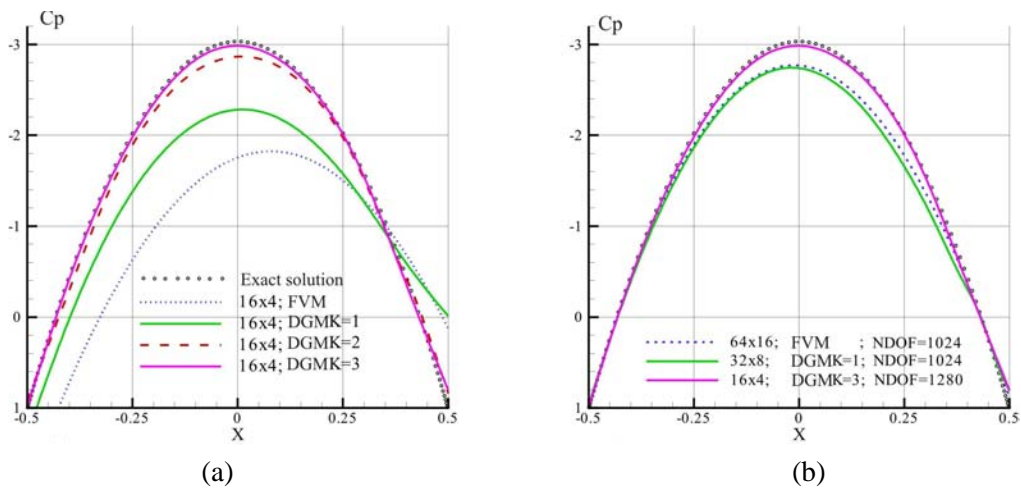
FIG. 4: Pressure distribution at the cylinder surface: (a) numerical solution for DGM $K = 1, 2, 3$ and for FVM on a coarse grid 16×4; (b) numerical solution for the schemes with an equal number of degrees of freedom.

strate that DGM provides better accuracy, even in the case of application of equivalent $\Re$ number.

The precision order of computational scheme is evaluated at entropy error value:

$$e_{\text{ent}} = \frac{p/\rho^\gamma}{p_\infty/\rho_\infty^\gamma} - 1.$$

Since the flow under consideration is isoentropic, the entropy must be equal to zero at exact solution. Shown in Table 1 are the dimension of the grid, the total number of elements in it, L_2 - the norm of entropy error, calculated over each element of the grid, the value of cylinder drag, and the obtained precision order of computational scheme. This precision order turns out to be close to the theoretical value $O\left(h^{K+1}\right)$. Precision order is calculated by the value of error diminishing at successive transition from the coarse grid $(i-1)$ to the finer one (i) using the following relationship:

$$\text{Order} = 2\frac{\lg\left[\frac{e_i}{e_{i-1}}\right]}{\lg\left[\frac{\Re_{i-1}}{\Re_i}\right]}.$$

Calculation of viscous laminar flow is executed on a sequence of grids described in the previous section at Re = 40. Precision order is evaluated on the basis of the value of cylinder total drag. Analysis of the asymptotic behavior of total drag value is fulfilled as a function of the averaged dimension of the grid cell calculated through the equation

$$h = 1/\sqrt{\Re}.$$

TABLE 1: Precision order of schemes for FVM and DGM (K = 1, 2, 3).

Grid	Number of elements	FVM			DGM $K = 1$		
		c_x	L_2, entropy error	Order	c_x	L_2, entropy error	Order
16×4	64	1.18e^{-1}	1.03e^{-2}		7.47e^{-2}	1.00e^{-2}	
32×8	256	2.73e^{-2}	3.11e^{-3}	1.73	7.34e^{-3}	2.73e^{-3}	1.88
64×16	1024	1.4e^{-3}	6.85e^{-4}	2.18	2.75e^{-3}	6.05e^{-4}	2.17
128×32	4096	9.05e^{-4}	1.36e^{-4}	2.33	1.56e^{-3}	1.18e^{-4}	2.36
Grid	Number of elements	DGM $K = 2$			DGM $K = 3$		
		c_x	L_2, entropy error	Order	c_x	L_2, entropy error	Order
16×4	64	8.94e^{-3}	5.55e^{-4}		2.66e^{-3}	1.13e^{-4}	
32×8	256	7.01e^{-4}	7.79e^{-5}	3.25	5.83e^{-5}	5.26e^{-6}	4.42
64×16	1024	2.37e^{-4}	7.50e^{-6}	2.95	6.92e^{-6}	3.66e^{-7}	3.85
128×32	4096	3.74e^{-5}	8.93e^{-7}	3.07	1.95e^{-6}	2.12e^{-8}	4.11

Viscous flow near the cylinder at M = 0.15, Re = 40.

Note that at such determination, the averaged grid step depends not only on its dimension but on the approximation method too. For FVM, in which only one variable in a cell is used, the averaged cell dimension in a uniform rectangular grid is identical to the actual step of grid.

An asymptotically limiting value of drag $c_{x*} = 1.5685$ results from the extrapolation of values from the two finest grids to the grid with infinitesimal step. Assuming $c_x^{i-1} = c_{x*} + O\left(h_{i-1}^p\right)$ and $c_x^i = c_{x*} + O\left(h_i^p\right)$, we have

$$\text{Order} = 2\frac{\lg\left[\frac{c_x^i - c_{x*}}{c_x^{i-1} - c_{x*}}\right]}{\lg\left[\frac{\Re_{i-1}}{\Re_i}\right]}.$$

The results of calculations, shown in Table 2, demonstrate the expected precision order of all considered computational schemes.

The computational area shown in Fig. 5a has the following dimensions: $-0.24 < x < 0.4$; $0 < y < 0.05$; $0 < z < 0.00625$. The plate is installed in the range $0 < x < 0.4$. Computational investigations are implemented on four generated grids, shown in Fig. 5. These 2D grids have only one cell in the z-direction. Some of the grid parameters presented in Table 3 show a number of cells in a grid, a distance from the wall surface to the first cell layer, a coefficient of distance increase between successive ranges of grid points, and a total number of nodes in y-direction. The number of elements in grid 1 is approximately four times greater than in grid 2, while grids 3 and 4 have the number of grid cells correspondingly 10 and 20 times less. Such grid selection enables comparison of different computational schemes in the case of approximately similar degrees of

TABLE 2: Drag coefficient and evaluation of scheme precision order for the problem on viscous flow over cylinder Re = 40 for FVM and for DGM K = 1, 2, 3.

Grid	Number of elements	FVM		DGM $K = 1$	
		c_x	Order	c_x	Order
16×4	64	0.403598		0.298054	
32×8	256	0.271965	1.10	0.191675	2.02
64×16	1024	0.180503	2.30	0.166170	1.90
128×32	4096	0.161464	2.46	0.159011	2.11
Grid	Number of elements	DGM $K = 2$		DGM $K = 3$	
		c_x	Order	c_x	Order
16×4	64	0.190749		0.163027	
32×8	256	0.161390	2.90	0.156464	3.99
64×16	1024	0.157401	2.05	0.156829	4.00
128×32	4096	0.156790	3.11		

Laminar flow over flat plate at M = 0.35, Re = 76,000.

(a)

(b)
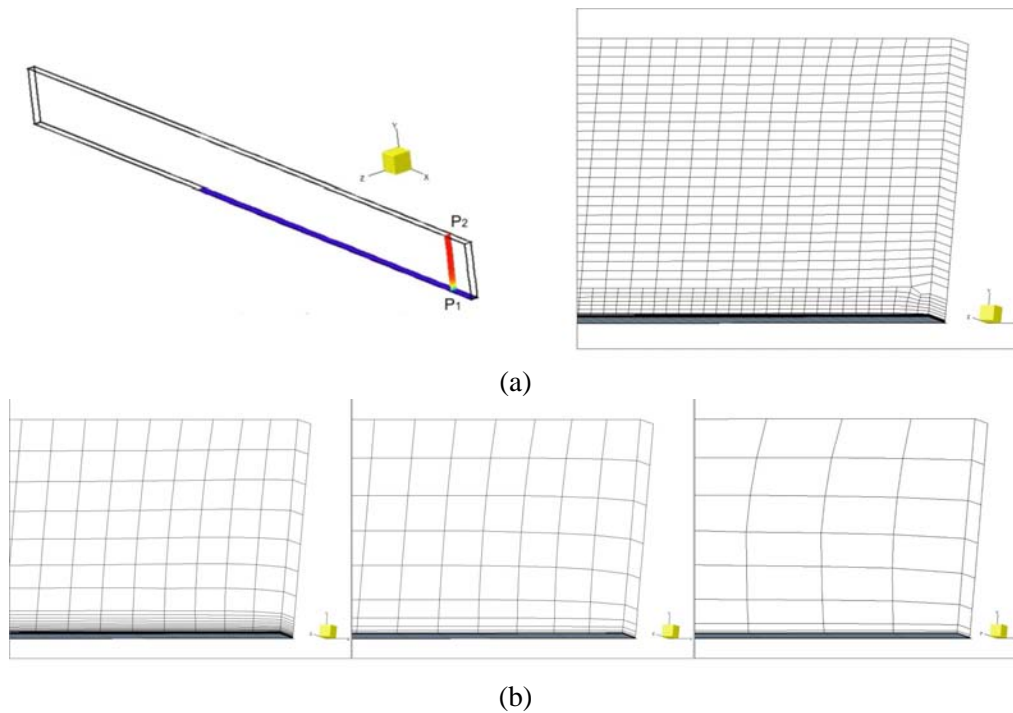
FIG. 5: Computational area and fragments of grids: (a) grid 1 and (b) grids 2, 3, 4.

TABLE 3: Grid parameters for calculation of laminar flow over the plate.

Grid	Number of cells		Distance up to the first layer $y+$	Coefficient of layer expansion	Number of grid lines in y-direction
1	6739		1×10^{-5}	1.02	25
2	1707	64	1×10^{-5}	1.20	13
3	680	64	2×10^{-5}	2.00	8
4	281	32	4×10^{-5}	2.50	5

freedom.

Some computational results are shown in Figs. 6 and 7 in terms of velocity profiles compared with a Blasius analytical solution for uncompressible flow. All dependences are presented as a combination of lines and markers. Each line is drawn through a set of points and is in precise correspondence with the equation for solution reconstruction in a cell. On each line, the markers are located approximately in the middle of cells. Thus, the number of markers on a line reproduces the density of the grid.

The U-component of velocity is shown in Fig. 6 for all the approximation schemes under investigation. All the schemes demonstrate good matching with analytical solu-
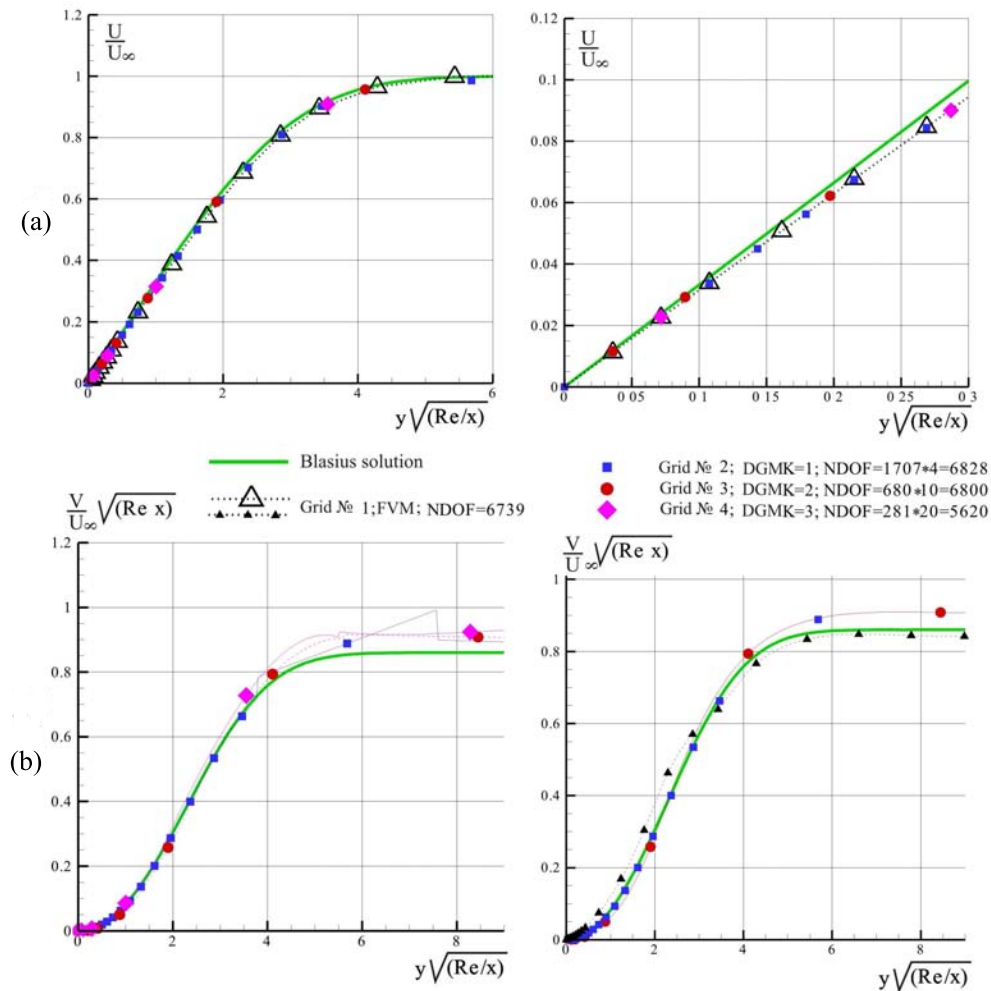
FIG. 6: Comparison of numerical schemes on different grids at the condition of similar number of degrees of freedom: (a) U-component of velocity and (b) V-component of velocity.

tion. The V-component of velocity, shown in Fig. 6b, is more sensitive to the quality of a grid. The results, obtained through DGM $K = 2$ on grid 3 and $K = 3$ on grid 4, are in better agreement with the analytical solution than the results obtained through conventional FVM on the finest grid 1, in spite of the equivalent quantity of the degrees of freedom set in motion.

Shown in Fig. 7 is the influence of scheme precision order on the V-component of the solution. The computation on the coarsest grid 4 is executed by means of DGM $K = 2$ and $K = 3$. Observed here is an appreciable improvement of matching, in spite of the extremely small number of computational grid nodes, located crosswise from the
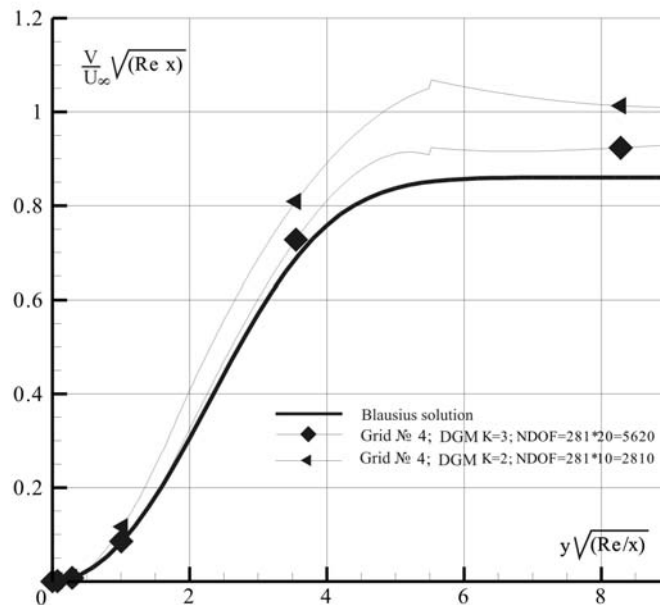
FIG. 7: Effect of increase of precision order of computational scheme from $K = 2$ up to $K = 3$ for V-component of velocity.

boundary layer.

The comparison of the distribution of local friction coefficient obtained on the coarsest grid 4 with a Blausius analytical solution is shown in Fig. 8. It is seen that in spite of the extremely coarse grid, good matching of the calculations with the exact solution is
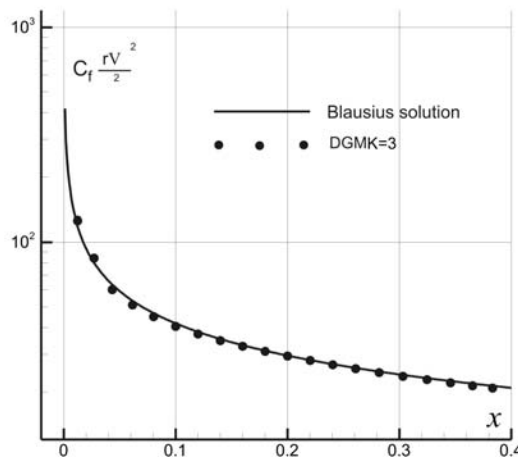
FIG. 8: Comparison of the analytical solution with DGM $K = 3$ solution, obtained on a coarse grid 4, for the local friction coefficient.
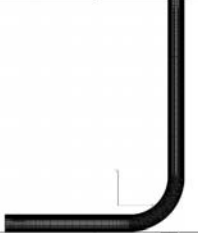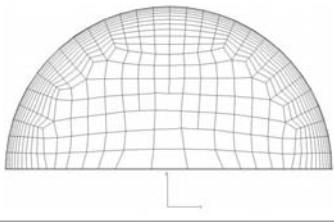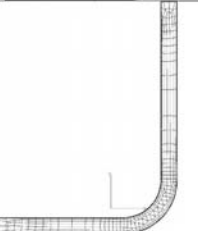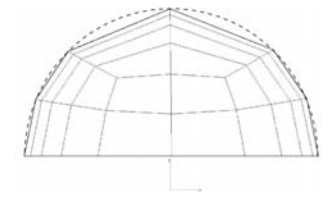
obtained.

5.2. 3D Laminar Flow in a Bend Duct

This 3D test case for laminar flow inside a 90° bend duct with a constant section is investigated experimentally [20] by laser-Doppler velocimetry with water as a working fluid. The investigations are executed at three different Reynolds numbers, including the laminar case at Re = 500. This case is considered in the present paper. The flow established in a duct, determined by the balance of viscous and nonviscous forces, is characterized by the presence of a couple of vortices swirling in opposite directions to each other, formed downstream after passing the duct bend. There are velocity profiles measured experimentally in five sections along the duct: Section 1 is at 0.58 diameter upstream from the bend, Section 2 is at 30° along the bend, Section 3 is at 60° along the bend, Section 4 is at 75° along the bend, and Section 5 is at 1 diameter downstream from the bend.

Five unstructured hexahedral grids are generated using the grid generator HEX-PRESS[TM] [13]. The number of cells in these grids varies from the finest grid to the coarsest one within the range 140,000÷2500. Some grid fragments are shown in Fig. 9. A dashed line indicates the duct surface for grid 5. The difference between the grid boundary and the real one is easily seen here. Consideration of the airfoil curvature enables this difference to be considered.

The calculations are fulfilled for all the grids using different approximation schemes. Velocity profiles at different duct sections are shown in Fig. 10. Here, the results obtained on the coarsest grid with schemes DGM $K = 2$ and 3 are compared with the experimental data. The results through the scheme DGM ($K = 3$) are seen to have good matching

Grid	Number of cells		
№1	139902		
№5	2502		

**FIG. 9:** Set of grids for the computation of laminar flow in a bend duct.
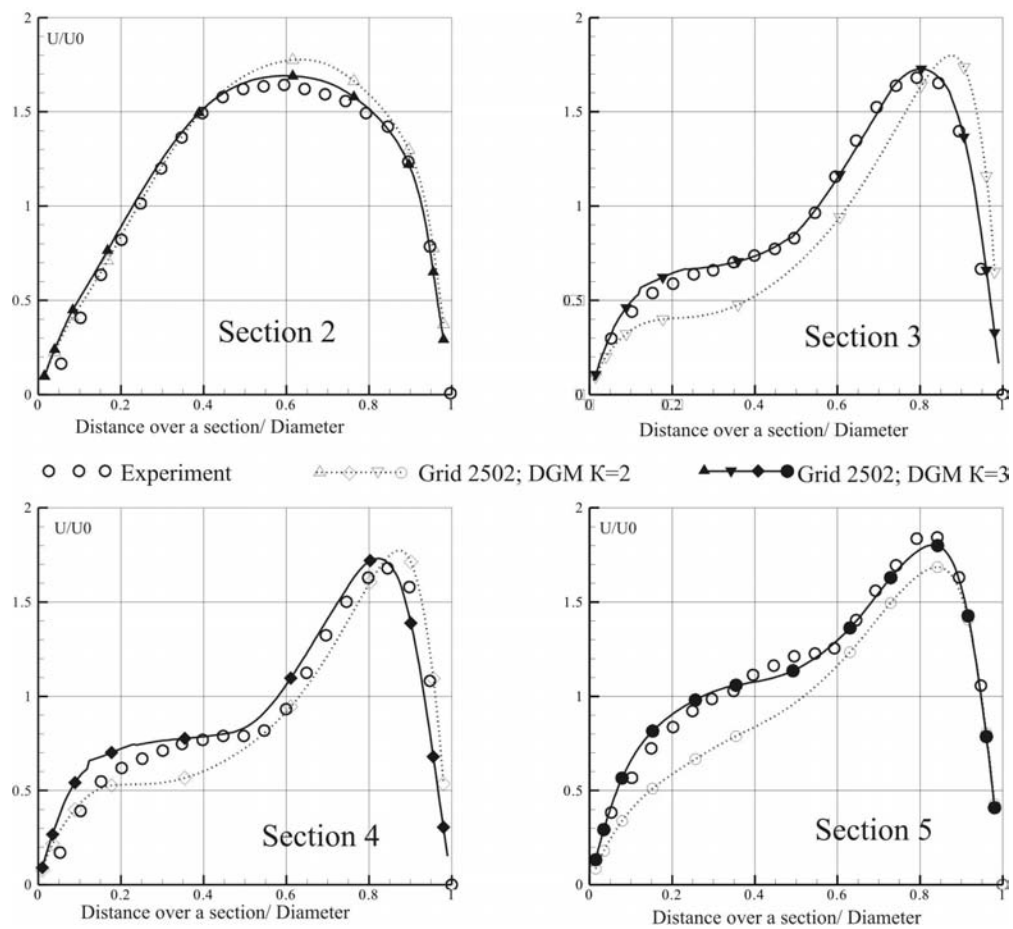
FIG. 10: Velocity profile in four sections of the duct. Comparison of the experiment with the computational results obtained through DGM $K = 2$ and 3 on a coarse grid 5.

with the experimental velocity profiles. This figure also demonstrates the effect from the increase of scheme order.

The advantages of the fourth-order scheme are also presented in Fig. 11. The velocity profiles calculated through the scheme DGM $K = 3$ on the grid with 2500 cells are compared with results from the FVM scheme [22] obtained on a dense grid containing 140,000 elements. The calculations implemented through the conventional FVM scheme on the grid with 62,000 elements are far from the experimental data. Thus, the FVM results are obtained with satisfactory precision only on the grid with 140,000 nodes.

A comparison of computational consumption is shown in Table 4. It is seen that the time spent on the four-order DGM scheme is three times longer than the FVM scheme, provided that the equivalent number of degrees of freedom is used (the 62,000 grid). Taking into account the more precise results of DGM, it is better to compare total time
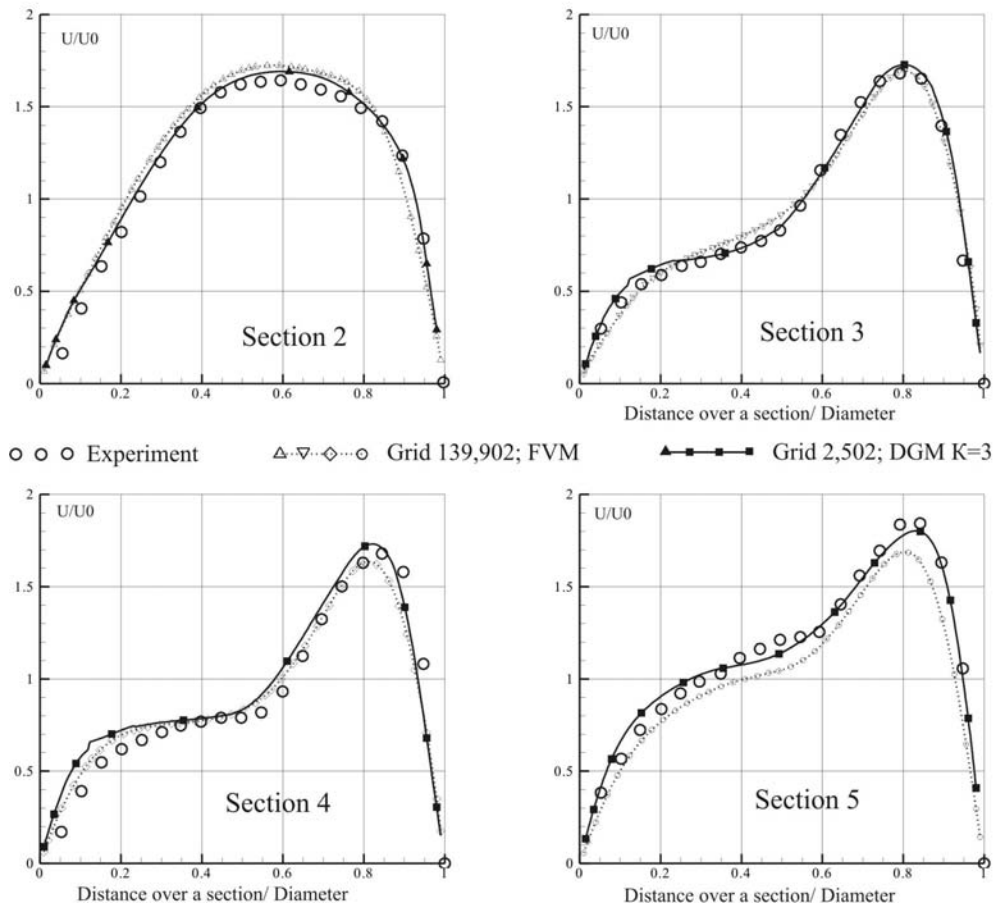
FIG. 11: Comparison of the experiment with the computational results obtained through DGM $K = 3$ coarse grid 5 and through FVM on grid 1.

of computational schemes required for obtaining results with equal precision. It is seen from the table that approximately the same calculation time is required for a new scheme with 2500 cells and for a FVM scheme with 140,000 cells, which casts some doubt on the benefit of applying a scheme with high precision order in this computational experiment.

The current DGM scheme realization is far from optimal and there are still potential opportunities for reducing the computational time. One of the key moments is the usage of optimized quadrature rules for the calculation of volume and surface integrals. It is a subject for further investigation related to the optimization of new approximation scheme applications.

The calculation of 3D turbulent transonic flow over the LANN wing (Ref. [21]) is fulfilled using a second-order scheme DGM $K = 1$. The results are compared with the

TABLE 4: Evaluation of CPU time for different schemes.

| Method	Number of cells	Number of degrees of freedom $\Re$	Time for 50 MG iterations, sec	CPU time for a degree of freedom	Time ratio
DGM K = 36-level	2502	50,040	1185	4.74×10^{-4}	3.00
DGM K = 25-level	6393	63,930	826	2.58×10^{-4}	1.63
DGM K = 14-level	14,265	57,060	439	1.54×10^{-4}	0.99
FVM 3-level	62,689	62,689	496	1.58×10^{-4}	1.00
FVM 3-level	139,902	139,902	1115	1.59×10^{-4}	

Calculation of 3D turbulent flow over LANN wing (M = 0.82, $\mathrm{Re} = 7.3 \times 10^6$, $\alpha = 0.6°$).

experiment and with the calculation fulfilled on a denser grid through the conventional FVM scheme (Ref. [22]).

All the calculations are executed on unstructured hexahedral grids generated by code HEXPRESS of the NUMECA Int. Company. For the DGM scheme the grid with 190,213 cells is used. The results through FVM are obtained on a denser grid containing 625,076 cells, enabling application of an equivalent number of variables. In both cases the first layer of nodes is located at a distance $y+ \approx 1$ from the body. Figure 12 demonstrates the fragments of a coarse grid used for the analysis of a new scheme. All the calculations are executed at M = 0.82, $\alpha = 0.6°$, and $\mathrm{Re} = 7.3 \times 10^6$, which corresponds to experimental conditions. The S-A (Spalart, Allmaras) turbulence model is applied.

The comparison of pressure distribution in the airfoil $z = 0.475$ for two discretization
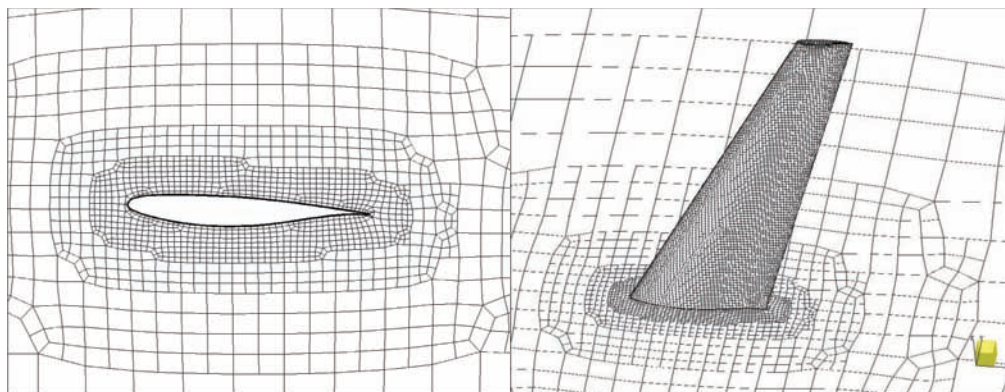
FIG. 12: Fragments of unstructured hexahedral grid around the LANN wing.
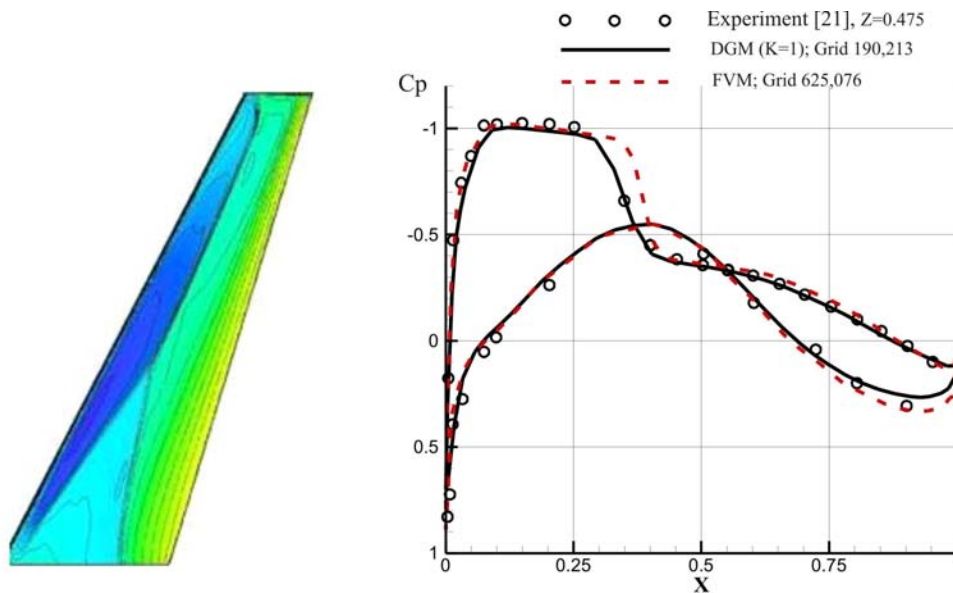
FIG. 13: Pressure distribution in the section of LANN wing at transonic turbulent flow: (− − −) FVM on a grid with 625,076 cells and (——) DGM on a grid with 190,213 cells.

schemes is shown in Fig. 13. It is seen that in spite of the use of a denser computational grid, the results obtained through the DGM scheme provide a better shock-wave position.

5.3. The Propagation of a Spherical Acoustic Wave

The solution of aeroacoustic problems requires the application of high-order computational schemes possessing minimal dispersive and diffused properties. The investigated scheme possesses such properties and is considered for the further industrial realization. Particularly, the scheme properties are investigated, while solving the classic problem on the acoustic momentum propagation, having comparatively small initial perturbation.

The numerical problem is considered within the cube computational area $[0 < x < 1]$; $[0 < y < 1]$; $[0 < z < 1]$. The following initial conditions exist at $t = 0$:

$$u\left(x,\ y,\ z,\ 0\right) = 0, \quad v\left(x,\ y,\ z,\ 0\right) = 0, \quad w\left(x,\ y,\ z,\ 0\right) = 0,$$

$$p = p_\infty \left(1 + \varepsilon\ 2^{-\frac{R^2}{r_0^2}}\right), \quad \rho = \rho_\infty \left(1 + \frac{\varepsilon}{c^2}\ 2^{-\frac{R^2}{r_0^2}}\right), \quad r_0 = 0.02, \quad \varepsilon = 0.001,$$

where $R^2 = \left(x - 0.5\right)^2 + \left(y - 0.5\right)^2 + \left(z - 0.5\right)^2$.

In this case, the solution of a linearized problem is described by the following equa-

tion:

$$p_{\text{exact}} = p_\infty \left(1 + \varepsilon \left[\frac{1}{2} \left(2^{-\frac{(r-ct)^2}{r_0^2}} + 2^{-\frac{(r+ct)^2}{r_0^2}} \right) - \frac{ct}{2r} \left(2^{-\frac{(r-ct)^2}{r_0^2}} + 2^{-\frac{(r+ct)^2}{r_0^2}} \right) \right] \right),$$

where c is a sound velocity. The solution of grid equations is obtained by the Runge–Kutta method of fifth order with an overall time step. Presented results correspond to the time $0.4/c$, i.e., to the moment when the leading Mach front does not yet achieve the boundary of computational area.

Shown in Fig. 14a is the comparison of the results for DGM $K = 1$, 2, 3 schemes and for the conventional FVM scheme [22]. The exact solution of this problem is also presented here. Shown in Fig. 14a is the case when the investigated schemes are used on individual grids chosen to equalize the number of degrees of freedom. It is seen that the schemes with higher precision order provide better matching with the exact solution. However, these schemes consume more CPU. Therefore the comparison of required CPU is fulfilled for the case when equal accuracy of calculations is ensured. Shown in Fig. 14b are the results for DGM $K = 2$ and 3, obtained on individual grids. It is seen that the accuracy of both results is the same. The comparison of CPU for this case is shown in Table 5. The fourth-order scheme provides good results 5.6 times quicker and consumes 1.4 times less memory. It is impossible to obtain such accuracy of results using the DGM $K = 1$ scheme and even more so using the conventional FVM scheme due to excessively
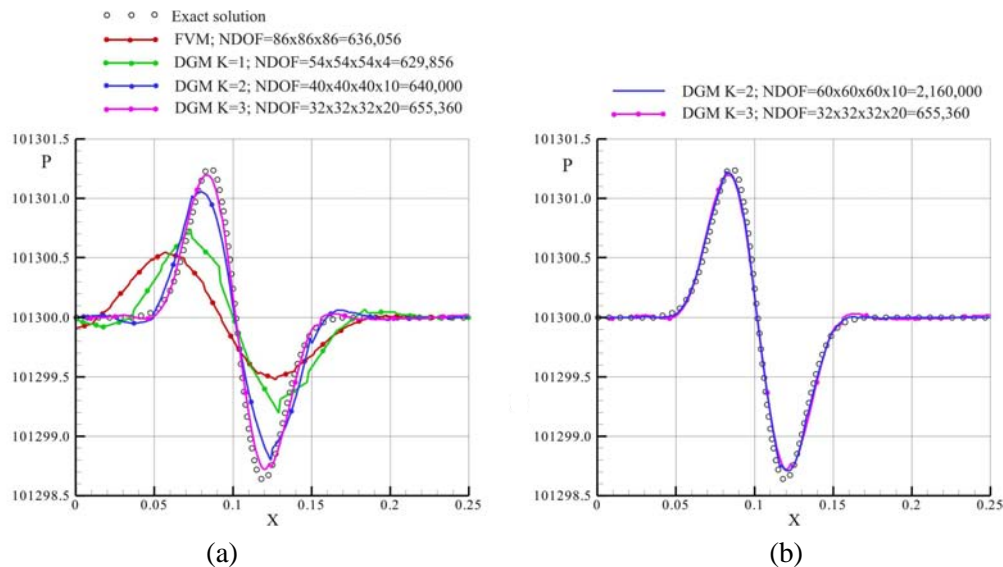
FIG. 14: Comparison of the exact solution with the numerical one for the acoustic momentum: (a) equivalent number of degrees of freedom and (b) equivalent accuracy of solutions.

TABLE 5: Comparison of CPU in the case of equal accuracy of results of the calculations for DGM (K = 2 and 3) schemes.

Scheme	Grid	Number of degrees of freedom	Operated memory, Kb	Memory ratio	Time of CPU	Time ratio
DGM $K = 2$	$60 \times 60 \times 60$	2,160,000	743	1.4	13 h 48 min	5.6
DGM $K = 3$	$32 \times 32 \times 32$	655,360	528	1.0	2 h 28 min	1.0

high CPU requirements

6. CONCLUSIONS

The discontinuous Galerkin method (DGM) was applied to the solution of Euler and Navier–Stokes equations on the basis of unstructured hexahedral grids. Considered test cases demonstrated good matching with theoretical or experimental results while using the fourth-order scheme, even on extremely coarse grids.

Comparisons were made of CPU required for a new scheme and for a scheme using the finite volume method (FVM) of second order of precision. In the case of application of an equivalent number of degrees of freedom in a discrete problem, the higher order scheme required more CPU.

The investigations showed that given equal accuracy of results, the calculation times of DGM and FVM schemes could be similar for some problems. Therefore, the conclusion about the necessity of applying higher order schemes was still unclear. The advantages of higher order schemes were obvious only in the acoustic problem on spherical wave propagation.

However, practical realization of the investigated scheme has many possibilities for significant reduction of calculation time. It is the solution of these problems regarding optimal realization of the DGM that offers the challenge for its widespread application. Questions regarding optimal realization of the scheme and its robustness are subjects for further investigation.

ACKNOWLEDGMENT

REFERENCES

1. Wolkov, A. and Lyapunov, S., Investigation of the efficiency of application of high-order numerical schemes for the solution of Navier–Stokes and Reynolds equations on unstructured adaptive grids, *ZHVMiMF*, vol. 46, no. 10, 2006.

2. Wolkov, A. and Lyapunov, S., Application of a discontinuous finite-element Galerkin method to the solution of Reynolds equations on unstructured adaptive grids, *TsAGI Sci. Trans.*, vol. XXXVIII, no. 3-4, 2007.

3. Wolkov, A., Hirsch, Ch., and Leonard, B., Discontinuous Galerkin method on unstructured hexahedral grids for 3D Euler and Navier–Stokes equations, *18th AIAA Computational Fluid Dynamics Conference,* AIAA Paper 2007-4078, 2007.

4. Morrison, J. and Hemsch, M., Statistical analysis of CFD solutions, *The 3rd AIAA Drag Prediction Workshop, 3rd AIAA APA Drag Prediction Workshop*, 2006; http://aaac.larc.nasa.gov/tsab/cfdlarc/aiaa-dpw/Workshop3/presentations/index.html.

5. Ladeinde, F., Alabi, K., Safta, C., Cai, X., and Johnson, F., The first high-order CFD simulation of aircraft: Challenges and opportunities, *44th AIAA Aerospace Sciences Meeting and Exhibit*, AIAA Paper 2006-1526, 2006.

6. Bassi, F. and Rebay, S., High-order accurate discontinuous finite element solution of the 2D Euler equations, *J. Comput. Phys.*, vol. 138, 1997.

7. Cockburn, B., Karniadakis, G., and Shu, C.-W., *Discontinuous Galerkin Methods: Theory, Computation and Applications, Lecture Notes in Computational Science*, New York: Springer-Verlag, 1999.

8. Bassi, F., Crivellini, A., Rebay, S., and Savini, M., Discontinuous Galerkin solutions of the Reynolds-averaged Navier–Stokes and $k - \omega$ turbulence model equations, *Comput. Fluids*, vol. 34, no. 4–5, 2005.

9. Bassi, F., Crivellini, A., Di Pietro, D. A., and Rebay, S., A high-order discontinuous Galerkin solver for 3D aerodynamic turbulent flows, *Proc. of ECCOMAS CFD 2006 Conf.*, P. Wesseling, E. Oñate, and J. Périaux (Eds), Sept., 2006.

10. Nguyen, N. C., Persson, P-O., and Peraire, J., RANS solutions using high-order discontinuous Galerkin methods, AIAA Paper 2007-0914, 2007.

11. Luo, H., Baum, J. D., and Lohner, R., A fast, p-multigrid discontinuous Galerkin method for compressible flows at all speeds, *44th AIAA Aerospace Sciences Meeting and Exhibit*, 9–12 Jan 2006, Reno, NV, AIAA Paper 2006-110, 2006.

12. Wang, Z. J., High-order methods for the Euler and Navier–Stokes equations on unstructured grids, *Prog. Aerospace Sci.*, vol. 43, 2007.

13. Delanaye, M., Patel, A., Leonard, B., and Hirsch, Ch., Automatic unstructured hexahedral grid generation and flow solution, *Proc. of the ECCOMAS CFD-2001 Conf.*, Swansea, Wales, UK, Sept 2001, 2001.

14. Atkins, H. L. and Shu, C. W., Quadrature free implementation of discontinuous Galerkin method for hyperbolic equations, *AIAA J.,* vol. 36, no. 5, 1998.

15. Krivodonova, L. and Berger, M., High-order implementation of solid wall boundary conditions in curved geometries, *J. Comput. Phys.*, vol. 211, no. 2, 2006.

16. Helenbrook, B., Mavriplis, D. J., and Atkins, H. L., Analysis of p-multigrid for continuous and discontinuous finite element discretizations, *Proc. of the 16th AIAA Computational Fluid Dynamics Conf.*, AIAA, pp. 2003–3989, 2003.

17. Nastase, C. R. and Mavriplis, D. J., Discontinuous Galerkin methods using an HP-multigrid solver for inviscid compressible flows on three-dimensional unstructured meshes, *44th AIAA Aerospace Sciences Meeting and Exhibit*, 9–12 Jan 2006, Reno, NV; AIAA Paper 2006-107, 2006.

18. Luo, H., Baum, J. D., and Lohner, R., A p-multigrid discontinuous Galerkin method for the Euler equations on unstructured grids, *J. Comput. Phys.*, vol. 211, 2006.

19. Mavriplis, D. J. and Venkatakrishnan, V., Agglomeration multigrid for two-dimensional viscous flows, *Computers Fluids*, vol. 24, no. 5, 1995.

20. Enayet, M., Gibson, M., Taylor, A., and Yianneskis, M., Laser Doppler measurements of laminar and turbulent flow in a pipe bend, NASA Contract Report CR-3551, 1982.

21. Müller, U. R., Schulze, B., and Henke, H., Computation of transonic steady and unsteady flow about LANN wing, Validation of CFD codes and assessment of turbulence models, ECARP Report 58, Vieweg, 1996.

22. www.numeca.be

INVESTIGATION OF THE APPLICATION OF ELECTRICAL DISCHARGES FOR WAVE DRAG REDUCTION

V. V. Skvortsov

Central Aerohydrodynamic Institute (TsAGI) 1, Zhukovsky str., Zhukovsky, 140180, Moscow region, Russia; E-mail: vlaskvortsov@rambler.ru

The problem of the main mechanism of electrical discharge influence on the wave drag of bodies at initial values of drag coefficient c_x and static pressures that are of interest for aviation applications is investigated based on the experiments in classical wind tunnels with well-known and stable parameters of flows. It is shown that such a main mechanism is heat one for the types of discharges proposed for practical application. It is also shown that electrical discharges being generated in front of models can lead to unsteady supersonic flow. In turn, this stipulates essentially nonsteady flow over a body that can seem as a shock wave disappearance at insufficient time resolution of an optical method of registration.

KEY WORDS: *wave drag, electrical discharge, heat mechanism of drag reduction, ion-overheat instability, non-stationarity of flow over bodies, optical method of registration, time resolution*

1. INTRODUCTION

The problem of the application of electrical discharges for wave drag reduction of aircraft was extensively investigated and discussed at the end of the last century and at the beginning of this century by some scientific centers in Russia, the United States, and Great Britain [1–6]. Physical investigations implemented on the models with high initial values of drag coefficient c_x testified to the possibility for considerable energy-profitable wave drag reduction while using this method. The effects of the disappearing of shock waves at the generation of discharges in front of models at supersonic flows were demonstrated. These effects were referred to as the new unknown properties of plasma.

The principal position of specialists adhering to the classical point of view toward the role of discharges is if the weak volume forces created by electric fields acting in plasma outside the boundary layer in the absence of an external magnetic field are not considered, the main mechanism of discharge influence on wave drag will be heat one,

with the ensuing consequences about energy consumption. This mechanism manifests itself in the fact that the pressure redistribution occurs in the area between the shock wave and the body, while supplying heat energy in this area. As a result, the shock wave deforms and stands off the body; meanwhile, the slope of streamlines to the axis of the body decreases, the value of the pressure component acting lengthways on the body diminishing.

To solve the problem set by physical experiments, research in this direction was made at TsAGI. The necessary condition for implementation was the requirement for the test accomplishment in classical wind tunnels with well-known and stable parameters of flows. The drag coefficients of models and the static pressures was of interest for aviation applications. The problem of the disappearing of shock waves was also studied.

Among different concepts of electrical discharge influence on aerodynamic characteristics of bodies, the concept of heat influence predicts rather definitely that at the generation of discharges in front of the bodies, the values of wave drag reduction will diminish, and energy consumption will increase at the improvement of the aerodynamic shape of the body. Therefore, in the frame of this problem, it is important to compare the energy efficiency of the present method for models with various aerodynamic shapes and to compare the values of drag coefficient that can be obtained at the generation of discharges near these models with the values of drag coefficients of models of optimal aerodynamic shape for corresponding Mach numbers without discharges near them.

The investigations of interest are accomplished in two types of experiments. In the first one, the discharges are created directly on models using plasma generators developed and manufactured by ideologists of the present method of wave drag reduction [1, 2]. The independent analysis of the results obtained was made at TsAGI. The conclusions made do not coincide in a number of counts with the conclusions of the present drag reduction method associates, particularly in efficiency. As a rule, there are no references to conclusions obtained at TsAGI in publications, especially in foreign ones.

In the second type of experiments, the models are installed in the wake of a longitudinal discharge with a low level of pulsations of current and of power supplied to this discharge. The results obtained by the author during the second type of experiments concerning the influence of power supplied to the discharge on the value of the variation of drag forces and on the efficiency of energy have not been published for a wide readership before.

The experiments of the first type were fulfilled in the TsAGI wind tunnel T-113 at Mach numbers equal to 4 and 2. The power supplied to the discharges are within the range from a few hundred watts up to $\sim$6.5 kW. This wind tunnel is known to have the dimensions of the test section equal to 600×600 mm; the length of test section is equal to 1.9 m. These dimensions are much larger than the characteristic dimensions of models used in the experiments. This fact ensures the absence of inverse effects of the energy supply near the models on the characteristics of the stream inside the primary area of the flow. The balance of the electromechanical type, insensitive to electromagnetic

disturbances of the discharge, was used for the measurements. The level of pulsations in a supersonic flow inside the test section of this wind tunnel was $< 1\%$.

The total number of runs fulfilled in wind tunnel T-113 equals approximately 110. The same regularity was revealed during all these runs, namely, a considerable decrease of energy efficiency was observed while passing from the models with high initial values of c_x to ones with low values, in accordance with the prediction of the heat concept of discharge influence on wave drag.

The variants of models involved in tests at $M = 4$ are shown in Fig. 1. Models A1 and A2 have a semispherical blunting of the nose part [7], models B1 and B2 have a cone blunting of the nose part and differ by structural features. Models A1 and B1 are made of caprolon (polyamide 6.6), and models A2 and B2 are made of radio ceramics. The cylindrical part of the models has a diameter equal to 40 mm. In addition, shown in Fig. 1, is the profile of model B3. Its nose part is close to the optimum shape for
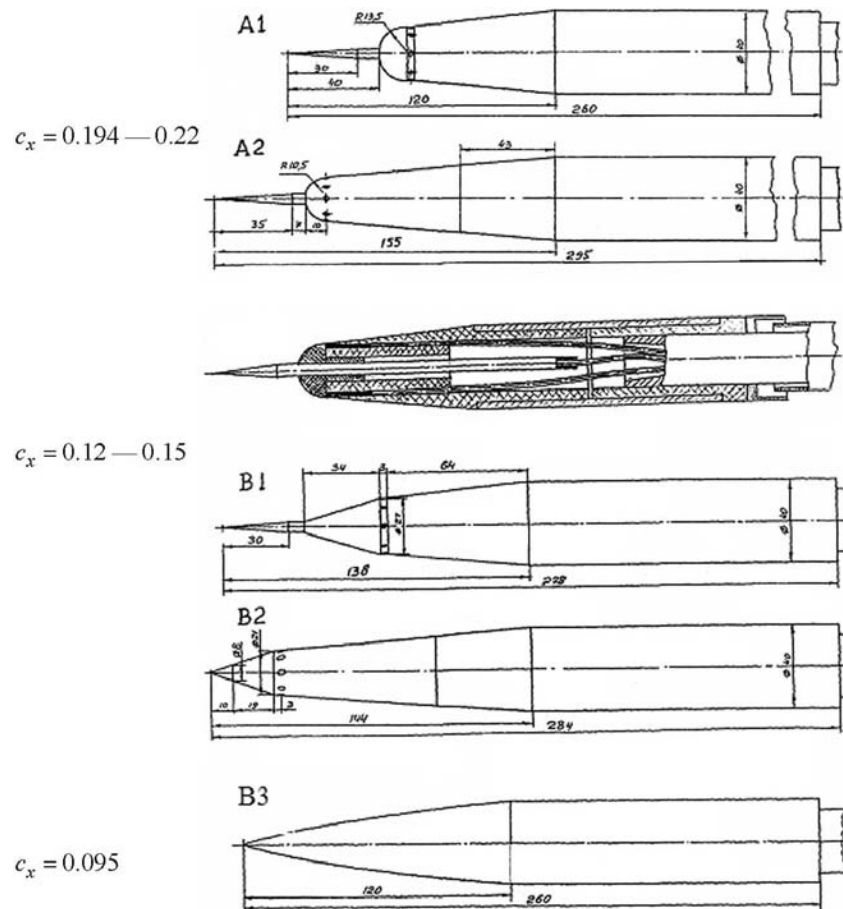
FIG. 1: Variants of models in experiments at M = 4.

M = 4 described by the equation [8, 9] $\bar{R} = \bar{x}^{3/4}$, where $\bar{R}$ and $\bar{x}$ are relative coordinates of the nose part. Models B1 and B2 (with cone blunting) and model B3 (with the optimum nose shape) had been proposed by TsAGI as having lower values of c_x. The models with the semispherical and cone blunting are equipped with plasma generators [10]. There is no plasma generator on the model with the optimum nose shape.

Plasma generators consist of eight electrodes of the same polarity mounted a flush on the lateral dielectric surface of the model, and of one electrode of another polarity representing a sharp metal cone, located in the model nose part. Plasma generators of the A models are energized both from the source of a quasi-constant current (capacitor bank) and from the source of an alternating current. The discharges for the B models are realized only by an alternating-current source. The electric potential between the electrodes turns out to be insufficient for the breakdown of the discharge gap while using the source of quasi-constant current. The circuit layout of the plasma generators under alternating current was established in such a way that the cone electrode has the same potential as the wind tunnel. One of the interesting results of tests led by Klimov [10] is that the discharges of the alternating current can burn at lower potentials than the discharges of the direct current. This is the reason for the lower energy consumption while using discharges under alternating current.

The velocity W of the incident flow at M = 4 is equal to 570 m/sec, and the static temperature T_{st} and the static pressure are equal to 69 K and 29 Torr, respectively. The unit Reynolds number is equal to 3.1×10^7 1/m.

The main results of the test analysis are shown in Figs. 2 and 3 and in Table 1. Particularly, shown in Fig. 2, is the dependence of the energy efficiency parameter on the
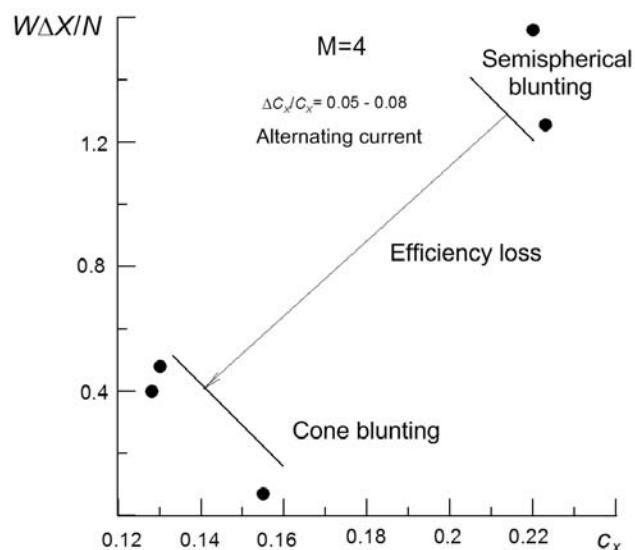
FIG. 2: Parameter of energy efficiency versus c_x coefficient in experiments at M = 4.
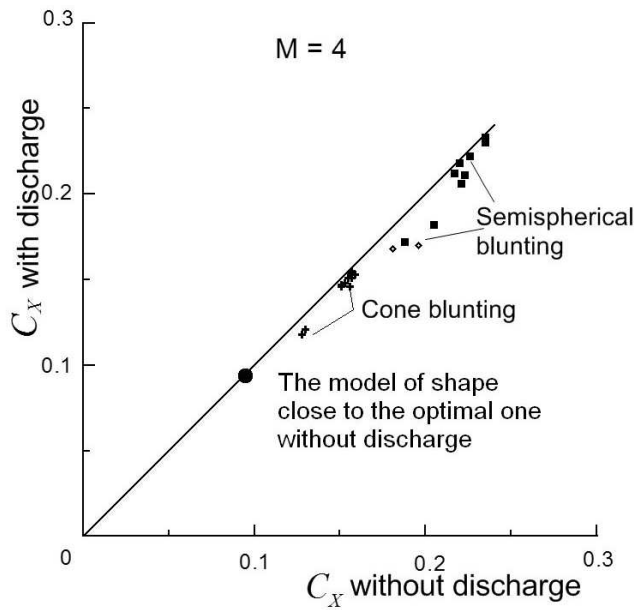
FIG. 3: Parameter of energy efficiency versus c_x coefficient in experiments at M = 4.

**TABLE 1:** Test analysis.

Nose part type	Discharge type	$c_{x\text{init}}$	Drag reduction value $\Delta c_x/c_x$ (%)	Ratio of the decrease of drag work in unit time to power consumed to generate the discharge $W\Delta X/N$
Semispherical blunting	Direct current	0.22	18	1.49
Semispherical blunting	Direct current	0.192	36	1.2
Semispherical blunting	Direct current	0.196	13.3	0.38
Semispherical blunting	Alternating current	0.22	6.8	1.56
Semispherical blunting	Alternating current	0.194	11.3	1.86
Cone blunting	Alternating current	0.15	2.6	0.1
Cone blunting	Alternating current	0.155	3.2	0.1
Cone blunting	Alternating current	0.122	6.1	0.48
Cone blunting	Alternating current	0.128	7.8	0.4
Optimal shape of the nose part without discharge	—	0.095	—	—

initial values of the coefficient c_x of the models for the case when plasma generators are energized from the source of alternating current. The efficiency parameter is determined as the ratio of drag work decrease in unit time ΔXW at the discharge generation to the power N supplied to the discharge. For the correct comparison, the data were presented for a short range of ratio $\Delta c_x/c_x = 0.05 - 0.08$, which is similar for different models and close to the maximum values obtained for the models with the nose part cone blunting.

It is seen from these data that a sharp decrease of the efficiency parameter occurs while passing from the models with semispherical blunting having sufficiently high initial values of coefficient c_x to the models with cone blunting possessing lower values of c_x, in compliance with the heat concept of discharge influence on wave drag. Meanwhile, the model with the optimum nose part shape without plasma generator has a lower value of coefficient c_x than the models equipped with operating plasma generators. This fact is seen from the data shown in Table 1 and in Fig. 3, where the value of the drag coefficient at the discharge generation is plotted as a function of the drag coefficient for the same models without discharge.

Similar results were obtained in the experiments at Mach numbers equal to 1.78 – 2 ($T_{st} \approx 160$ K, $W \approx 500$ m/sec). The comparison of the results for models having the values of coefficient c_x within the range 0.14–0.2 with the experimental data for the shortened model of the F-15 airctraft nose part having $c_x = 0.35 - 0.37$ (Fig. 4) was made. The former models are equipped with the combination of multielectrode plasma generator of current and erosion generator of plasma [11]. Their initial values of c_x are different due to either the design features of the installation of generators in a model or the progressive surface failure subjected by discharges, or else due to specially made ledges. The second model is equipped with plasma generators of a different type [11]. Shown in Fig. 4b as an example is a variant of models with the generator similar to the
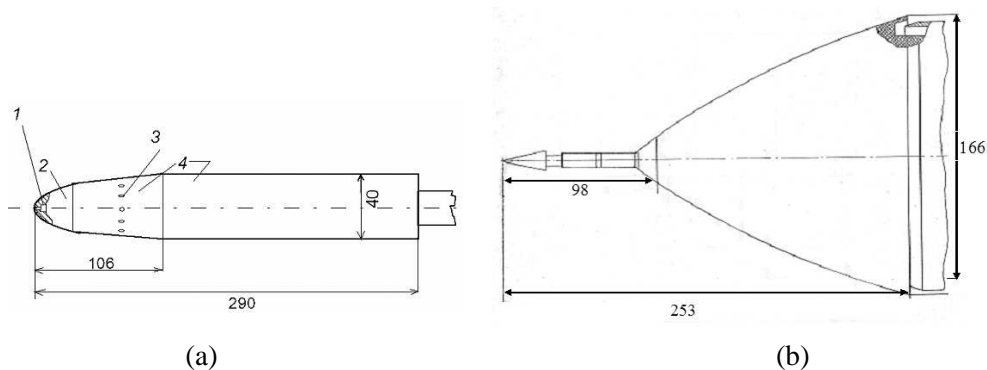

FIG. 4: Variants of models in experiments at M≈2: (a) scheme of models with application of the combination of erosive generator and direct current generator (1, erosive generator; 2, metal surface; 3, anodes of direct current generator; 4, dielectric surface); (b) shortened model of the aircraft F-15 nose part.

another one applied in the tests at Mach number M = 4 (the length of the knot of central electrode equals 98 mm).

The experiments were implemented at static pressures within the range from 100 Torr up to 300 Torr (from $1.33 \cdot 10^4$ Pa up to $4 \cdot 10^4$ Pa). The dependence of the efficiency parameter on the drag coefficient c_x for the range of $\Delta c_x / c_x$ values from 0.045 up to 0.06 (these values correspond to their limiting values obtained for the models presented in Fig. 4a) is shown in Fig. 5. The importance of the choice of a sufficiently narrow range of values of this ratio, similar for different models, becomes notably evident in this case, since the high values of the efficiency parameter can be obtained for the model with a bad aerodynamic shape [12]. The maximum value of ratio $\Delta c_x / c_x$ for the last model equals ~0.05. As seen from Fig. 5, the efficiency parameter decreases significantly while passing from the model with a high initial value of the drag coefficient to the models with lower values; the same results from the heat influence concept. Meanwhile, in the majority of cases, the TsAGI model with an optimal aerodynamic shape of the nose part, whose contour is described by the relationship $\bar{R} = \bar{x}^{2/3}$, has the minimal value of c_x, without additional energy consumption as compared to other models, equipped with operating plasma generators (Fig. 6).

Similar results were obtained at the installation of models in a wake of longitudinal discharge with a low level of pulsations of current and of power supplied to the discharge generated in supersonic airflow [13]. The discharge generation scheme is shown in a Toepler picture (Fig. 7), where the dashed line designates the contour of the electrodes. The discharge is generated between a brass anode 1 installed in profiled support 2 with the tip directed along the flow and duraluminum profiled support 3 (cathode) with two
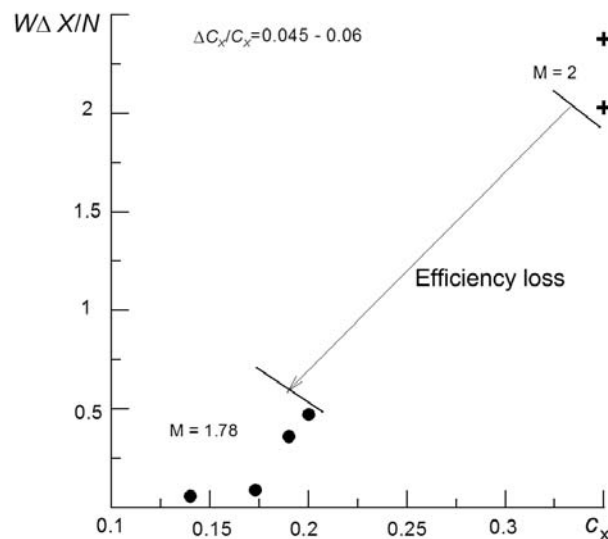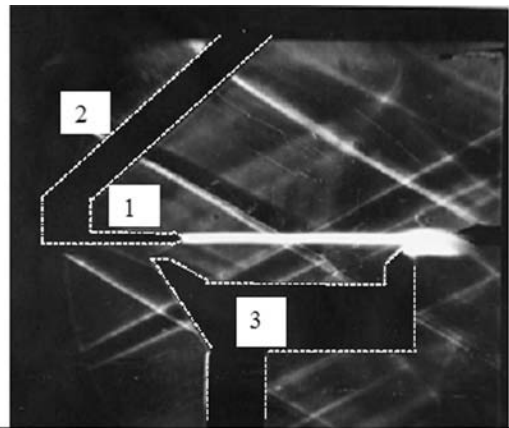

FIG. 5: Energy efficiency parameter versus c_x coefficient in experiments at M $\approx$ 2.
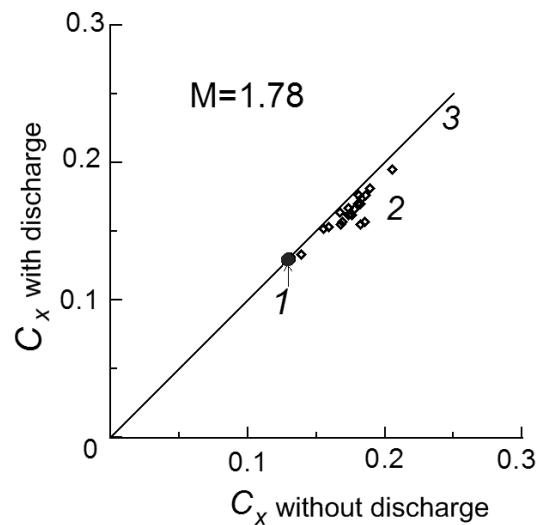
FIG. 6: Value of c_x coefficient at the generation of discharges versus c_x without discharge in experiments at $M \approx 2$: 1, model having a shape close to the optimal one; 2, experiment data; 3, line of equal values of drag coefficients with discharge and without it.

FIG. 7: Toepler photography illustrating the scheme of discharge generation with low level of pulsations of current and of power supplied to the discharge.

ledges. The ledge that is closer to the upper electrode is meant for a reliable breakdown of the discharge gap. After firing, the discharge is brought downstream along the plate, undergoes contraction at a certain length of the discharge gap, and closes up primarily on the ledge located far from the anode. The discharge current is equal to 1 A; the discharge burning voltage is equal to 1 kV. Such a discharge has a much smaller value of current pulsations as compared to the discharges in which the discharge channel crosses

a supersonic stream at the current closing up from one electrode to another one and in which the current pulsations can amount to 40–50% from the average value.

The tests were implemented in the supersonic wind tunnel T-42M with flow size equal to $120\times120\times400$ mm, developed by rectangular nozzle and walls of the facility adjoint with it. The level of velocity pulsations equal to $\sim$0.6%. The low static pressure was generated by means of a supersonic ejector. Unit Reynolds number Re varyied from $\sim 0.9\times10^7$ up to $\sim 2.1\times10^7$ 1/m. The electrodes did not have galvanic contact with the facility walls.

The tests have shown that the conditions of the most stable burning of discharge with a low level of pulsations of current ($\sim$3%) and of power ($\sim$5%) are achieved when the distance across the flow between the points of discharge connection to the electrodes does not exceed 1.5–2 mm, which seems to be the characteristic radius of the discharge channel, and the discharge closes on the leading edge of the back ledge of the cathode. At discharge shift outside the cathode, the pulsations of current increase up to 5%, and the pulsations of power increase up to 7.5%.

The qualitative investigations of the reduction temperature distribution in a wake behind the discharge in the area without discharge where the models are installed have shown that the area heated by the discharge in the plane perpendicular to the flow is of elliptical shape, the major axis of ellipse being perpendicular to the cathode plane, which is related to the character of the flow over the cathode ledge. As a result of investigations of total pressure distribution in a wake behind the discharge, it was determined that the flow was supersonic, with the value of Mach number in the center of distribution equal to $\sim$1.3–1.6.

The investigations implemented have demonstrated an important feature of electrical discharge in gas flow, namely, the discharge is able to amplify the density pulsations of neutral flow, which appear inevitably; for example there pulsations can arise due to the flow separation or due to the development of the flow vortex structure—even with profiled electrodes. Taking into account that the flow is isobaric, this means there are zones with a different gas temperature in the discharge area.

Some results of investigations of the influence of supersonic flow heating by longitudinal discharge on the drag of models of different geometry, but of similar midsection, that are installed in a wake of discharge, as well as the evaluation of the energy efficiency, are shown in Fig. 8. The results obtained conform well to the prediction of the heat concept of discharge influence on aerodynamic effects. Notably, the effect of the influence of the energy supply decreases while c_x of models is diminishing from the values about 1 (semispherical blunting, cone with aperture angle equal to $2\alpha = 80$ deg) up to the value of $\sim$0.3 (cone with aperture angle $2\alpha = 40$ deg). The efficiency of the energy supply decreases even more sharply. For the models with a high value of c_x, the value $\Delta XW/N$ increases as the ratio D/d_{ch} magnifies, where D is the model diameter, d_{ch} is the channel diameter. It is similar to the calculations [14, 15] fulfilled on the basis of the gas dynamics equations with energy supply, i.e., the heat concept.
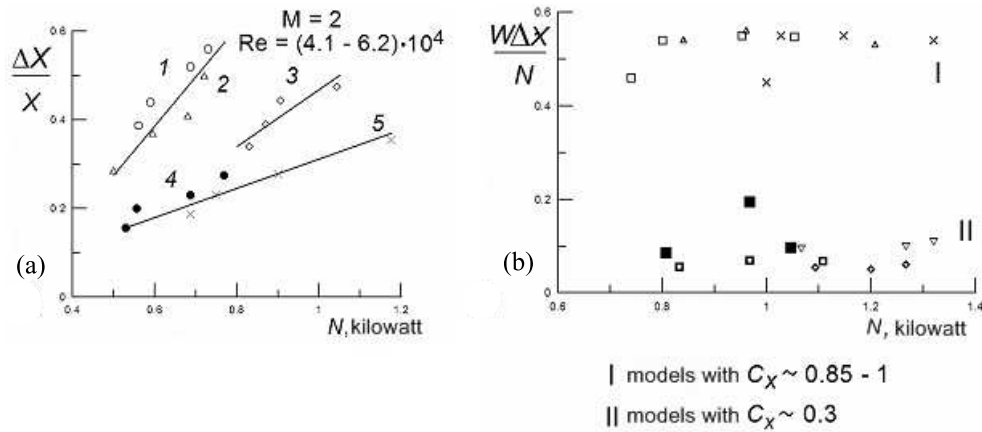
FIG. 8: The variation of drag force (a) and energy efficiency (b) at the installation of models in a wake behind the longitudinal discharge versus the power supplied to the discharge: 1, semisphere; 2, cone; 3, semisphere; 4, cone at $p_{st} = 58$ Torr; 5, cone at $p_{st} = 85$ Torr.

At the same time, a series of effects of the discharge influence on the wave drag can be noted that are likely to refer to the nonthermal effects. Namely, in the case of the discharge creation on the models these effects are the dependence of the drag reduction effect on the polarity of the electrodes, and the decrease of energy consumption at the feed of discharges by alternating current and at their pulse-periodic feed. Several authors relate the features that take place at the simultaneous application of electrical discharge and electron beam to the nonthermal effects [16,17]. The same is true for the possibility of initiating a strong electric field at shock waves that can influence the gas dynamics of the flow [18, 19].

In the tests fulfilled of the first and second types, there was no special investigation of Mach number influence on the amount of wave drag reduction for the models of similar geometry with the same energy supply to the discharges. For example, the geometry of models for the tests in wind tunnel T-113 at different Mach numbers was selected to be close to the geometry of models with an optimum shape of nose part and to be acceptable with technological possibilities of plasma generators arrangement. These geometries differ substantially for different values of Mach number. The experimental data on Mach number influence on energy efficiency of the method with application of generators with plasma jet blowing toward the airflow are contained in Ref. [11]. As follows from Ref. [11], at $M > 1.5$, there is a substantial decrease of the indicated value.

Investigated in the experiments with longitudinal discharge application was the time-resolution pattern of supersonic flow over models. This flow is exposed to the mentioned discharge. The flow pattern was registered by the IAB-451 instrument of a Toepler type with its time sweep done by a high-speed photochronograph operating at a time magnifier mode. In addition, the flow pattern photographing was fulfilled as a starting point

for our investigations by the same devices at an exposure time of $\sim$0.01 s. The tests of this type, but otherwise stated, were fulfilled at TsAGI previously by Kalachev and by Alferov.

The discharge was generated in the way shown in Fig. 7. The electrodes and the power supplied to the discharge were installed so that the minimum of pulsations was realized. The distance between the anode tip and the leading edge of the cathode ledge situated far from anode was equal to $\sim$70 mm. The Mach number of the cold flow was 2.5. The static pressure of the facility test section was 7.7×10^3 pascal (58 Torr). Used as the models were semispheres of 15 mm diameter and a cone having a semiapex angle equal to 20 deg and a base diameter equal to 6 mm. In all the tests, the models were installed on the axis of the facility test section at a distance equal to 20 mm from the cathode rear face.

During the implementation of the time-sweep tests, the lighter of the Toepler device worked in a pulse regime and was activated from the desk of the high-speed photochronograph camera simultaneously with the start of the image sweep on the photographic film. The high-speed photochronograph camera operated with a two-row insert; only one row of the lens was used.

Toepler photos of the cold flow over the model obtained by means of the high-speed photochronograph reveal classical shock waves at all exposure times. On the photos of the flow over the same models with a heat supply inside the flow by means of longitudinal discharge (the discharge current equals 1 A, the discharge voltage equals 1 kilovolt) and with longer exposure time ($\Delta t \approx 0.01\,\mathrm{s}$), the flow pattern in the central zone (where the flow is heated) turns out to be blurred, like in some other works. But the unsteady flow pattern was registered clearly (Fig. 9) while decreasing the exposure time up to $\sim$1.5 microsec at a time interval between the starts of the adjacent frames equal to $\sim$3 microsec. The period of pulsations of this pattern was close to the period of pulsations of the flow density gradient, measured during the tests using the combination of Toepler device and photoelectric multiplier with a rather wide-range frequency characteristic. Besides this, for the flow heated, the shock wave in the central part moved forward, which corresponds to a decrease of the Mach number. This behavior of the flow was observed only in the central (i.e., heated) flow part, which was varying with time under the influence of the discharge. Given the constant pressure, this indicates a heterogeneity of temperature, density, sound speed, and Mach number along the flow. This gives arise of spatial zones with high temperature, which alternate with zones of lower temperature, and to the corresponding moving alternating density gradients. This leads to an unsteady flow pattern. When such flow inflows on the model, the area in front of the body looks like a zone of the shock wave "disappearance" if the method of optical imaging has a large averaging time. The gas-dynamic analysis of the periodic inflow of zones with different values of temperature and of density on the shock wave, accomplished by Kuznetsov (TsAGI), conforms satisfactorily to the experimentally observed picture of the phenomenon. A possible cause of the unsteady flow is the mechanism of
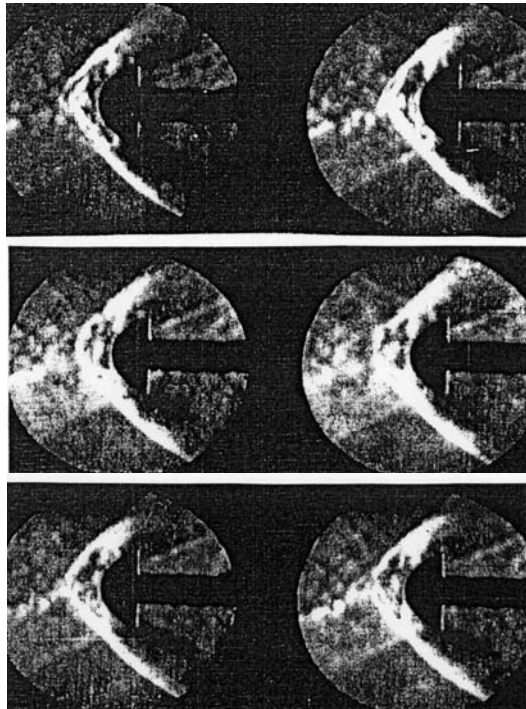
FIG. 9: High-speed sweep of flow pattern over model installed in a wake of longitudinal discharge, illustrating unsteady behavior of flow.

heterogeneous heating of the flow, typical for discharges. The ionization-overheating instability can be such a mechanism [20]. Therefore, the tests done and their analysis have shown that the cause of this effect consists not in the disappearance of shock waves in front of the body under the influence of electrical discharge on incident flow, but in the appearance of substantially unsteady flow over the body.

2. CONCLUSIONS

The tests fulfilled proved the heat concept of electrical discharge influence on the wave drag of bodies to be essential and basic one at the values of drag coefficients c_x and static pressures that were of interest for aviation applications. During the tests with TsAGI models that had the optimum shape of the nose part and that were not equipped with plasma generators, the lowest values of the wave drag coefficient were obtained in most cases as compared to the models that were equipped with operating plasma generators. It was shown that the cause of the disappearance of shock waves influenced by electrical discharges on supersonic flow demonstrated in a series of investigations could be the appearance of substantially unsteady flow over models caused by the development of alternating zones with different densities and temperatures of gas in the incident flow.

It should also be noted that the conversion of the energy of the electrical field that maintains the discharge in the airflows into the heat energy passes through a series of stages. Therefore, it significantly decreases the efficiency of the process. At the values of the ratio of electric field intensity to the concentration of neutral molecules that are typical for discharges in air, up to 50–80% of this energy goes first of all into the excitation of the vibrational degrees of freedom of the nitrogen molecules [20]. Then, this energy relaxes gradually into translational degrees of freedom. The rest of the energy goes into the excitation of the vibrational degrees of freedom of the oxygen molecules, the lowest proportion of the energy going into the excitation of the rotational and translational degrees of freedom (i.e., directly of thermal ones). The speed of the relaxation processes depends on the gas temperature in the discharge, and it can be low at the initial stage of heating (especially for nitrogen) [21]. Shown experimentally in Ref. [22] is the fact that the ratio of the energy going into the heating to the total discharge energy in the nitrogen can be on a level of 10%. This ratio is taken to be equal to 20% in many numerical calculations as the result of the averaging of different experimental data. These values show that the essential energy release occurs downstream, but not in front, of the body.

ACKNOWLEDGMENT

REFERENCES

1. Magneto plasma aerodynamics in aerospace applications, *Proceedings of International Workshop*, Vols. 1–5, IVTAN (Institute of High Temperatures RAS), Moscow, 1999–2003.
2. USAF, Weakly ionized gases workshops, No 1–6, USAF Academy, 1996–2004.
3. Cain, T. and Boyd, D., Electrodynamics and the effect of an electric discharge on cone/cylinder drag at Mach 5, AIAA Paper No. 99-0602, 1999.
4. Fomin, V., Tretyakov, P., and Taran, J. D., Flow control using various plasma and aerodynamic approach (short review), *Aerospace Sci. Technol.*, vol. 8, pp. 411–421, 2004.
5. Macheret, S. O., Shneider, M. N., and Miles, R. B., Magnetohydrodynamic and electrohydrodynamic control of hypersonic flows of weakly ionized plasmas, *AIAA J.*, vol. 12, no. 11, pp. 1378–1387, 2004.
6. Bletzinger, P., Ganguly, B. N., and Van Wie, D., Plasmas in high speed aerodynamics, *J. Phys. D.*, vol. 38, no. 4, pp. R33–R57, 2005.
7. Klimov, A. and Bityurin, V., Charged plasma formations in high-speed airflow, *Proceedings of 7th International workshop on Magneto-Plasma-Aerodynamics*, IVTAN, Moscow, pp. 67–78, 2007.
8. Grodzovsky, G. L. (Ed.), *Aeromechanics of Supersonic Flow over Bodies of Revolution with*

Optimum Aerodynamical Shape, Mashinostroenie, Moscow, 1975.

9.   Mile, A. (Ed.), *Theory of Optimum Aerodynamic Shapes*, Mir, Moscow, 1969.

10.   Gridin, A. Yu., Efimov, B. G., Zabrodin, A. V., Klimov, A. I., Kuzin, K. A., Kuznetsov, Yu. E., Lutskii, A. E., Severin, A. V., Skvortsov, V. V., Sukovatkin, N. N., Khodataev K. V., and Cherkashin, V. A., Computational and experimental investigations of flow over body with needle at the presence of discharge in its nose part, Preprint of IPM named after M. V. Keldysh (Keldysh Institute of Applied Mathematics), No. 19, 1995.

11.   Leonov, S., Nebolsin, V., and Shilov, V., Effectiveness of plasma jet effect on bodies in an airflow, *Proceedings of Workshop "Perspectives of MHD and Plasma Technologies in Aerospace Applications*,*" IVTAN, Moscow, pp. 58–65, 1999.

12.   Beaulieu, W., Bityurin, V., Klimov, A., Kuznetsov, A., and Leonov, S., Plasma aerodynamic WT test with 1/6 scale model of nose part of flight test laboratory (F15), *Proceedings of Workshop "Perspectives of MHD and Plasma Technologies in Aerospace Applications*,*" IVTAN, Moscow, pp. 44–46, 1999.

13.   Ivanov, V. V., Skvortsov, V. V., Kuznetsov, Yu. E., Efimov, B. G., Pyndyk, A. M., Kireev, A. Yu., Krasheninnikov, V. N., and Shilenkov, S. V., Spectroscopic investigations of longitudinal discharge in supersonic airflow at injection of propane in discharge area, *High Temp.*, vol. 46, no. 1, pp. 7–14, 2008.

14.   Georgievsky, P. Yu. and Levin, V. A., Effective control of flow over various bodies with the supply of energy into oncoming stream, *Proceedings of 4th Workshop on Magneto Plasma Aerodynamics in Aerospace Applications*, Reports' thesis, IVTAN, Moscow, 2002.

15.   Georgievsky, P. Yu., Control of forward separation zones using local energy supply into oncoming flow, IX All-Russian Congress on theoretical and applied mechanics, collection of abstracts, Vol. II, Nizhny Novgorod, 2006.

16.   Klimov, A., Bituirin, V., and Serov, Yu., Non-thermal approach in plasma aerodynamics, AIAA Paper No. 2001-0348, 2001.

17.   Bituirin, V., Bocharov, A., Klimov, A., and Leonov, S., Analysis of non-thermal plasma aerodynamic effects, AIAA Paper No. 2006-1209, 2006.

18.   Alferov, V. I., Investigation of structure of the high-power discharge in high-velocity airflow, *MZhG (Fluid Mech.)*, vol. 6, pp. 163–175, 2004.

19.   Kolesnikov, A. F., Mechanism of ions thermal-baro diffusion pump in weakly ionized shock layer, AIAA Paper No. 2001-2871, 2001.

20.   Raizer, Yu. P., *Physics of Gas Discharge*, Nauka, Moscow, 1971.

21.   Agafonov, V. P., Vertushkin, V. K., Gladkov, A. A., and Polyansky, O. Yu., *Nonequilibrium Physical-Chemical Processes in Aerodynamics*, Mashinostroenie, Moscow, 1972.

22.   Bushmin, A. S. and Dmitriev, L. M., Investigation of distribution of energy losses of electrons at electrical discharge excitation of gases and their mixtures: Facilities for the investigations of aerodynamics and aircraft strength, *TsAGI Proceedings*, vol. 1949, pp. 86–91, 1978.

INVESTIGATION OF THE SONIC BOOM OF THE OBLIQUE WING AIRCRAFT

Kyuchul Cho

Central Aerohydrodynamic Institute (TsAGI) 1, Zhukovsky str., Zhukovsky, 140180, Moscow region, Russia; E-mail: teperin@mail.ru

The characteristics of the lift-drag ratios and sonic boom intensity of the aircraft, consisting of the oblique wing, fuselage, and vertical fin, were investigated at $M_\infty \sim 1.2 - 1.98$. The investigation results were compared to the results, obtained for the Tu-144 aircraft, having the same fuselage and fin. The Tu-144 aircraft has the same wing area as the aircraft with the oblique wing.

KEY WORDS: *oblique wing, aerodynamic characteristics, sonic boom*

1. INTRODUCTION

It is known that at transonic and small supersonic flow velocity, the aerodynamic characteristics of aircraft with the oblique wing have special advantages in comparison with aircraft with the symmetrical wing. Given in Ref. [1] is the wing drag equation, taking into account friction, induced, and wave drag separately,

$$X = c_f q S_w + \frac{Y^2}{\pi q l} + \frac{M_\infty^2 - 1}{2\pi q} \frac{Y^2}{x_1^2} + \frac{128q}{\pi} \frac{V^2}{x_2^4} \tag{1}$$

where c_f is the friction coefficient, q is the dynamic pressure, S_w is the wetted wing area, Y is the lift, l is the wingspan, M_∞ is the free-stream Mach number, V is the volume, and x_1 and x_2 are specified by the equations

$$\frac{1}{x_1^2} = \frac{1}{\pi} \int_0^{2\pi} \frac{\sin^2 \theta}{x(\theta)^2} d\theta \tag{2}$$

$$\frac{1}{x_2^4} = \frac{1}{2\pi} \int_0^{2\pi} \frac{d\theta}{x(\theta)^4} \tag{3}$$

where θ is the inclination of the cutting Mach plane and $x(\theta)$ is the length of an equivalent axially symmetrical body.

The first term in Eq. (1) specifies the friction drag, the second term corresponds to the induced drag, the third term corresponds to the wave drag due to the lift, and the fourth term corresponds to the wave drag due to the wing volumes. At small supersonic Mach numbers. x_1 and x_2 are approximately equal to the length L_w for a symmetrical wing with a great sweep angle and to two lengths L_w for an oblique wing. It follows from Eq. (1) that the oblique wing wave drag due to the lift is four times less than the wave drag due to the lift of the symmetrical wing, and the oblique wing wave drag due to the volume is 16 times less than that one of the symmetrical wing under the condition of equal area and span. Shown in Fig. 1a is the dependence of the lift-drag ratio on the Mach number ($M_\infty \sim 0.6 - 1.4$) for the oblique and symmetrical wing [2]. One can see that the oblique wing with the ratio of the ellipse sides $b : a = 10 : 1$ and with variable sweep has better characteristics than the symmetrical wing within the whole range of Mach numbers.

The method, based on the solution of Navier-Stokes equations was used for the calculation of sonic boom intensity of aircraft with symmetrical and oblique wing [3]. This method requires the creation of a special computational grid near the aircraft surface to take into account properly the viscosity effects and to plot the velocity profile in the boundary layer. For this purpose, the value of the y^+ parameter, specified by the distance between the surface and the first grid node, is to be < 200, and at least 10 layers should

(a)   (b)
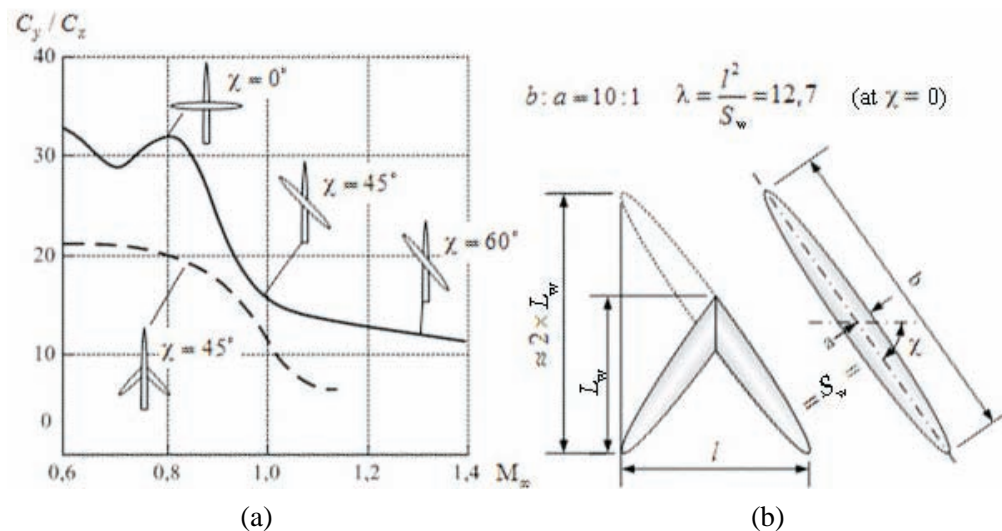
FIG. 1: Comparison of the lift-drag ratio of the elliptic oblique and symmetrical wing depending on Mach number: (a) lift-drag ratio as a function of Mach number [1]; (b) geometry of the symmetrical and oblique wing.

be across the boundary layer. In this paper, we used the model of a turbulent flow SST with the initial fractional intensity equal to 5% and eddy viscosity ratio equal to 10 in all cases while calculating the flow over an aircraft under the full-scale conditions for Reynolds numbers $Re > 3 \times 10^8$ [4].

2. COMPARISON OF AERODYNAMIC CHARACTERISTICS OF THE SYMMETRICAL AND OBLIQUE WINGS

The flow problem is solved for two oblique wings and one symmetrical wing. The wing surfaces are constructed by NACA64412 airfoil (Fig. 2a). Cited in Table 1 are the geometric parameters of the wings and of the computational grid. The area of all the wings equals 501 m^2, the maximum thickness ratio of the airfoils being equal to 12%. The
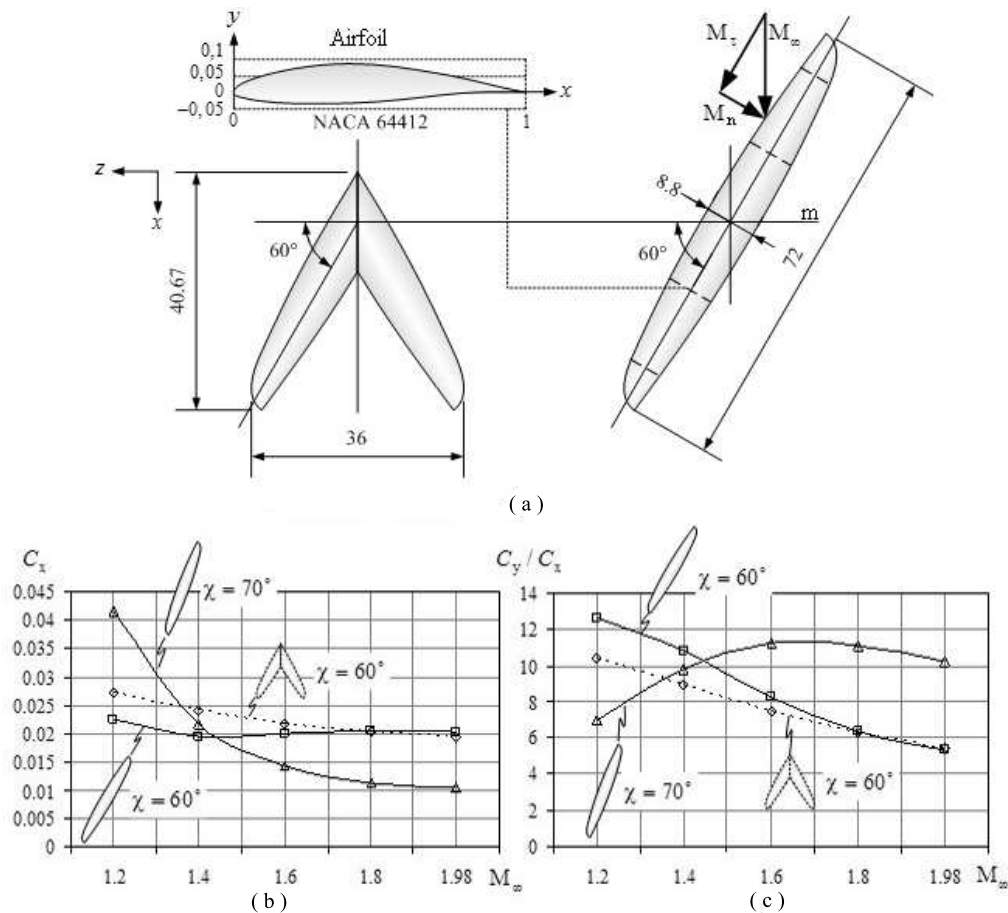
FIG. 2: Comparison of the lift-drag ratio of the oblique and symmetrical wing: (a) the schemes of the symmetrical and oblique wing; (b) the wing drag; (c) the lift-drag ratio.

TABLE 1: Wing types and parameters.

Wing type/- parameters		Symmetrical wing $\chi = 60$ deg		Oblique wing		
				$\chi = 60$ deg		$\chi = 70$ deg
Airfoil type		NACA 64412 (maximum thickness ratio 12%)				
Area S_w, m^2		501				
Length L_w, m		40.67		62.35		67.66
Span l, m		36		36		24.63
Aspect ratio λ		2.59		2.59		1.21
				10.35 (at $\chi = 0$)		
Mass, t		150				
c_y		M$_\infty =$	1.2	1.4	1.6	1.8	1.98
		$c_y =$	0.287	0.211	0.162	0.128	0.106
Grid	Form	Tetrahedral grid				
	Number of nodes	571,348 (symmetry)		1,152,486		1,156,159
	Number of elements	1,718,338 (symmetry)		3,461,882		3,498,721

oblique wing aspect ratio is equal to 10.35 at $\chi = 0$ (χ is a sweep angle), the symmetrical wing aspect ratio being equal to 2.59 and coinciding with the oblique wing aspect ratio at $\chi = 60$ deg. The lift coefficient is specified at various Mach numbers from the condition of flight at an altitude of 16100 m and the aircraft mass is 150 t. Cited in the bottom lines of Table 1 are the tetrahedral grid parameters. The computational area, aimed at the calculation of the flow over the symmetrical wing, has the symmetry plane and therefore one calculates the flow over a half wing. The oblique wing is considered completely.

Shown in Figs. 2b and 2c is the dependence of drag and lift-drag ratio on the Mach number. At $\chi > 60$ deg, the Mach number, being normal to the leading edge, is < 1 within the range of the free-stream Mach numbers M$_\infty \sim 1.2 - 1.98$, but at $\chi = 60$ deg and M$_\infty \geq 1.8$, the Mach cone is tangent to the oblique wing leading edge. At M$_\infty =$ 1.2 and 1.98, the symmetrical wing surface is streamlined without flow separation. The separation arises at M$_\infty =$ 1.4, 1.6, and 1.8 after a shock wave in the narrow zone on the surface. The separated flow appears on the surface of the oblique wing with the sweep angle $\chi = 60$ deg at M > 1.4 from under an intense shock wave; and as the Mach number increases, the separated flow area expands slightly. In order to provide lift at $\chi = 70$ deg and at the free-stream Mach numbers equal to 1.2 and 1.4, greater angles of attack— $\alpha = 9, 6.42$ deg, accordingly—are needed. For this reason, the separation arises on the wing leading edge, and the wall streamlines, arising from the leading edge in front of the separation area, pass through the arc trajectory over the wing surface to the leading edge behind the separation area and cause a new separation area to appear. Because of this fact, the drag of the oblique wing with $\chi = 70$ deg increases abruptly at M$_\infty = 1.2$.

The separated flow is not observed at $M_\infty > 1.6$ on the surface of the wing with $\chi = 70$ deg and only at $M_\infty = 1.98$ does the flow on the wing rear accelerate and separate after the shock wave in a narrow zone. At $M_\infty \sim 1.2 - 1.98$, the Mach cone is not tangent to the leading edge of the oblique wing with $\chi = 70$ deg, and Mach number normally to the edge is $M_n < 0.7$. Thus, the drag of the oblique wing with $\chi = 70$ deg decreases abruptly as the free-stream Mach number increases. At $M_\infty = 1.2$, the lift-drag ratio of the oblique wing with $\chi = 60$ deg is better than the lift-drag ratio of the other types of wing, and as the free-stream Mach number increases, the oblique wing with $\chi = 70$ deg has the lowest drag.

The oblique wing has a peculiarity, consisting in the fact that the lift is created mainly on the wing rear. This peculiarity results in the creation of a roll moment with respect to the x-axis.

3. COMPARISON OF THE SONIC BOOM INTENSITY OF AN AIRCRAFT WITH THE OBLIQUE WING AND OF THE TU-144 AIRCRAFT

For the analysis, we chose the conception of the entirely rotating wing, varying its sweep from $\chi = 0$ deg for subsonic flight up to $\chi = \geq 60$ deg for transonic and supersonic flight. For the investigation of the sonic boom intensity, we chose the oblique wings with sweep angles $\chi = 60$ deg for $M_\infty = 1.2$ and $\chi = 70$ deg for $M_\infty = 1.6$, 1.98, installed on the fuselage of the Tu-144 aircraft by means of a pylon (Fig. 3a). Cited in Table 2 are the parameters of the Tu-144 aircraft [5] and of the aircraft consisting of the oblique wing, fuselage, and vertical fins.

The oblique wing axis of rotation is situated at a distance of 34 m from the fuselage nose. The length of the aircraft with the oblique wing increases as the sweep angle increases, and for $\chi \geq 60$ deg, it is greater than the length of the Tu-144 aircraft. The wing aspect ratio of the Tu-144 aircraft is less than the wing aspect ratio of the aircraft with the oblique wing with $\chi = 60$ deg and greater than the aircraft with the oblique wing with $\chi = 70$ deg. Shown in the bottom lines of Table 2 is the tetrahedral grid size. In order to calculate the flow over the Tu-144 aircraft, one uses the unstructured grid, taking into account the model symmetry. The aircraft with the oblique wing is considered completely.

4. COMPARISON OF AERODYNAMIC CHARACTERISTICS

The flow over the aircraft with the oblique wing with $\chi = 60$ deg is calculated for the free-stream Mach number $M_\infty = 1.2$, and the flow over the aircraft with the oblique wing with $\chi = 70$ deg is calculated for $M_\infty = 1.6$ and 1.98. The calculation results are compared to the data obtained for the Tu-144 aircraft. At $M_\infty = 1.98$, a narrow separated flow arises at the oblique $\chi = 70$ deg wing tip after an intense shock wave. Shown in Fig. 3b is the pressure distribution on the oblique wing surface at $M_\infty = 1.2$. Pressure drops are more
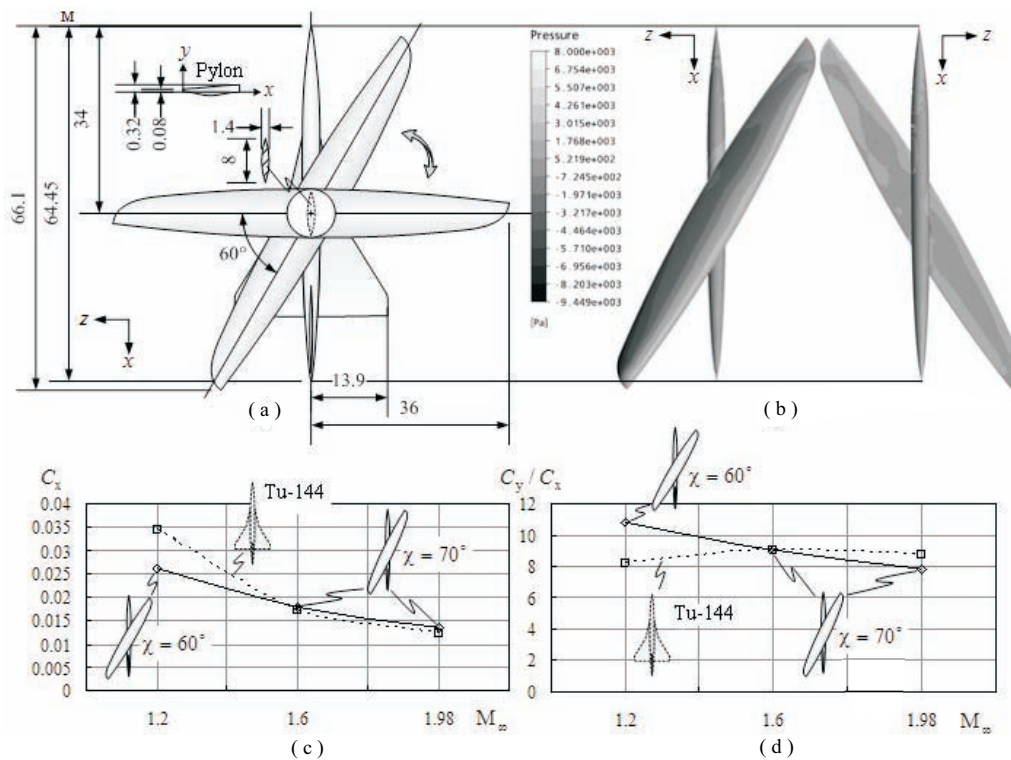
FIG. 3: Comparison of the drag of the aircraft with the oblique wing and of the Tu-144 aircraft: (a) the schemes of the aircraft with the oblique wing and of the Tu-144 aircraft; (b) pressure distribution on the surface of the aircraft with the oblique wing at $M_\infty = 1.2$; (c) drag as a function of the Mach number; (d) lift-drag ratio as a function of the Mach number.

intense on the wing part situated downstream. Therefore, the lift on this part of the wing is greater, which leads to the rise of the roll moment. The fuselage slightly influences the distribution of pressure drop on the aircraft with the oblique wing. Shown in Fig. 3c is the dependence of the drag of the aircraft with the oblique wing and of the Tu-144 aircraft on Mach number. One can see that at $M_\infty = 1.2$, the drag of the aircraft with the oblique wing is less than the drag of the Tu-144 aircraft. The comparison of the lift-drag ratio is presented in Fig. 3d. At $M_\infty = 1.2$, the lift-drag ratio of the aircraft with the oblique wing ($c_y/c_x = 10.76$) is greater than that of the Tu-144 aircraft ($c_y/c_x = 8.21$) by 2.55. As the Mach number increases, the lift-drag ratio of the Tu-144 aircraft becomes greater than the lift-drag ratio of the aircraft with the oblique wing. At $M_\infty = 1.6$, $c_y/c_x = 9.02$ for the aircraft with the oblique wing, and $c_y/c_x = 9.09$ for the Tu-144 aircraft. At $M_\infty = 1.98$, the difference in the lift-drag ratio is equal to 0.95.

TABLE 2: Aircraft parameters.

Parameters	Tu-144 aircraft	Oblique wing aircraft		
		$\chi = 60$ deg	$\chi = 70$ deg	
Aircraft length L, m	64.45	66.1	68.44	
Wing area S_w, m^2	505.868	501		
Airfoil type	Special	NACA 64412		
Span l, m	27.8	36	24.63	
Wing aspect ratio, λ	1.53	2.59	1.21	
		10.35 (at $\chi = 0$)		
Mass, t	150			
Flight altitude, m	16,100			
c_y	$M_\infty =$ | 1.2 | 1.6 | 1.98	$M_\infty =$ | 1.2 | 1.6 | 1.98		
	$c_y =$ | 0.285 | 0.16 | 0.105	$c_y =$ | 0.287 | 0.162 | 0.106		
Grid Form	Tetrahedral			
Grid Number of nodes	1,217,696 (symmetry)	1,724,604	1,846,352	
Grid Number of elements	4,193,568 (symmetry)	5,141,104	5,466,192	

5. COMPARISON OF THE SONIC BOOM INTENSITY

The intensity of the local sonic boom from the aircraft with the oblique wing is calculated during the flight at the altitude 16,100 m, at Mach numbers 1.2, 1.6, 1.98, and aircraft mass 150 t. The calculation results are compared to the data obtained for the Tu-144 aircraft. Shown in Fig. 4a is the pressure distribution on the horizontal plane under the Tu-144 aircraft at $M_\infty = 1.2$, and shown in Fig. 4b is the pressure distribution under the aircraft with the oblique wing also at $M_\infty = 1.2$. It is evident that the maximum disturbance distribution for these aircraft markedly differs. In case of the Tu-144 aircraft, the maximum disturbance area is situated under the wing. In case of the oblique wing, this area is situated upstream, where the shock waves arising from the fuselage nose and the wing forepart join. The pressure distribution integration along the wingspan allows one to specify the equivalent axially symmetrical body area derivative $\bar{S}'_{\text{eq}}$ (Fig. 4c). Shown in Fig. 4d is the curve of the F-function, and shown in Fig. 4e is the sonic boom intensity of the Tu-144 aircraft and of the aircraft with the oblique wing. The maximum overpressure $\Delta p_{\max}$ in a shock wave is equal to 121 Pa for the Tu-144 aircraft and 81 Pa for the aircraft with the oblique wing, with the minimum overpressure $\Delta p_{\min}$ being equal to –107 Pa for the Tu-144 aircraft and –56 for the aircraft with the oblique wing. The difference in $\Delta p_{\max}$ between these two aircraft is equal to 40 Pa, and the difference
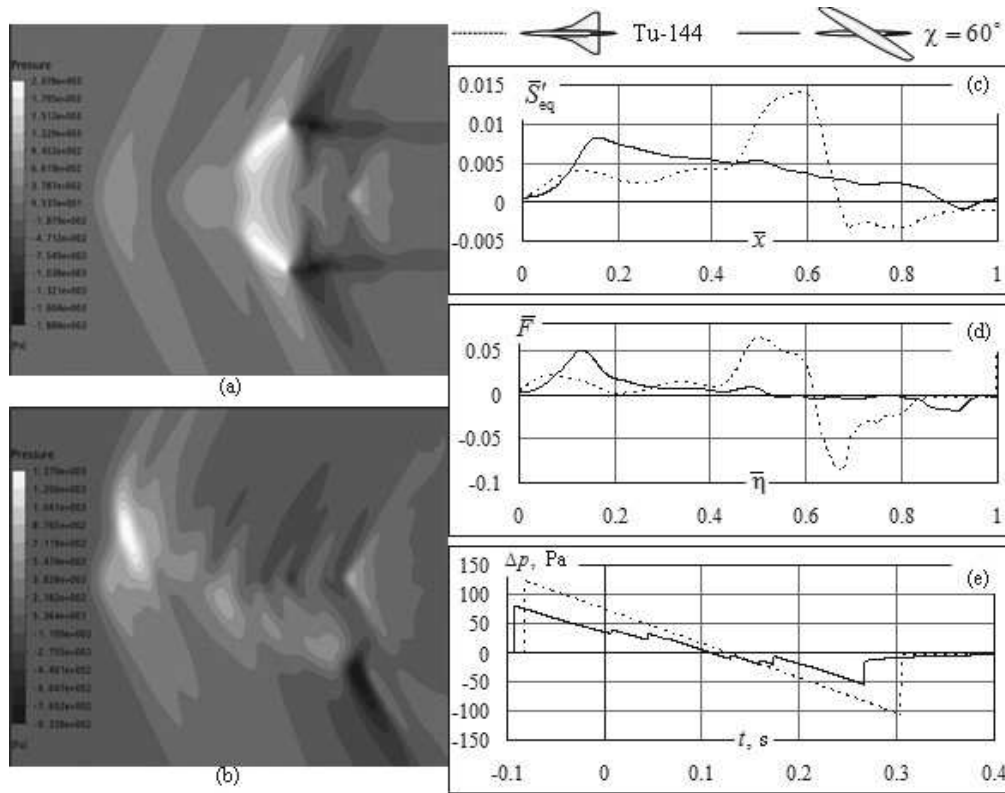
FIG. 4: Sonic boom intensity of the aircraft with the oblique wing and of the Tu-144 aircraft at $M_\infty = 1.2$: (a) pressure field of the Tu-144 aircraft; (b) pressure field of the aircraft with the oblique wing; (c) distribution of the equivalent axially symmetrical body area derivative $(\bar{S}'_{eq})$; (d) distribution of the F-function; (e) overpressure curve in the N-shaped wave.

in Δp_{min} is equal to 51 Pa. This great difference results from the different distributions of the cross-sectional area and of the lift along the x-axis. If the entire wing is situated inside the Mach cone, the disturbances, caused by the oblique wing lift, will spread in a vast area along the x-axis. The variations of the area derivative $\bar{S}'_{eq}$ of the F-function and of the overpressure of the sonic boom are shown in Fig. 5a for $M_\infty = 1.6$, and in Fig. 5b for $M_\infty = 1.98$. In addition, the disturbance distribution pattern on the computational plane and the form of the curve of the equivalent axially symmetrical body derivative $\bar{S}'_{eq}$ do not differ from the calculated ones at the flight mode with $M_\infty = 1.2$. Shown in Table 3 are the maximum and minimum sonic boom intensities of the aircraft with the oblique wing and of the Tu-144 aircraft at $M_\infty = 1.6$ and 1.98. At $M_\infty = 1.6$, the difference in the maximum intensity Δp_{max} is 37 Pa, and the difference in the minimum intensity Δp_{min} is –53 Pa. At $M_\infty = 1.98$, the difference $\Delta p_{max} = 38$ Pa, and at $\Delta p_{min} = 50$.
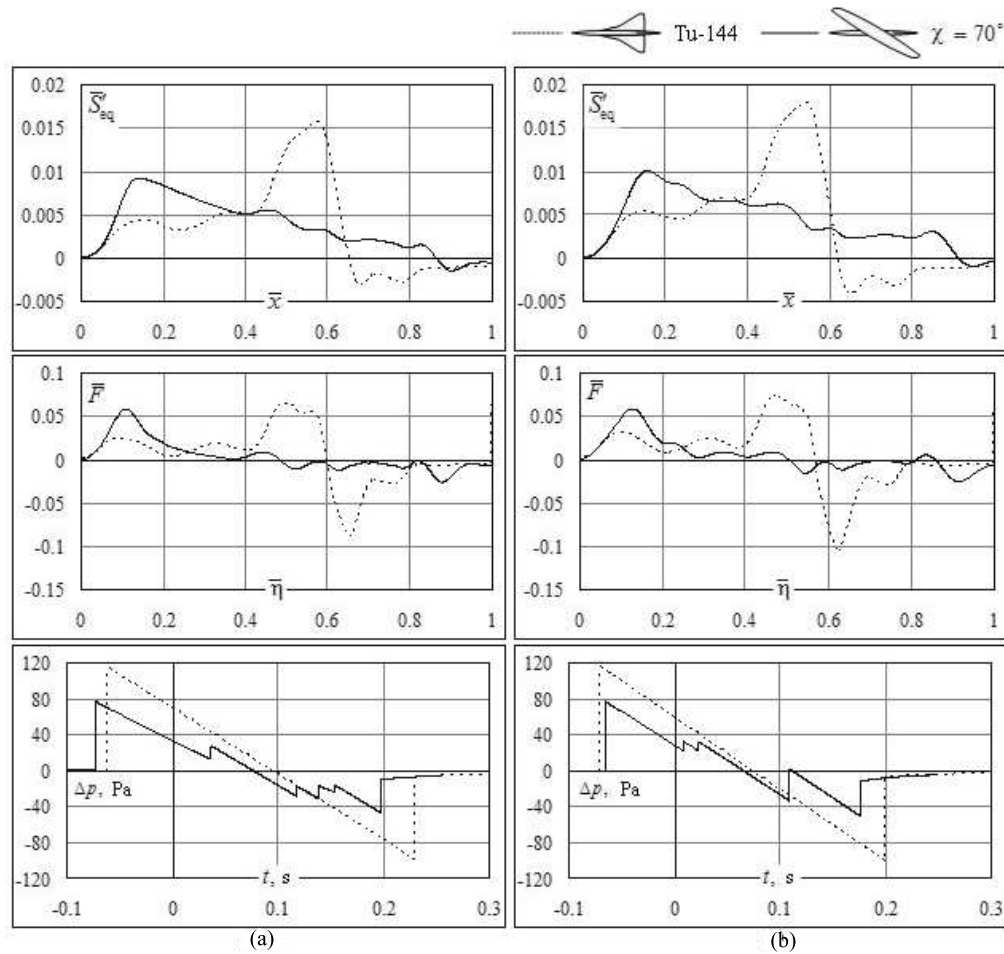
FIG. 5: Sonic boom intensity of the aircraft with the oblique wing and of the Tu-144 aircraft at $M_\infty = 1.6$ and 1.98: (a) sonic boom intensity at $M_\infty = 1.6$; (b) sonic boom intensity at $M_\infty = 1.98$.

TABLE 3: Maximum and minimum sonic boom intensities.

M_∞	Aircraft	Δp_{max}, Pa	Δp_{min}, Pa
1.6	Tu-144	114	-99
	with oblique wing	77	-46
1.98	Tu-144	115	-101
	with oblique wing	77	-51

6. CONCLUSION

Investigated in the present work was the supersonic aircraft with entirely rotating oblique wing, the wing area, the fuselage, and the vertical fins of which were equivalent to the

Tu-144 aircraft. The aircraft with the entirely rotating wing has a remarkable advantage in the sonic boom intensity in comparison with the conventional Tu-144 aircraft at all Mach numbers, and an advantage in the lift-drag ratio at small Mach numbers $(M_\infty = 1.2)$. However, the aircraft with the entirely rotating wing still has some problems to solve concerning the engineering solution of the rotation gear and the roll and longitudinal trim.

REFERENCES

1. Jones, R. T., The oblique wing — aircraft design for transonic and low supersonic speeds, *Acta Astronaut.,* vol. 4, pp. 99–109, 1977.

2. Nelms, Jr., W. P. and Bailey, R. O., Preliminary performance estimates of an oblique all wing RPV for air-to-air combat, NASA TN D-7731, Jul. 1974.

3. Cho, K. C., Analysis of the sonic boom intensity using near-field perturbation under the aircraft, calculated by means of the nonlinear theory, *TsAGI Sci. J.*, vol. XL, no. 4, 2009.

4. ANSYS, Inc., ANSYS CFX-solver, Release 10.0: Theory, Turbulence and Wall Function Theory, 2005.

5. Bliznyuk, V., Vasiliev, L., Vul, V., Klimov, V., Mironov, A., Tupolev, A., Popov, Yu., Pukhov, A., and Cheremukhin, G., *The Truth about Supersonic Passenger Aircrafts*, Moskovskiy Rabochiy, Moscow, 2000.

MOLECULAR-KINETIC DESCRIPTION OF BROWNIAN MOTION OF HEATED NONSPHERICAL PARTICLES IN HIGHLY RAREFIED GAS

V. S. Galkin & S. V. Rusakov[*]

Central Aerohydrodynamic Institute (TsAGI) 1, Zhukovsky str., Zhukovsky, 140180, Moscow region, Russia

[*]Address all correspondence to S. V. Rusakov E-mail: dsmc1@mail.ru

The kinetic equation describing translational and rotational Brownian motion of nonspherical convex solid particles in moving highly rarefied thermally inhomogeneous monatomic gas is derived. The regime of flow around the particles is free molecular, i.e., the characteristic dimensions of particles are much smaller than the average free path of the gas molecules. The interaction between the particles and their effect on the gas phase be neglected. The specular-diffuse law of interaction between the molecules and the particle surface is supposed. The temperatures of particles are equal and differ from the local gas temperature. Such a thermal nonequilibrium leads to the violation of well-known relations between the diffusion coefficients in the spaces of translational and angular velocities and the coefficients of forces and momentums acting on a particle. The coefficients in the Fokker-Planck collision operator entering into the kinetic equation are calculated for the particles in the form of the bodies of revolution. In the case of particles without longitudinal symmetry (circle cone of finite length, hemisphere etc.), the Fokker-Planck collision operator contains the second mixed derivative with respect to the translational and angular velocities.

KEY WORDS: *kinetic Fokker-Planck equation, nonspherical thermally nonequilibrium Brownian particles, fine-dispersed gas suspension*

1. INTRODUCTION

During the derivation of the Fokker-Planck operator for Brownian particles, the assumption of particles being in thermodynamic equilibrium with the gas was formerly used [1, 2]. This fact did not allow to take into account the effect of thermal nonequilibrium, i.e., the difference between temperature T_p of particles and local gas temperature T. In addition, sufficiently symmetric particles were considered, so the force and the torque did not depend on the components of angular and of translational velocity, respectively. Therefore, the Fokker-Planck operator did not contain the second mixed derivative of the distribution function with respect to translational and angular velocities.

Steady increase of interest in the investigations of gas suspension flows (i.e., the flows of mixtures of gas with solid or fluid particles) is caused by corresponding demands from aerospace engineering, applied chemistry, propulsion engineering, etc. Refs. [3–5]. In many cases, it is important to consider the nonequilibrium due to the heating (or cooling) of particles, from chemical processes on their surfaces, etc. The theory of gas suspension mechanics is phenomenological, and sometimes just empirical. The areas based on kinetic theory [6, 7] are developing in order both to derive the equations of motion of gas suspensions as a continuum and to calculate the kinetic coefficients and the relaxation terms as it is done in the kinetic ideal gas theory. Moreover, in some cases, the investigations of gas suspension flows are to be based on molecular-kinetic concepts. Recently, these areas have been stimulated for the development by the investigations of nanoparticles [7]. However, there are a lot of assumptions in the kinetic theory of gas suspensions that is known to be explained by the complexity of the processes under consideration.

The most important method of the theory accuracy analysis is the consideration of the simplest cases when it is possible to create convincing mathematical models. The striking example is described in Ref. [8], where the small-parameter expansions of the Boltzmann integral of collisions between heavy particles and light ones is implemented on the assumption that all the molecules are elastic spheres. As a result, the kinetic Fokker-Planck equation is derived from the kinetic Boltzmann equation for Brownian free molecular spherical particles whose surfaces the gas molecules interact with according to the specular reflection law. However, it was used to consider the kinetic Boltzmann equation to be inapplicable for the description of Brownian motion of particles, being due to the collective (and not binary) action of medium molecules; therefore, the result of Ref. [8]) enlarged the representations about the range of applicability of this equation. This result can be generalized for taking into account the thermophoretic force acting on a specular reflecting sphere in free molecular conditions, i.e., at a Knudsen number of the Brownian particle $\text{Kn} \gg 1$, by applying the equations from Ref. [9] obtained for the special case of molecules considered as elastic spheres.

After that [10], the natural question arises of whether the Fokker-Planck kinetic equation can be obtained in a similar way for other laws of interactions of molecules of surrounding gas with the solid particle surface (instead of the specular law), especially for the important diffusion law from the Boltzmann-type equation. By definition, in the Boltzmann-type equation, the convective part equals the collision operator, characterizing the difference between the number of particles incoming and outgoing from the phase space element. It is required to construct this operator theory on the basis of the free molecule flow theory with further application of the small-parameter expansions by analogy with Ref. [8] assuming that the collisions of gas molecules with the particle surface are instant (i.e., the collision time is assumed to be negligibly small in comparison with characteristic times of translational and rotational motions of particles), so that the operator is calculated at a fixed particle orientation. The heating (cooling) of

the particle does not crucially transform the character of the interaction processes between the gas and the particle; therefore, the temperatures of the particles are assumed to be identical and to differ from the gas temperature. This fact enables to investigate the thermal nonequilibrium influence on the operator coefficients and to use the results of the investigations for experiments on the problem of applicability of Boltzmann-type equations.

Such a program is realized in Ref. [10–12] and in the present work. In each of them, the major result for this mathematical model is underlined, namely, in the absence of thermal nonequilibrium, i.e., at the equality of the temperatures of particles and of gas, the equations obtained turn into the well-known kinetic equations for Brownian free molecular particles determined by means of principally different techniques. This shows that Boltzmann-type equations are applicable for the derivation of kinetic equations for Brownian free molecular paricles.

The kinetic theory of the Fokker-Planck operator for free molecular thermal nonequilibrium particles has been developed recently. At first, this theory was developed for a spherical particle in stationary homogeneous gas at the diffuse law of the reflection of gas molecules from the wall [10], and then a generalization has been carried out for the case of a moving gas with a temperature inhomogeneity at the specular-diffuse reflection law [11]. After that, the same statement of the problem has been extended to nonspherical particles [12], where the coefficients in the sought operator are calculated for the particles taken as the rotational bodies with longitudinal symmetry. [According to the terminology of Ref. [13], such bodies possess a symmetry plane that is perpendicular to the axis of symmetry; for example, spheroids [12]. In this case, the collision operator does not contain term with the second mixed derivative. Thermal nonequilibrium leads to significant variations of known expressions for the diffusion coefficients in the spaces of translational and rotational velocities of particles in terms of the coefficients of forces and moments acting on moving particle. Generally speaking, the degree of this variation depends on the accommodation coefficient and on the shape of a particle [11, 12].

Stated below in more details than in Ref. [12] is the derivation of the kinetic equation describing translational and rotational Brownian motion of free molecular particles in a nonhomogeneous gas with the parameter of thermal nonequilibrium being not equal to unity $\tau \equiv T_p/T \neq 1$ and at an arbitrary law of interaction between gas molecules and a particle surface. Next, the specular-diffuse law of interaction is used, with only a slight nonhomogeneity of the gas temperature being considered. The integration in multidimensional quadratures contained in the collision operator is carried out with respect to the relative velocities of molecules before and after the collision with the particle surface element. Final explicit expressions are obtained for a hemisphere and for a circular cone when the second mixed derivative of the distribution function appears in the Fokker-Planck operator.

As before [10–12], the density of the particulate phase (assembly of particles) is assumed to be so small that the collisions of particles and their influence on the flow pa-

rameters of the carrier phase (the gas) are inessential. The maximum particle dimension d_m is much smaller than the mean-free-path length of molecules, but much larger than the diameter of a molecule, so the particle may be assumed to be a macroscopic body interacting with the gas by the laws of free molecular flows (for brevity, the particles at such conditions are called the free molecules [11,12]).

The particles are assumed to be convex, solid, and mass and temperature homogenious. The velocity of the gas is **U** in a fixed frame of reference, and its mass density ρ and temperature T are constant at a length about d_m. The differences of characteristic phase velocities are much less than the characteristic thermal velocity of the molecules. The gradient ∇T is set away from the particle, with the thermophoretic force resulting from it.

Some errors made previously in Refs. [10–12] are corrected hereafter in this work. Basic misprints [10, 11] are indicated in Refs. [11, 12], respectively. In the first equation (2.5) of Ref. [12], $\varphi \rightarrow -\lambda\varphi/(5nkT)$, the minus sign must be omitted. The errors in equations are most numerous in the English version of Ref. [12].

2. KINETIC EQUATION

The assumptions [10–12] applicable to the derivation of Boltzmann-type equation are used. The time of interaction (collision) of the molecule with a particle surface is much shorter than the characteristic time of variation of the particle distribution function F_p. The variation of particle orientation during the collision is unessential, so the operator of collisions is derived at constant values of Eulerian angles. Meanwhile, it is possible to involve the known results from the kinetic theory of gas consisting of nonspherical molecules that are considered within classical mechanics [14].

The variation of the distribution function $F_p \equiv F_p\left(\mathbf{r}, t, \mathbf{\xi}_p, \mathbf{\omega}_p, \mathbf{\alpha}\right)$ in a phase space element is described by the following expression:

$$\mathfrak{D} F_p d\mathbf{r}dtd\mathbf{\xi}_p d\mathbf{\omega}_p d\mathbf{\alpha} = (\Delta_+ - \Delta_-)\, d\mathbf{r}dtd\mathbf{\alpha} \equiv J d\mathbf{r}dtd\mathbf{\xi}_p d\mathbf{\omega}_p d\mathbf{\alpha} \qquad (2.1)$$

The convective operator $\mathfrak{D} F_p$ is determined by the following equation [14]:

$$\mathfrak{D} F_p = \frac{\partial F_p}{\partial t} + \frac{\partial}{\partial \mathbf{r}} \cdot \left(\mathbf{\xi}_p F_p\right) + \frac{\partial}{\partial \mathbf{\xi}_p} \cdot \left(\mathbf{\Phi} F_p\right) + \frac{\partial}{\partial \mathbf{\omega}_p} \cdot \left(\dot{\mathbf{\omega}}_p F_p\right) + \frac{\partial}{\partial \mathbf{\alpha}} \cdot \left(\dot{\mathbf{\alpha}} F_p\right)$$

$$\dot{\mathbf{\alpha}} \equiv \frac{\partial \mathbf{\alpha}}{\partial t} \qquad\qquad (2.2)$$

The value $(\Delta_+ - \Delta_-)$ is equal to the difference between the number of particles incoming and outgoing from the phase space element during the time unit at constant values of Eulerian angles. This value determines the operator of collisions J using the second equality of Eq. (2.1).

There are the following notations in Eqs. (2.1) and (2.2): ξ_p is a center-of-mass velocity of a particle relative to the fixed frame of reference; ω_p is its angular velocity; $\mathbf{r}$ is a radius vector of the center of mass; t is a time; α is a vector whose components are equal to Eulerian angles; Φ is an external force related to the particle mass m_p.

Initiating calculation of the difference $(\Delta_+ - \Delta_-)$, let us introduce the velocities of particles and of molecules relative to the local gas velocity $\mathbf{U}$ [11] in order to take into account the motion of gas,

$$\mathbf{W}_p = \xi_p - \mathbf{U}, \mathbf{W} = \xi - \mathbf{U}, \mathbf{U} = \mathbf{U}(\mathbf{r},\ t)$$

The equations connecting the velocities of molecules and of particles before collision with the same variables after collision are as follows:

$$\mathbf{W}' = \mathbf{W} - \frac{\mathbf{G}}{m}, \quad \mathbf{W}'_p = \mathbf{W}_p + \frac{\mathbf{G}}{m_p}, \quad \omega'_p = \omega_p + \mathbf{I}^{-1} \cdot [\mathbf{x} \times \mathbf{G}] \tag{2.3}$$

Here, m, m_p are the masses of a gas molecule and of a particle, respectively; the stroke designates the values after collision; $\mathbf{W}', \mathbf{W}$ are the relative velocities of molecules after collision and before it; $\mathbf{G}$ is a momentum transmitted during collision; $\mathbf{I}$ is a tensor of inertia of a particle relative to the moving frame of reference starting in its center of mass; $\mathbf{x} = R\mathbf{e}$ is a radius vector of an arbitrary point at a particle surface in this frame of reference; R is a length of radius vector (variable over the particle surface in contrast to the sphere [10,11]); and $\mathbf{e}$ is a corresponding unit vector. By definition, $\mathbf{I} \cdot \mathbf{I}^{-1} = \mathbf{E}$, where $\mathbf{E}$ is a unit tensor, and symbol $\mathbf{T}^{-1}$ introduces a tensor inverse to tensor $\mathbf{T}$. The point signifies the scalar product of vectors as well as the simple (inner) product of a second rank tensor by vector or by a second rank tensor; two points signify the double product of second rank tensors, for example, $\mathbf{u} \cdot \mathbf{n}, \mathbf{T} \cdot \mathbf{u}, \mathbf{T} \cdot \mathbf{T}', \mathbf{T} : \mathbf{T}'$ respectively, where $\mathbf{u}, \mathbf{n}$ are vectors, and $\mathbf{T}'$ is a tensor. The sign $\times$ signifies the vector product that is put in square brackets when it is a factor in an equation, for example, $[\mathbf{u} \times \mathbf{n}]$. Applied for dyads are common notations $\mathbf{uu}$, $\mathbf{nn},$ etc. Other factors are put in brackets if necessary; the expression $\mathbf{T} : (\mathbf{T}' \cdot \mathbf{uu})$ is a double product of tensor $\mathbf{T}$ by a tensor equal to the ordinary product of tensor $\mathbf{T}'$ by a dyad $\mathbf{uu}$. The following symbols are also applicable later (k is Boltzmann constant):

$$\mathbf{g} = \mathbf{W} - \mathbf{v}, \quad \mathbf{g}' = \mathbf{W}' - \mathbf{v}', \quad \mathbf{v} = \mathbf{W}_p - \mathbf{x} \times \omega_p, \quad \Delta\mathbf{g} = \mathbf{g}' - \mathbf{g},$$

$$\Sigma = m_p \mathbf{I}^{-1} \cdot [\mathbf{x} \times \Delta\mathbf{g}], \quad \varepsilon = m(m_p + m)^{-1}, \quad \mu = \varepsilon m_p, \quad h = 2kTm^{-1} \tag{2.4}$$

The exclusion of momentum $\mathbf{G}$ from Eq. (2.3) is fulfilled earlier [12]. As a result, the following relationships are found:

$$\begin{pmatrix} \mathbf{W}'_p \\ \mathbf{W}' \end{pmatrix} = \begin{pmatrix} \mathbf{W}_p \\ \mathbf{W} \end{pmatrix} + [\mathbf{e}(\mathbf{e} \cdot \Delta\mathbf{g}) - \mathbf{\Omega}] \begin{pmatrix} -\varepsilon \\ 1 - \varepsilon \end{pmatrix} - \mathbf{\Psi} \Xi \begin{pmatrix} m_p^{-1} \\ -m^{-1} \end{pmatrix},$$

$$\omega'_p = \omega_p + \mathbf{I}^{-1} \cdot \{[\mathbf{x} \times \mathbf{\Omega}] \varepsilon m_p - [\mathbf{x} \times \mathbf{\Psi}] \Xi\},$$

$$\boldsymbol{\Omega} = \mathbf{e} \times \left(\boldsymbol{\Pi} \cdot [\mathbf{e} \times \Delta \mathbf{g}] \right), \quad \boldsymbol{\Psi} = \mathbf{e} \times \left(\boldsymbol{\Pi} \cdot \mathbf{e} \right), \quad \boldsymbol{\Pi} = \left(\mathbf{E} + \mu \mathbf{I}^{-1} R^2 \right)^{-1},$$

$$\Xi = -\mu^2 \left\{ 1 - \mathbf{x} \cdot \left(\mathbf{I}^{-1} \cdot [\boldsymbol{\Pi} \cdot \mathbf{x}] \right) \mu \right\}^{-1} \left\{ \mathbf{x} \cdot \mathbf{I}^{-1} \cdot \left(\boldsymbol{\Pi} \cdot [\mathbf{x} \times \Delta \mathbf{g}] \right) \right\}. \tag{2.5}$$

The number of collisions of molecules having the velocities from the element $d\mathbf{W}$ with the particles having the velocities from element $d\mathbf{W}_p d\boldsymbol{\omega}_p$ is equal to

$$|\mathbf{n} \cdot \mathbf{g}| \, f\left(\mathbf{r}, t, \mathbf{W} \right) d\mathbf{W} dS F_p\left(\mathbf{r}, t, \mathbf{W}_p, \boldsymbol{\omega}_p, \boldsymbol{\alpha} \right) \, d\mathbf{W}_p d\boldsymbol{\omega}_p d\boldsymbol{\alpha} \, d\mathbf{r} dt$$

Here, $\mathbf{n}$ is an external normal unit vector to the particle surface element dS and f is a distribution function of molecules. Furthermore, for brevity, the arguments $\mathbf{r}$, t in the distribution functions will be omitted.

When the molecule impacts with a particle, the velocity of the latter does not change; therefore, the argument $\boldsymbol{\alpha}$ in the function of the distribution of particles F_p is also omitted.

The probability of the fact that the molecules after reflection from the element dS get relative velocities from the element $d\mathbf{g}'$ is $P\left(\mathbf{g}, \mathbf{g}' \right) d\mathbf{g}'$, where P is related to the flow of incoming molecules, i.e., the total probability of molecule emission [the integral of $P\left(\mathbf{g}, \mathbf{g}' \right)$ over the region $\mathbf{n} \cdot \mathbf{g}' > 0$] is equal to unity. As a result, the following equation is obtained:

$$\Delta_- = \int\limits_{\mathbf{n} \cdot \mathbf{g} < 0} \int\limits_{\mathbf{n} \cdot \mathbf{g}' > 0} \int\limits_{S} |\mathbf{n} \cdot \mathbf{g}| \, f\left(\mathbf{W} \right) P\left(\mathbf{g}, \mathbf{g}' \right) F_p\left(\mathbf{W}_p, \boldsymbol{\omega}_p \right) d\mathbf{W} d\mathbf{g}' d\mathbf{W}_p d\boldsymbol{\omega}_p dS \tag{2.6}$$

The number of collisions that convert the velocities $\mathbf{W}', \mathbf{W}'_p, \boldsymbol{\omega}'_p$ into $\mathbf{W}, \mathbf{W}_p, \boldsymbol{\omega}_p$ is calculated in the same way. Therefore, we have

$$\Delta_+ = \int\limits_{\mathbf{n} \cdot \mathbf{g}' < 0} \int\limits_{\mathbf{n} \cdot \mathbf{g} > 0} \int\limits_{S} |\mathbf{n} \cdot \mathbf{g}'| \, f\left(\mathbf{W}' \right) P\left(\mathbf{g}', \mathbf{g} \right) F_p\left(\mathbf{W}'_p, \boldsymbol{\omega}'_p \right) d\mathbf{W}' d\mathbf{g} d\mathbf{W}'_p d\boldsymbol{\omega}'_p dS \tag{2.7}$$

Using Eq. (2.5), it is possible to demonstrate that Jacobian determinants of transformations of variables $\mathbf{W}, \mathbf{g}', \mathbf{W}_p, \boldsymbol{\omega}_p \rightarrow \mathbf{W}', \mathbf{g}, \mathbf{W}'_p, \boldsymbol{\omega}'_p \rightarrow \mathbf{g}, \mathbf{g}', \mathbf{W}_p, \boldsymbol{\omega}_p$ are of block form and equal to unity. As a result, using Eqs. (2.1), (2.4), (2.6), and (2.7), we find the kinetic equation of the Boltzmann type

$$\mathfrak{D} F_p = J \tag{2.8}$$

The left part of Eq. (2.8) is determined from Eq. (2.2). The following equation can be found in the collision operator right-hand side:

$$J = \int \left\{ H\left(-\mathbf{n} \cdot \mathbf{g}' \right) H\left(\mathbf{n} \cdot \mathbf{g} \right) |\mathbf{n} \cdot \mathbf{g}'| \, f\left(\mathbf{g}' + \mathbf{v}' \right) P\left(\mathbf{g}', \mathbf{g} \right) \, F_p\left(\mathbf{W}'_p, \boldsymbol{\omega}'_p \right) \right.$$
$$\left. - H(-\mathbf{n} \cdot \mathbf{g}) H\left(\mathbf{n} \cdot \mathbf{g}' \right) |\mathbf{n} \cdot \mathbf{g}| \, f(\mathbf{g} + \mathbf{v}) P\left(\mathbf{g}, \mathbf{g}' \right) F_p(\mathbf{W}_p, \boldsymbol{\omega}_p) \right\} d\mathbf{g} d\mathbf{g}' dS \tag{2.9}$$

Here, the integration is implemented over the complete velocity spaces; the function $H(y)$ is equal to 1 for $y > 0$ and to 0 for $y < 0$, the vector $\mathbf{v}$ is determined by the third equation of Eq. (2.4). The variables $\mathbf{W}', \mathbf{W}'_p, \boldsymbol{\omega}'_p$ in the first term of the expression under the integral sign of Eq. (2.9) are the substituted by right-hand sides of the first three equations (2.5), then the variables $\mathbf{g}'$ and $\mathbf{g}$ are renamed to $\mathbf{g}$ and $\mathbf{g}'$. For example,

$$f\left(\mathbf{g}' + \mathbf{v}'\right) = f\left(\mathbf{W}'\right) = f\left(\mathbf{W} + \Delta\mathbf{g} - \Delta_\eta\right) = f\left(\mathbf{v} + \mathbf{g}' - \Delta_\eta\right) \rightarrow f\left(\mathbf{v} + \mathbf{g} + \Delta_\eta\right)$$
$$= f\left(\boldsymbol{\eta} + \Delta_\eta\right)$$

After that, Eq. (2.9) for operator J takes on the form

$$J = \int [f\left(\boldsymbol{\eta} + \boldsymbol{\Delta}_\eta\right) F_p(\mathbf{W}_p + \boldsymbol{\Delta}_\xi, \boldsymbol{\omega}_p + \boldsymbol{\Delta}_\omega) - f(\boldsymbol{\eta}) F_p(\mathbf{W}_p, \boldsymbol{\omega}_p)] d\boldsymbol{\Theta} \equiv \int [\Im] \, d\boldsymbol{\Theta},$$

$$d\boldsymbol{\Theta} = H\left(-\mathbf{n} \cdot \mathbf{g}\right) H\left(\mathbf{n} \cdot \mathbf{g}'\right) |\mathbf{n} \cdot \mathbf{g}| \, P\left(\mathbf{g}, \ \mathbf{g}'\right) d\mathbf{g} d\mathbf{g}' dS, \quad \boldsymbol{\eta} = \mathbf{g} + \mathbf{v},$$

$$\begin{pmatrix} \boldsymbol{\Delta}_\xi \\ \boldsymbol{\Delta}_\eta - \Delta\mathbf{g} \end{pmatrix} = -\left[\mathbf{e}\left(\mathbf{e} \cdot \Delta\mathbf{g}\right) - \boldsymbol{\Omega}\right] \begin{pmatrix} -\varepsilon \\ 1 - \varepsilon \end{pmatrix} + \boldsymbol{\Psi}\boldsymbol{\Xi} \begin{pmatrix} m_p^{-1} \\ -m^{-1} \end{pmatrix},$$

$$\boldsymbol{\Delta}_\omega = -\mathbf{I}^{-1} \cdot \{[\mathbf{x} \times \boldsymbol{\Omega}] \, \varepsilon \, m_p - [\mathbf{x} \times \boldsymbol{\Psi}] \, \boldsymbol{\Xi}\} \qquad (2.10)$$

Used in the two latest equations are the symbols from Eq. (2.5). Furthermore, analogous to Ref. [10], we apply the infinitesimality $\varepsilon \ll 1$ on the assumption that the translational and the rotational velocities of particles are on the order of ε as compared to the mean thermal velocity of the gas molecules. We linearize expression $\Im$, put in square brackets of the first formula of Eq. (2.10), by $\Delta_\eta, \Delta_\xi, \Delta_\omega$, which are small in comparison with $\eta, \mathbf{W}_p, \boldsymbol{\omega}_p$, relatively. Therefore, we find the following:

$$\Im = F_p \left(\frac{\partial f}{\partial \boldsymbol{\eta}} \cdot \boldsymbol{\Delta}_\eta\right) + f \left(\frac{\partial F_p}{\partial \mathbf{W}_p} \cdot \boldsymbol{\Delta}_\xi + \frac{\partial F_p}{\partial \boldsymbol{\omega}_p} \cdot \boldsymbol{\Delta}_\omega\right) + \frac{1}{2} F_p \frac{\partial^2 f}{\partial \boldsymbol{\eta} \partial \boldsymbol{\eta}} : (\boldsymbol{\Delta}_\eta \boldsymbol{\Delta}_\eta)$$

$$+ \frac{1}{2} f \left[\frac{\partial^2 F_p}{\partial \mathbf{W}_p \partial \mathbf{W}_p} : (\boldsymbol{\Delta}_\xi \boldsymbol{\Delta}_\xi) + \frac{\partial^2 F_p}{\partial \mathbf{W}_p \partial \boldsymbol{\omega}_p} : (\boldsymbol{\Delta}_\xi \boldsymbol{\Delta}_\omega) + \frac{\partial^2 F_p}{\partial \boldsymbol{\omega}_p \partial \boldsymbol{\omega}_p} : (\boldsymbol{\Delta}_\omega \boldsymbol{\Delta}_\omega)\right.$$

$$\left. + \frac{\partial^2 F_p}{\partial \boldsymbol{\omega}_p \partial \mathbf{W}_p} : (\boldsymbol{\Delta}_\omega \boldsymbol{\Delta}_\xi)\right]$$

Indicated here for brevity are $F_p \equiv F_p\left(\mathbf{W}_p, \boldsymbol{\omega}_p\right), f \equiv f\left(\boldsymbol{\eta}\right)$.

Now, we expand Eq. (2.10) in ε for $\boldsymbol{\Delta}_\eta, \boldsymbol{\Delta}_\xi, \boldsymbol{\Delta}_\omega$, taking into account Eq. (2.5) and a known relationship,

$$\left(\mathbf{E} + \varepsilon \, \mathbf{T}\right)^{-1} \approx \mathbf{E} - \varepsilon \, \mathbf{T}, \quad \mathbf{E}^{-1} = \mathbf{E},$$

Here, $\mathbf{E}$ and $\mathbf{T}$ are the unit and arbitrary tensors of second rank, respectively. Omitting the higher-ε-order terms, we obtain the following equations:

$$\boldsymbol{\Delta}_\xi \approx \varepsilon \, \Delta\mathbf{g}, \quad \boldsymbol{\Delta}_\eta \approx \varepsilon \, \Delta\mathbf{g} - \varepsilon \left[\mathbf{x} \times \boldsymbol{\Sigma}\right], \quad \boldsymbol{\Delta}_\omega \approx \varepsilon \, \boldsymbol{\Sigma}$$

Here, the value $\boldsymbol{\Sigma}$ is determined by the fifth formula of Eq. (2.4). Taking into account these expressions and the equation $\boldsymbol{\eta} = \mathbf{g} + \mathbf{W}_p - \mathbf{x} \times \boldsymbol{\omega}_p$, we have

$$\frac{\partial f}{\partial \mathbf{W}_p} = \frac{\partial f}{\partial \boldsymbol{\eta}}, \quad \frac{\partial^2 f}{\partial \mathbf{W}_p \partial \mathbf{W}_p} = \frac{\partial^2 f}{\partial \boldsymbol{\eta} \partial \boldsymbol{\eta}}, \quad \frac{\partial f}{\partial \boldsymbol{\omega}_p} \cdot \boldsymbol{\Delta}_\omega = -\frac{\partial f}{\partial \boldsymbol{\eta}} \cdot \left[\mathbf{x} \times \boldsymbol{\Sigma}\right],$$

$$\frac{\partial^2 f}{\partial \boldsymbol{\omega}_p \partial \boldsymbol{\omega}_p} : (\boldsymbol{\Sigma}\boldsymbol{\Sigma}) = \frac{\partial^2 f}{\partial \boldsymbol{\eta} \partial \boldsymbol{\eta}} : \left(\left[\mathbf{x} \times \boldsymbol{\Sigma}\right] \left[\mathbf{x} \times \boldsymbol{\Sigma}\right]\right),$$

$$\frac{\partial^2 f}{\partial \mathbf{W}_p \partial \boldsymbol{\omega}_p} : (\boldsymbol{\Sigma}\Delta\mathbf{g}) = -\frac{\partial^2 f}{\partial \boldsymbol{\eta} \partial \boldsymbol{\eta}} : \left(\left[\mathbf{x} \times \boldsymbol{\Sigma}\right] \Delta\mathbf{g}\right)$$

The result obtained enables us to write the considered value $\Im$ as follows:

$$\Im = \varepsilon \left\{\frac{\partial F_p}{\partial \mathbf{W}_p} \cdot \Delta\mathbf{g} + \frac{\partial F_p}{\partial \boldsymbol{\omega}_p} \cdot \boldsymbol{\Sigma}\right\} f + \frac{\varepsilon^2}{2} \left\{\frac{\partial^2 F_p}{\partial \mathbf{W}_p \partial \mathbf{W}_p} : (\Delta\mathbf{g}\Delta\mathbf{g})\right.$$

$$\left. + \frac{\partial^2 F_p}{\partial \boldsymbol{\omega}_p \partial \boldsymbol{\omega}_p} : (\boldsymbol{\Sigma}\boldsymbol{\Sigma}) + \frac{\partial^2 F_p}{\partial \mathbf{W}_p \partial \boldsymbol{\omega}_p} : (\Delta\mathbf{g}\boldsymbol{\Sigma}) \right\} f$$

Now, we use once again the assumption about the infinitesimality of the velocities of particles,

$$f(\boldsymbol{\eta}) = f(\mathbf{g} + \mathbf{v}) \approx f(\mathbf{g}) + \mathbf{v} \cdot \frac{\partial f(\mathbf{g})}{\partial \mathbf{g}}, \quad \mathbf{v} \cdot \frac{\partial f(\mathbf{g})}{\partial \mathbf{g}} \sim \varepsilon,$$

$$\mathbf{g} \cdot \frac{\partial}{\partial \mathbf{W}_p} \sim \frac{1}{\varepsilon}, \quad (\mathbf{g}\,\mathbf{g}) : \frac{\partial^2}{\partial \boldsymbol{\omega}_p \partial \boldsymbol{\omega}_p} \sim \frac{l_p^2}{\varepsilon^2}$$

etc. (here, l_p is a maximum dimension of a particle).

Holding the dominant terms of expansions, we obtain the following relationships for the collisions operator:

$$J = \frac{\partial}{\partial \mathbf{W}_p} \cdot \left(-\frac{\mathbf{F}}{m_p} F_p\right) + \frac{\partial}{\partial \boldsymbol{\omega}_p} \cdot \left(-\mathbf{M}^* F_p\right)$$

$$+ \frac{\varepsilon}{2m_p} \left\{\frac{\partial^2 F_p}{\partial \mathbf{W}_p \partial \mathbf{W}_p} : \langle \Delta\mathbf{g}\Delta\mathbf{g} f \rangle + \frac{\partial^2 F_p}{\partial \boldsymbol{\omega}_p \partial \boldsymbol{\omega}_p} : \langle \boldsymbol{\Sigma}\boldsymbol{\Sigma} f \rangle + 2\frac{\partial^2 F_p}{\partial \mathbf{W}_p \partial \boldsymbol{\omega}_p} : \langle \Delta\mathbf{g}\boldsymbol{\Sigma} f \rangle\right\} \quad (2.11)$$

$$-\mathbf{F} = \langle \Delta\mathbf{g}\, f \rangle + \left\langle \Delta\mathbf{g}\, \frac{\partial f}{\partial \mathbf{g}}\right\rangle \cdot \mathbf{W}_p + \left\langle \Delta\mathbf{g} \left[\mathbf{x} \times \frac{\partial f}{\partial \mathbf{g}}\right]\right\rangle \cdot \boldsymbol{\omega}_p \qquad (2.12)$$

$$-\mathbf{M}^* m_p = \langle \mathbf{\Sigma} f \rangle + \left\langle \mathbf{\Sigma} \left[\mathbf{x} \times \frac{\partial f}{\partial \mathbf{g}} \right] \right\rangle \cdot \mathbf{\omega}_p + \left\langle \mathbf{\Sigma} \frac{\partial f}{\partial \mathbf{g}} \right\rangle \cdot \mathbf{W}_p, \quad \mathbf{\Sigma} = m_p \mathbf{I}^{-1} \cdot [\mathbf{x} \times \Delta \mathbf{g}] \quad (2.13)$$

$$f = f(\mathbf{g}), \quad F_p = F_p(\mathbf{W}_p, \mathbf{\omega}_p), \quad \langle \Lambda \rangle \equiv m \int\limits_{\mathbf{n} \cdot \mathbf{g} < 0} \int\limits_{\mathbf{n} \cdot \mathbf{g}' > 0} \int\limits_{S} \Lambda d\mathbf{\Theta}$$

It should be emphasized that $f \equiv f(\mathbf{g})$ in Eqs. (2.11)–(2.13) and later. The differential $d\mathbf{\Theta}$ is determined by the second formula of Eq. (2.10). Let us remember that the point introduces the scalar product of vectors and the simple (inner) product of tensor by vector or by tensor, and two points signify the double product of tensors. In the present case, these tensors are dyads that can be written as follows:

$$\frac{\partial^2 F_p}{\partial \mathbf{W}_p \partial \mathbf{W}_p}, \quad \Delta \mathbf{g} \, \Delta \mathbf{g}, \quad \Delta \mathbf{g} \left[\mathbf{x} \times \frac{\partial f}{\partial \mathbf{g}} \right], \quad \mathbf{\Sigma} \frac{\partial f}{\partial \mathbf{g}}$$

3. OPERATOR OF COLLISIONS

The expression for the operator J is general. To specify it, let us take the specular-diffusion law of reflection to be reasonable, when

$$P(\mathbf{g}, \mathbf{g}') = (1 - \alpha) \, \delta \{ \mathbf{g}' - \mathbf{g} + 2\mathbf{n}(\mathbf{n} \cdot \mathbf{g}) \} + \alpha \frac{2}{\pi} h_p^{-2} |\mathbf{n} \cdot \mathbf{g}'| \exp \left(-\frac{g'^2}{h_p} \right),$$

$$\mathbf{n} \cdot \mathbf{g}' > 0, \quad h_p = \frac{2kT_p}{m}, \quad \alpha = [0, 1] = \text{const}$$

where α is a diffusion factor (it is also called an accommodation coefficient of tangential momentum; at $\alpha = 1$, there is a diffuse reflection), and δ is a delta function.

It is assumed [11, 12] that the distribution function of molecules f is defined from the first approximation of the Chapman-Enskog method, with only the term caused by the gas temperature nonhomogeneity being taken into account. Therefore, the following representation takes place in a fixed frame of reference:

$$f(\mathbf{g}) = f_0(g^2)(1 + \psi^T), \quad f_0(g^2) = \frac{\rho}{m} (h\pi)^{-3/2} \exp \left(-\frac{g^2}{h} \right), \quad \psi^T = -\tilde{A}(g^2) \mathbf{g} \cdot \nabla T$$

It is the first term of function $\tilde{A}(g^2)$ expansion in Sonin polynominals that is considered. The accuracy analysis of such an approximation was implemented earlier in Ref. [11].

The first terms of Eqs. (2.12) and (2.13) take the form

$$\langle \Delta \mathbf{g} f \rangle = \langle \Delta \mathbf{g} f_0 (1 + \psi^T) \rangle, \quad \langle \mathbf{\Sigma} f \rangle = \langle \mathbf{\Sigma} f_0 (1 + \psi^T) \rangle$$

The function f is substituted by f_0 in all other terms of Eqs. (2.11)–(2.13). As a result, the following expression for the Fokker-Planck operator is obtained:

$$J = \frac{\partial}{\partial \boldsymbol{\xi}_p} \cdot \left\{ -\frac{\mathbf{F}}{m_p} F_p + \mathbf{D}_\xi \cdot \frac{\partial F_p}{\partial \boldsymbol{\xi}_p} \right\} + \frac{\partial}{\partial \boldsymbol{\omega}_p} \cdot \left\{ \left(-\mathbf{M} \cdot \mathbf{I}^{-1} \right) F_p + \mathbf{D}_\omega \cdot \frac{\partial F_p}{\partial \boldsymbol{\omega}_p} \right\}$$
$$+ \mathbf{D}_{\xi\omega} : \frac{\partial^2 F_p}{\partial \boldsymbol{\xi}_p \partial \boldsymbol{\omega}_p} \tag{3.1}$$

The force $\mathbf{F}$ and the torque $\mathbf{M}$ acting on a particle are caused by its translational motion, by the gas temperature gradient, and by rotation of the particle. According to this,

$$\mathbf{F} = \mathbf{F}_\xi + \mathbf{F}_T + \mathbf{F}_\omega, \quad \mathbf{M} = \mathbf{M}_\xi + \mathbf{M}_T + \mathbf{M}_\omega \tag{3.2}$$

There are the following terms in the first Eq. (3.2):

$$\mathbf{F}_\xi = A \left\langle\!\left\langle \left(\mathbf{U} - \boldsymbol{\xi}_p \right) \right\rangle\!\right\rangle + B\,(1) \left\langle\!\left\langle \mathbf{n} \left[\left(\mathbf{U} - \boldsymbol{\xi}_p \right) \cdot \mathbf{n} \right] \right\rangle\!\right\rangle$$

$$\mathbf{F}_T = \frac{1}{p} \left\{ \frac{A}{5} \left\langle\!\left\langle \mathbf{q}_T \right\rangle\!\right\rangle + \left[-B\,(1) + \frac{6}{5} B \left(\frac{5}{6} \right) \right] \left\langle\!\left\langle \mathbf{n} \left(\mathbf{n} \cdot \mathbf{q}_T \right) \right\rangle\!\right\rangle \right\} \tag{3.3}$$

$$\mathbf{F}_\omega = A \left\langle\!\left\langle \left[\mathbf{x} \times \boldsymbol{\omega}_p \right] \right\rangle\!\right\rangle - B\,(1) \left\langle\!\left\langle \mathbf{n} \left(\boldsymbol{\omega}_p \cdot \left[\mathbf{x} \times \mathbf{n} \right] \right) \right\rangle\!\right\rangle$$

The terms of the second equation of (3.2) are determined by the relationships

$$\mathbf{M}_\xi = A \left\langle\!\left\langle \mathbf{x} \times \left(\mathbf{U} - \boldsymbol{\xi}_p \right) \right\rangle\!\right\rangle + B\,(1) \left\langle\!\left\langle \left[\mathbf{x} \times \mathbf{n} \right] \left[\left(\mathbf{U} - \boldsymbol{\xi}_p \right) \cdot \mathbf{n} \right] \right\rangle\!\right\rangle$$

$$\mathbf{M}_T = \frac{1}{p} \left\{ \frac{A}{5} \left\langle\!\left\langle \mathbf{x} \times \mathbf{q}_T \right\rangle\!\right\rangle + \left[-B\,(1) + \frac{6}{5} B \left(\frac{5}{6} \right) \right] \left\langle\!\left\langle \left[\mathbf{x} \times \mathbf{n} \right] \left(\mathbf{n} \cdot \mathbf{q}_T \right) \right\rangle\!\right\rangle \right\} \tag{3.4}$$

$$\mathbf{M}_\omega = A \left\langle\!\left\langle \mathbf{x} \times \left[\mathbf{x} \times \boldsymbol{\omega}_p \right] \right\rangle\!\right\rangle - B\,(1) \left\langle\!\left\langle \left[\mathbf{x} \times \mathbf{n} \right] \left(\boldsymbol{\omega}_p \cdot \left[\mathbf{x} \times \mathbf{n} \right] \right) \right\rangle\!\right\rangle$$

The angular brackets $\langle\!\langle\rangle\!\rangle$ signify the integration over the surface of particle,

$$\left\langle\!\left\langle Z \right\rangle\!\right\rangle \equiv \int Z \, dS; \quad Z = \left(\mathbf{U} - \boldsymbol{\xi}_p \right), \mathbf{n} \left(\left(\mathbf{U} - \boldsymbol{\xi}_p \right) \cdot \mathbf{n} \right), \ \ldots \tag{3.5}$$

that is, for example, $\left\langle\!\left\langle \mathbf{U} - \boldsymbol{\xi}_p \right\rangle\!\right\rangle = \left(\mathbf{U} - \boldsymbol{\xi}_p \right) S$, where S is a surface area of a particle. The following symbols are used (λ is a coefficient of heat conductivity of gas):

$$A = 2\rho \left(\frac{h}{\pi} \right)^{1/2} \frac{\alpha}{4}, \quad B\,(l) = 2\rho \left(\frac{h}{\pi} \right)^{1/2} \left(1 + \frac{l\,\pi\sqrt{\tau} - 6}{8} \alpha \right), \quad l = 1, \ \frac{5}{6},$$

$$\mathbf{q}_T = -\lambda \nabla T, \quad p = \frac{\rho}{m} kT, \quad h = \frac{2kT}{m}, \quad \tau = \frac{T_p}{T}, \quad \varepsilon = \frac{m}{m_p} \tag{3.6}$$

After a series of similar but more complicated computations, the following equations for the diffusion coefficients in the spaces of translational and angular velocities are obtained:

$$\mathbf{D}_\xi = \frac{\varepsilon}{2m_p} \left\langle\left\langle a_0\mathbf{E} + b_0\mathbf{nn}\right\rangle\right\rangle \tag{3.7}$$

$$\mathbf{D}_\omega = \frac{\varepsilon}{2} m_p \Bigg\{ b_0 \left\langle\left\langle \left(\mathbf{I}^{-1} \cdot [\mathbf{x} \times \mathbf{n}]\right) \left(\mathbf{I}^{-1} \cdot [\mathbf{x} \times \mathbf{n}]\right)\right\rangle\right\rangle$$

$$+ a_0 \left\langle\left\langle (\mathbf{x} \cdot \mathbf{x}) \sum_{k=1}^3 \left(\mathbf{I}^{-1} \cdot \mathbf{e}_k\right) \left(\mathbf{I}^{-1} \cdot \mathbf{e}_k\right) - \left(\mathbf{I}^{-1} \cdot \mathbf{x}\right) \left(\mathbf{I}^{-1} \cdot \mathbf{x}\right)\right\rangle\right\rangle \Bigg\} \tag{3.8}$$

and for mixed diffusion coefficient,

$$\mathbf{D}_{\xi\omega} = \varepsilon \left(\sum_{k=1}^3 a_0 \left\langle\left\langle \mathbf{e}_k \left(\mathbf{I}^{-1} \cdot [\mathbf{x} \times \mathbf{e}_k]\right)\right\rangle\right\rangle + b_0 \left\langle\left\langle \mathbf{n} \left(\mathbf{I}^{-1} \cdot [\mathbf{x} \times \mathbf{n}]\right)\right\rangle\right\rangle \right) \tag{3.9}$$

The following symbols are used:

$$a_0 = \alpha\left(1 + \tau\right) \frac{h^{3/2}}{4\sqrt{\pi}}\rho, \quad b_0 = a_0 + \frac{h^{3/2}}{\sqrt{\pi}} \left[\frac{\alpha}{4}\pi\sqrt{\tau} + 2\left(1 - \alpha\right)\right]\rho \tag{3.10}$$

$\mathbf{e}_k$ $(k = 1, 2, 3)$ are unit vectors generating the right-hand system.

Let us consider the equilibrium case when $\mathbf{U} = 0, \nabla T = 0, \tau = 1$, and the distribution function of particles over velocities is to be determined by the equation

$$F_p\left(\boldsymbol{\xi}_p, \boldsymbol{\omega}_p\right) = F_p^{(0)} \sim \exp\left[-\frac{1}{2kT} \left(m_p\boldsymbol{\xi}_p \cdot \boldsymbol{\xi}_p + \boldsymbol{\omega}_p \cdot \mathbf{I} \cdot \boldsymbol{\omega}_p\right)\right] \tag{3.11}$$

Therefore, its derivatives are as follows:

$$\frac{\partial F_p}{\partial \boldsymbol{\xi}_p} = F_p^{(0)} \left(-\frac{m_p}{kT}\boldsymbol{\xi}_p\right), \quad \frac{\partial F_p^{(0)}}{\partial \boldsymbol{\omega}_p} = F_p^{(0)} \left(-\frac{\mathbf{I} \cdot \boldsymbol{\omega}}{kT}\right),$$

$$\frac{\partial^2 F_p^{(0)}}{\partial \boldsymbol{\xi}_p \partial \boldsymbol{\omega}_p} = F_p^{(0)} \frac{m_p}{(kT)^2} \left(\mathbf{I} \cdot \boldsymbol{\omega}_p\right) \boldsymbol{\xi}_p \tag{3.12}$$

where the symmetry of tensor of inertia $\mathbf{I}$ is taken into account.

Let us bring under the integral all these derivatives and all the coefficients that do not depend on the coordinates of particle surface and let us write operator (3.1) in the form

$$J = \left\langle\left\langle J_\xi + J_\omega + J_{\xi\omega}\right\rangle\right\rangle \tag{3.13}$$

where Eq. (3.5) is used. Let us prove that the expression under integral sign in Eq. (3.13), i.e., the sum $J_\xi + J_\omega + J_{\xi\omega}$, equals zero; therefore, the distribution (3.11) is valid.

With all of the above considered, operator J_ξ is defined through the formula

$$J_\xi = -\frac{\partial}{\partial \boldsymbol{\xi}_p} \cdot \left[\frac{\mathbf{F}_\xi}{m_p} + \frac{2}{h_p} \left(\mathbf{D}_\xi \cdot \boldsymbol{\xi}_p \right) \right] F_p^{(0)}, \quad h_p = \frac{2kT}{m_p} \tag{3.14}$$

where vector $\mathbf{F}_\xi$ is determined by the first equation of (3.3), and tensor $\mathbf{D}_\xi$ is determined by Eq. (3.7). The Eqs. (3.6), (3.10) are bound by the relationship

$$(A, \ B(1)) = \frac{1}{h} (a_0, \ b_0)$$

and the following equation is valid for the product of a vector by a dyad:

$$\boldsymbol{\xi}_p \cdot \mathbf{nn} = \mathbf{n} (\boldsymbol{\xi}_p \cdot \mathbf{n})$$

we obtain that the expression inside the square brackets in Eq. (3.14) equals zero since

$$\frac{2}{h_p} \left(\mathbf{D}_\xi \cdot \boldsymbol{\xi}_p \right) = \frac{1}{m_p} \left(A\boldsymbol{\xi}_p \cdot \mathbf{E} + B(1)\boldsymbol{\xi}_p \cdot \mathbf{nn} \right) = \frac{1}{m_p} \left[A\boldsymbol{\xi}_p + B(1)\mathbf{n}(\boldsymbol{\xi}_p \cdot \mathbf{n}) \right] = -\frac{\mathbf{F}_\xi}{m_p},$$

where $\mathbf{E}$ is a unit tensor. Taking into account the third formula of Eq. (3.4) and Eq. (3.8) for J_ω, we have

$$J_\omega = -\frac{\partial}{\partial \boldsymbol{\omega}_p} \cdot \left[\mathbf{M}_\omega \cdot \mathbf{I}^{-1} + \mathbf{D}_\omega \cdot (\mathbf{I} \cdot \boldsymbol{\omega}_p) \frac{1}{kT} \right] F_p^{(0)} \tag{3.15}$$

Obtained by analogy is

$$\mathbf{D}_\omega \cdot (\mathbf{I} \cdot \boldsymbol{\omega}_p) = kT \left[B(1) \left\langle \left\langle \left(\mathbf{I}^{-1} \cdot [\mathbf{x} \times \mathbf{n}] \right) (\boldsymbol{\omega}_p \cdot [\mathbf{x} \times \mathbf{n}]) \right\rangle \right\rangle \right.$$
$$\left. - A \left\langle \left\langle \left(\mathbf{I}^{-1} \cdot \mathbf{x} \right) (\mathbf{x} \cdot \boldsymbol{\omega}_p) - (\mathbf{x} \cdot \mathbf{x}) \left(\mathbf{I}^{-1} \cdot \boldsymbol{\omega}_p \right) \right\rangle \right\rangle \right] = - \left(\mathbf{M}_\omega \cdot \mathbf{I}^{-1} \right) kT$$

Therefore, the expression inside the square brackets equals in Eq. (3.15) zero. Finally, applying the third equation of (3.3), the first one of (3.4), and Eq. (3.9), we find the equation for $J_{\xi\omega}$ as

$$J_{\xi\omega} = \frac{F_p^{(0)}}{kT} \left\{ \mathbf{F}_\omega \cdot \boldsymbol{\xi}_p + \left(\mathbf{M}_\xi \cdot \mathbf{I}^{-1} \right) \cdot (\mathbf{I} \cdot \boldsymbol{\omega}_p) + \frac{2}{h_p} \mathbf{D}_{\xi\omega} : \left[(\mathbf{I} \cdot \boldsymbol{\omega}_p) \, \boldsymbol{\xi}_p \right] \right\} \tag{3.16}$$

The relation $\left(\mathbf{a} \cdot \mathbf{T}^{-1} \right) \cdot (\mathbf{T} \cdot \mathbf{b}) = \mathbf{a} \cdot \mathbf{b}$ is valid for every two vectors $\mathbf{a}$, $\mathbf{b}$ and for symmetric tensor $\mathbf{T}$. Besides this, tensor $\mathbf{D}_{\xi\omega}$ is a dyad, and the relation $\mathbf{ab} : \mathbf{cd} = (\mathbf{a} \cdot \mathbf{d})(\mathbf{b} \cdot \mathbf{c})$ is valid for the double product of dyads. Therefore, we find that the sum of two first terms inside the square brackets in Eq. (3.16) is equal to the third one with a minus sign,

$$\mathbf{F}_\omega \cdot \boldsymbol{\xi}_p + \left(\mathbf{M}_\xi \cdot \mathbf{I}^{-1} \right) \cdot (\mathbf{I} \cdot \boldsymbol{\omega}_p) = 2 \left(\mathbf{F}_\omega \cdot \boldsymbol{\xi}_p \right) = -\frac{2}{h_p} \mathbf{D}_{\xi\omega} : \left[(\mathbf{I} \cdot \boldsymbol{\omega}_p) \, \boldsymbol{\xi}_p \right]$$

Therefore, $J_{\xi\omega} = 0$.

Thus, the expression under the integral sign in (3.13) and, therefore, operator J are equal to zero, i.e.,

$$J_\xi + J_\omega + J_{\xi\omega} = 0 \;\Rightarrow\; J = 0$$

and equilibrium distribution (3.11) is valid, which was to be proved.

4. PARTICLES AS BODIES OF REVOLUTION

Let consider the particles as bodies of revolution, with the axis of symmetry set by unit vector **u**. It is possible in this case to write the coefficients of operator (3.1) through the expressions determined only by the shape of particle. During the integration with respect to **g** and **g**$'$, the technique described in Refs. [12, 15, 16] is applied.

The Fokker-Planck operator (3.1) now takes the following form:

$$J = \frac{\partial}{\partial \boldsymbol{\xi}_p} \cdot \left\{ \left[\boldsymbol{\gamma}_\xi \cdot (\boldsymbol{\xi}_p - \mathbf{U}) + \boldsymbol{\theta} \cdot \nabla T - \frac{\mathbf{F}_\omega}{m_p} \right] F_p + \mathbf{D}_\xi \cdot \frac{\partial F_p}{\partial \boldsymbol{\xi}_p} \right\} + \frac{\partial}{\partial \boldsymbol{\omega}_p}$$

$$\cdot \left\{ \left[\boldsymbol{\gamma}_\omega \cdot \boldsymbol{\omega}_p - (\mathbf{M}_\xi + \mathbf{M}_T) \cdot \mathbf{I}^{-1} \right] F_p + \mathbf{D}_\omega \cdot \frac{\partial F_p}{\partial \boldsymbol{\omega}_p} \right\} + \mathbf{D}_{\xi\omega} : \frac{\partial^2 F_p}{\partial \boldsymbol{\xi}_p \partial \boldsymbol{\omega}_p} \qquad (4.1)$$

Tensors of second rank $\boldsymbol{\gamma}_\xi, \boldsymbol{\theta}, \mathbf{D}_\xi, \mathbf{D}_\omega$ are provided by the following experessions:

$$\boldsymbol{\gamma}_\xi = \beta_\| \, \mathbf{uu} + \beta_\perp \, (\mathbf{E} - \mathbf{uu}), \quad \boldsymbol{\theta} = \varphi_\| \, \mathbf{uu} + \varphi_\perp \, (\mathbf{E} - \mathbf{uu}) \qquad (4.2)$$

$$\begin{pmatrix} \beta_\| \\ \beta_\perp \end{pmatrix} = \varphi \left[\chi \begin{pmatrix} 2F_2 \\ F_1 - F_2 \end{pmatrix} + \frac{\alpha}{2} F_1 \begin{pmatrix} 1 \\ 1 \end{pmatrix} \right], \quad \varphi = \frac{\rho}{m_p} \left(\frac{h}{\pi} \right)^{1/2}, \qquad (4.3)$$

$$\chi = 1 + \left(\pi \sqrt{\tau} - 6 \right) \frac{\alpha}{8}$$

Used in Eqs. (2.10) and (4.3) and later are the equations of the form of columns. Meanwhile, for example, $\beta_\perp = \varphi \left[\chi \, (F_1 - F_2) + (1/2) \alpha \, F_1 \right]$. The expressions for $\varphi_\|, \varphi_\perp$ are defined from Eq. (4.3) for $\beta_\|, \beta_\perp$, respectively, by the following substitutions: $\varphi \to (\lambda \varphi / 5p), \chi \to 1 - (3/4)\alpha$.

The following equations are valid for other tensors:

$$\boldsymbol{\gamma}_\omega = \mathbf{I}^{-1} \cdot \left(\vartheta_\| \, \mathbf{uu} + \vartheta_\perp \, (\mathbf{E} - \mathbf{uu}) \right), \quad \mathbf{D}_\xi = \varsigma \left[\mathbf{E} + \phi \, (N \, \mathbf{E} + (1 - 3N) \, \mathbf{uu}) \right] F_1,$$

$$\begin{pmatrix} \vartheta_\| \\ \vartheta_\perp \end{pmatrix} = \varphi \, m_p \left[\chi \begin{pmatrix} 2H_2 \\ H_1 - H_2 \end{pmatrix} + \frac{\alpha}{2} \begin{pmatrix} G_1 - G_2 \\ \frac{1}{2} (G_1 + G_2) \end{pmatrix} \right], \qquad (4.4)$$

$$\varsigma = \frac{1}{8} \varepsilon \, \alpha \, (1 + \tau) \, h \, \varphi$$

$$\mathbf{D}_\omega = \frac{\varsigma}{2}\, m_p^2 \Big\{ \left(\mathbf{I}^{-1} \cdot \mathbf{I}^{-1} \right) \left[\phi \left(H_1 - H_2 \right) + G_1 + G_2 \right]$$

$$+ \left(\mathbf{I}^{-1} \cdot \mathbf{u} \right)\left(\mathbf{I}^{-1} \cdot \mathbf{u} \right)\left[\phi(3H_2 - H_1) + G_1 - 3G_2 \right] \Big\}, \quad \phi = 1 + \frac{1}{1+\tau}\left[\pi\sqrt{\tau} + \frac{8}{\alpha}(1-\alpha) \right] \quad (4.5)$$

The expressions for factors $\varphi, \chi, \varsigma, \phi$ are set in Eqs. (4.3)–(4.5), $\mathbf{I}^{-1}$ is a tensor inverse to the tensor of inertia in the moving frame of reference, $\mathbf{E}$ is a unit tensor, and $\mathbf{uu}$ is a dyad. The coefficients that are determined only through the shape of a particle are given by the following equations [using bracket operators (3.5)]:

$$F_1 = \langle\langle 1 \rangle\rangle, \quad F_2 = \left\langle\left\langle (\mathbf{n}\cdot\mathbf{u})^2 \right\rangle\right\rangle, \quad N = \frac{1}{2}\left(1 - \frac{F_2}{F_1} \right), \quad G_1 = \left\langle\left\langle \mathbf{x}^2 \right\rangle\right\rangle,$$

$$G_2 = \left\langle\left\langle (\mathbf{x}\cdot\mathbf{u})^2 \right\rangle\right\rangle, \quad H_1 = \left\langle\left\langle [\mathbf{x}\times\mathbf{n}]^2 \right\rangle\right\rangle, \quad H_2 = \left\langle\left\langle ([\mathbf{x}\times\mathbf{n}]\cdot\mathbf{u})^2 \right\rangle\right\rangle \quad (4.6)$$

The integral of dyads over the surface appearing during the calculation of considered tensors are expressed in terms of them (again, $\mathbf{n}$ is a unit vector of the external normal):

$$\left\langle\left\langle \begin{matrix} \mathbf{nn} \\ \mathbf{xx} \\ [\mathbf{x}\times\mathbf{n}][\mathbf{x}\times\mathbf{n}] \end{matrix} \right\rangle\right\rangle = \frac{1}{2}\begin{pmatrix} F_1 \\ G_1 \\ H_1 \end{pmatrix}(\mathbf{E} - \mathbf{uu}) + \frac{3}{2}\begin{pmatrix} F_2 \\ G_2 \\ H_2 \end{pmatrix}\left(\mathbf{uu} - \frac{1}{3}\mathbf{E} \right)$$

The calculation of these integrals is described in more details in Ref. [12], where the particles with longitudinal symmetry (i.e., having a symmetry plane perpendicular to the axis of symmetry) are considered.

Other terms of Eq. (4.1) appear in the case of bodies without longitudinal symmetry. The following relations for the force resulted from the rotation, acting on a particle, are valid:

$$\mathbf{F}_\omega = Q\left[\boldsymbol{\omega}_p \times \mathbf{u} \right], \quad Q = A\,\mu_2 + B\,(1)\,\upsilon \quad (4.7)$$

The following expressions for the torques resulted from translational motion and from temperature gradient are valid:

$$\mathbf{M}_\xi = A\,\mu_2\left[\mathbf{u}\times\left(\mathbf{U} - \boldsymbol{\xi}_p \right) \right] + B\,(1)\,\upsilon\left\{ \mathbf{j}\left[\left(\mathbf{U} - \boldsymbol{\xi}_p \right)\cdot\mathbf{i} \right] - \mathbf{i}\left[\left(\mathbf{U} - \boldsymbol{\xi}_p \right)\cdot\mathbf{j} \right] \right\} \quad (4.8)$$

$$\mathbf{M}_T = -\frac{\lambda}{p}\left\{ \frac{A}{5}\mu_2[\mathbf{u}\times\nabla T] + \upsilon\left[-B\,(1) + \frac{6}{5}B\left(\frac{5}{6} \right) \right]\left[\mathbf{j}(\nabla T\cdot\mathbf{i}) - \mathbf{i}(\nabla T\cdot\mathbf{j}) \right] \right\} \quad (4.9)$$

The appearance of last term from Eq. (4.1) with the mixed derivative is importance. The following value is called the mixed diffusion coefficient:

$$\mathbf{D}_{\xi\omega} = \varepsilon\left\{ \mu_2 a_0 \sum_{k=1}^{3} \mathbf{e}_k\left(\mathbf{I}^{-1}\cdot[\mathbf{u}\times\mathbf{e}_k] \right) + b_0\upsilon\left[\mathbf{i}\left(\mathbf{I}^{-1}\cdot[\mathbf{u}\times\mathbf{i}] \right) + \mathbf{j}\left(\mathbf{I}^{-1}\cdot[\mathbf{u}\times\mathbf{j}] \right) \right] \right\} \quad (4.10)$$

The formal cause of the appearance of new terms in the collision operator is the fact that the integrals over the surface of particle

$$\boldsymbol{\alpha}_1 = \langle\langle \mathbf{x} \rangle\rangle ; \quad \boldsymbol{\alpha}_2 = \langle\langle \mathbf{nnx} \rangle\rangle ; \quad \mathbf{nnx} = (n_\nu n_\mu x_\lambda) ; \quad \nu, \ \mu, \ \lambda = 1, \ 2, \ 3,$$

containing the third component of $\mathbf{x}$ vector, i.e., its symmetry axis component $x_3, n_1^2 x_3,$ $n_2^2 x_3, n_3^2 x_3, n_1 n_3 x_3, \ n_2 n_3 x_3$ are not equal to zero in contrast to the case described in Ref. [12]. It may be shown that integrals $\boldsymbol{\alpha}_1, \boldsymbol{\alpha}_2$ have the following form:

$$\boldsymbol{\alpha}_1 = \mu_2 \mathbf{u}, \quad \boldsymbol{\alpha}_2 = \mu_1 \mathbf{uuu} + \frac{1}{2}(\mu_2 - \mu_1)(\mathbf{ii} + \mathbf{jj})\,\mathbf{u} + \frac{1}{2}\mu_3(\mathbf{u}[\mathbf{ii} + \mathbf{jj}] + \mathbf{iui} + \mathbf{juj}),$$

$$\mu_1 = \left\langle\!\!\left\langle (\mathbf{x}\cdot\mathbf{u})(\mathbf{n}\cdot\mathbf{u})^2 \right\rangle\!\!\right\rangle, \quad \mu_2 = \langle\langle \mathbf{x}\cdot\mathbf{u} \rangle\rangle, \quad \mu_3 = \langle\langle [\mathbf{x}\times\mathbf{u}][\mathbf{n}\times\mathbf{u}](\mathbf{n}\cdot\mathbf{u})\rangle\rangle \quad (4.11)$$

The unit vector in the line of symmetry axis of a particle forms the mutually perpendicular triple with vectors $\mathbf{i}$ and $\mathbf{j}$, the unit vector $\mathbf{E}$ being equal to $\mathbf{E} = \mathbf{ii} + \mathbf{jj} + \mathbf{uu}$. Using Eq. (4.11) and a known expression for the mixed product, we find

$$\langle\langle \mathbf{n}\,(\boldsymbol{\omega}_p\cdot[\mathbf{x}\times\mathbf{n}])\rangle\rangle = \upsilon\left\{\mathbf{i}\,(\mathbf{i}\cdot[\boldsymbol{\omega}_p\times\mathbf{u}]) + \mathbf{j}\,(\mathbf{j}\cdot[\boldsymbol{\omega}_p\times\mathbf{u}])\right\} = \upsilon\,[\boldsymbol{\omega}_p\times\mathbf{u}],$$

$$\langle\langle (\boldsymbol{\xi}_p\cdot\mathbf{n})[\mathbf{x}\times\mathbf{n}]\rangle\rangle = \upsilon\left[\mathbf{j}\,(\boldsymbol{\xi}_p\cdot\mathbf{i}) - \mathbf{i}\,(\boldsymbol{\xi}_p\cdot\mathbf{j})\right], \quad \upsilon = \frac{1}{2}(\mu_2 - \mu_1 - \mu_3) \quad (4.12)$$

Expressions (4.11) and (4.12) are used for the calculation of Eqs. (4.7)–(4.10).

5. SPECIAL CASES

In order to obtain simple qualitative assessments, the special "degenerated" cases of the motion of Brownian particles are considered [2]. It is assumed hereafter that vector $\mathbf{u}$, related to the symmetry axis of a particle, is directed along the z-axis of a fixed frame of reference (the fixation of this axis is realized, for example, by external forces [2]), and the velocity of the gas $\mathbf{U} = 0$. In both cases, the integral $H_2 = 0$ [see Eq. (4.6)].

The first case is considered earlier [12]. The particles possess a longitudinal symmetry, i.e., have the symmetry plane perpendicular to the symmetry axis that is parallel to the vectors $\boldsymbol{\xi}_p = \xi_p \mathbf{u}, \boldsymbol{\omega}_p = \omega_p \mathbf{u}, \nabla T = (dT/dz)\,\mathbf{u}$. The Fokker-Planck operator takes a much simpler form,

$$J = \frac{\partial}{\partial\xi_p}\left\{\left[\gamma_\xi\,\xi_p + \theta\frac{dT}{dz}\right]F_p + D_\xi\frac{\partial F_p}{\partial\xi_p}\right\} + \frac{\partial}{\partial\omega_p}\left\{\gamma_\omega\omega_p F_p + D_\omega\frac{\partial F_p}{\partial\omega_p}\right\} \quad (5.1)$$

Coefficients $\gamma_\xi, \gamma_\omega, \theta, D_\xi, D_\omega$ are scalars, and the expressions for them result from Eqs. (4.2)–(4.5) as

$$\gamma_\xi = \beta_\|, \quad \gamma_\omega = \frac{1}{\Gamma_{uu}}\vartheta_\|, \quad \theta = \varphi_\|, \quad D_\xi = \varsigma\,[F_1 + \phi F_2], \quad (5.2)$$

$$D_\omega = \frac{\varsigma}{\Gamma_{uu}^2}\, m_p^2 \left(G_1 - G_2\right)$$

where Γ_{uu} is a moment of inertia with respect to the axis of a particle. These coefficients are written using the integral values (4.6). The explicit expressions for the last ones are obtained in Ref. [12] for circular cylinders of finite length, spherocylinders, and spheroids. Using these expressions, the analysis of the influence of particle nonsymmetry on the relations between the diffusion coefficients in velocity spaces and the coefficients of forces and of momentums acting on a particle in thermal nonequilibrium is fulfilled.

Let us demonstrate these explicit expressions. For the circular cylinder with radius R_0 and length $h_* R_0$, there are

$$\begin{pmatrix}\gamma_\xi \\ \theta\end{pmatrix} = Y\varphi\begin{pmatrix}\sigma_1 + \dfrac{\pi}{4}\alpha\sqrt{\tau} \\ \dfrac{\lambda}{5\,p}\,\sigma_1\end{pmatrix}, \quad \begin{pmatrix}\gamma_\omega \\ D_\omega\end{pmatrix} = Y\sigma_2\begin{pmatrix}\dfrac{\alpha}{2}\,\varphi \\ \dfrac{2\,\varsigma}{R_0^2}\end{pmatrix}, \quad \begin{pmatrix}\sigma_1 \\ \sigma_2\end{pmatrix} = \begin{pmatrix}2 + \alpha\left(\dfrac{h_*}{2} - 1\right) \\ 1 + 2\,h_* + \dfrac{h_*^3}{6}\end{pmatrix},$$

$$D_\xi = Y\varsigma\,(1 + h_*)\left\{2 + h_* + \frac{1 + h_*}{1 + \tau}\left[\pi\sqrt{\tau} + \frac{8}{\alpha}\,(1 - \alpha)\right]\right\}, \quad Y = 2\pi R_0^2$$

At $h_* = 0$, we obtain the expressions for a circular disk. For a spherocylinder consisting of a circular cylinder of radius R_0, of length $h_* R_0$, and of two hemispheres at the ends, we find

$$\begin{pmatrix}\gamma_\xi \\ \theta\end{pmatrix} = Y\varphi\begin{pmatrix}\sigma_3 + \dfrac{\pi}{6}\alpha\sqrt{\tau} \\ \dfrac{\lambda}{5\,p}\,\sigma_3\end{pmatrix}, \quad \begin{pmatrix}\gamma_\omega \\ D_\omega\end{pmatrix} = \frac{m_p}{\Gamma}\pi R_0^4\left(\frac{4}{3} + h_*\right)\begin{pmatrix}\alpha\,\varphi \\ \dfrac{2\,\varsigma}{\Gamma}\,m_p\end{pmatrix}, \quad Y = 2\pi R_0^2,$$

$$D_\xi = \frac{2}{3}Y\varsigma\left\{4 + \frac{3}{2}h_* + \frac{1}{1 + \tau}\left[\pi\sqrt{\tau} + \frac{8}{\alpha}(1 - \alpha)\right]\right\}, \quad \begin{pmatrix}\sigma_3 \\ \Gamma\end{pmatrix} = \begin{pmatrix}\dfrac{4}{3} + \alpha\dfrac{h_*}{2} \\ m_p R_0^2\dfrac{16 + 15h_*}{10\;\;\;4 + 3h_*}\end{pmatrix}$$

Coefficients φ, ς are determined by the last equations of (4.3) and (4.4). The corresponding relations for a sphere result from these at $h_* = 0$

$$\gamma_\xi = \frac{8}{3}\rho\, R_0^2\sqrt{\pi h}\left(1 + \alpha\frac{\pi}{8}\sqrt{\tau}\right)m_p^{-1}, \quad \theta = \frac{16}{15 m_p}\sqrt{\frac{\pi}{h}}R_0^2\lambda, \quad \gamma_\omega = \frac{4}{3}\rho\, R_0^4\sqrt{\pi\, h}\,\alpha\,\Gamma^{-1},$$

$$D_\xi = \frac{kT}{m_p}\gamma_\xi\,(1 + \delta_\xi), \quad D_\omega = \frac{kT}{\Gamma}\gamma_\omega\,(1 + \delta_\omega),$$

$$\delta_\xi = \alpha\,\delta_\omega\left(1 + \alpha\frac{\pi}{8}\sqrt{\tau}\right)^{-1}, \quad \delta_\omega = \frac{\tau - 1}{2}, \quad \Gamma = \frac{2}{5}m_p R_0^2, \quad \tau = \frac{T_p}{T}$$

Here, λ is the heat-conductivity coefficient of a gas.

The equations for the oblate spheroid with semiaxes a and b (axis $a < b$, the rotation is around the small axis [17]) are the following:

$$\begin{pmatrix} \gamma_\xi \\ \theta \\ D_\xi \end{pmatrix} = 4\pi\varphi\left(a^2 + b^2\sigma\right) \begin{pmatrix} \chi d_1 + \dfrac{\alpha}{4} \\[2mm] \dfrac{\lambda}{5p}\left[d_1\left(1 - \dfrac{3}{4}\alpha\right) + \dfrac{\alpha}{4}\right] \\[2mm] \dfrac{\varsigma}{2\varphi}\left(1 + \phi\, d_1\right) \end{pmatrix}, \quad \begin{pmatrix} \gamma_\omega \\ D_\omega \end{pmatrix} = \frac{m_p\pi d_2}{4\Gamma}\begin{pmatrix} \alpha\varphi \\[1mm] 2m_p\dfrac{\varsigma}{\Gamma} \end{pmatrix},$$

$$d_1 = 1 - \frac{y^2\left[\left(1 + \kappa^2\right)\sigma - 1\right]}{\kappa^2\left(y^2\sigma + 1\right)}, \quad \sigma = \frac{1}{2\kappa}\ln\frac{1+\kappa}{1-\kappa}, \quad y^2 = 1 - \kappa^2, \quad \Gamma = \frac{2}{5}m_p a^2,$$

$$d_2 = a^4\left\{3 - \kappa^2 - y^2\sigma\left(\kappa^2 - 5\right) - \frac{1}{\kappa^2}\left[1 - \kappa^4 - \left(1 - \kappa^2\right)^3\sigma\right]\right\}, \quad \kappa^2 = 1 - \frac{b^2}{a^2}$$

The similar expressions for the prolate spheroid with semiaxes a and b (axis $a > b$, the rotation is around the big axis) are obtained from the reduced equations for the oblate spheroid by the following substitutions. In the equations for the column of elements $\gamma_\xi, \theta, D_\xi$. One needs to complete the substitutions

$$a^2 + b^2\sigma \to a\left(a + b\sigma\right), \quad d_1 \to d_3 \equiv 1 - \frac{y - \left(1 - 2\kappa^2\right)\sigma}{\kappa^2\left(y + \sigma\right)}$$

and in the formulas for the column of elements γ_ω, D_ω, the substitutions are

$$d_2 \to d_4 \equiv b^4 y\left\{y\left(3 - 2\kappa^2\right) + \sigma\left(5 - 4\kappa^2\right) - \frac{1}{\kappa^2}\left[y\left(2\kappa^2 - 1\right) + \sigma\right]\right\}$$

Made in Ref. [12] for this case is an error: in the equation for G_1 the coefficient $(3 - \kappa^2)$ is to be substituted by $(3 - 2\kappa^2)$. As in Ref. [12], there are the following values in all the equation for the prolate spheroid:

$$\sigma = \frac{1}{\kappa}\arcsin\kappa, \quad y = \sqrt{1 - \kappa^2}, \quad \kappa^2 = 1 - \frac{a^2}{b^2}, \quad \Gamma = \frac{2}{5}m_p a^2$$

Let us consider the second special case. The particles do not possess longitudinal symmetry. Vectrors $\xi_p = \xi_p \mathbf{i}$, $\nabla T = (dT/dx)\,\mathbf{i}$, $\omega_p = \omega_p \mathbf{j}$ are perpendicular to the symmetry axis of a particle. Symbol Γ_{xx} signifies the moment of inertia of a particle along the axis perpendicular to $\mathbf{u}$. Therefore, Eqs. (4.7)–(4.9) take the form

$$\mathbf{F}_\omega = Q\,\omega_p\mathbf{i}, \quad \mathbf{M}_\xi = -Q\,\xi_p\mathbf{j} \tag{5.3}$$

$$\mathbf{M}_T = -\frac{\lambda}{p}V\frac{dT}{dx}\mathbf{j}, \quad V = \frac{A}{5}\mu_2 + \left[-B\left(1\right) + \frac{6}{5}B\left(\frac{5}{6}\right)\right]\upsilon \tag{5.4}$$

$$\mathbf{D}_{\xi\omega} : \frac{\partial^2 F_p}{\partial \xi_p \partial \omega_p} = D_{\xi\omega} \frac{\partial^2 F_p}{\partial \xi_p \partial \omega_p}, \quad D_{\xi\omega} = \frac{\varepsilon}{\Gamma_{xx}} \left(\mu_2 \, a_0 + \upsilon \, b_0 \right) \tag{5.5}$$

Instead of Eq. (5.1), using Eqs. (5.3)–(5.5), we obtain the following equation for the operator of collisions:

$$J = \frac{\partial}{\partial \xi_p} \left\{ \left[\gamma_\xi \xi_p + \theta \frac{dT}{dx} - \frac{Q}{m_p} \, \omega_p \right] F_p + D_\xi \frac{\partial F_p}{\partial \xi_p} \right\}$$
$$+ \frac{\partial}{\partial \omega_p} \left\{ \left[\gamma_\omega \omega_p + \frac{1}{\Gamma_{xx}} \left(Q \xi_p + \frac{\lambda}{p} V \frac{dT}{dx} \right) \right] F_p + D_\omega \frac{\partial F_p}{\partial \omega_p} \right\} + D_{\xi\omega} \frac{\partial^2 F_p}{\partial \xi_p \partial \omega_p} \tag{5.6}$$

Let us remember that the radius vector $\mathbf{x} = R\mathbf{e}$ of an arbitrary point of the particle surface in a moving frame of reference presented earlier is measured from the center of inertia. In the first case, it coincides with the symmetry center, which is absent here. This fact complicates the problem of the calculation of the coefficients in Eq. (5.6). These coefficients are expressed through the integral values (4.6) and (4.11).

The following equations for these values are obtained for the circular cone of radius R_0, height $h_* R_0$, and inertia center located at a distance $(1/4)h_* R_0$ from the base:

$$F_1 = F_2 l_* = \pi R_0^2 (1 + l_*), \quad N = \frac{1}{2} \left(1 - \frac{1}{l_*} \right), \quad H_1 = \frac{c}{2} \left[1 + \frac{h_*^4 + 8}{8 \, l_*} \right], \quad l_* = \sqrt{1 + h_*^2},$$

$$G_1 = \left(1 + \frac{8}{h_*^2} \right) G_2, \quad G_2 = \frac{c}{16} h_*^2 (1 + l_*), \quad \mu_1 = \kappa \left(-1 + \frac{1}{3 \, l_*} \right), \quad c = \pi R_0^4, \tag{5.7}$$

$$\mu_2 = \kappa \left(-1 + \frac{l_*}{3} \right), \quad \mu_3 = \frac{8}{3} \frac{\kappa}{l_*}, \quad \kappa = \frac{h_* \pi R_0^3}{4}, \quad \Gamma_{xx} = \frac{3}{20} m_p R_0^2 \left(1 + \frac{1}{4} h_*^2 \right)$$

This is similar for the semisphere of radius R_0 and inertia center located at a distance $(3/8)R_0$ from the base,

$$F_1 = 3\pi R_0^2, \quad F_2 = \frac{5}{3} \pi R_0^2, \quad N = \frac{2}{9}, \quad H_1 = \frac{11}{16} c, \quad G_1 = \frac{139}{64} c,$$
$$G_2 = \frac{65}{192} c, \quad c = \pi R_0^4, \quad \mu_1 = \mu_2 = -\frac{1}{4} \mu_3 = -\frac{1}{8} \pi R_0^3, \quad \Gamma_{xx} = \frac{83}{320} m_p R_0^2 \tag{5.8}$$

As in the case of a cone, the contribution of the base is taken into account (the integration is fulfilled over the whole surface of particle). Equations (5.2) are valid for factors $\gamma_\xi, \theta, D_\xi$, and we have the following relations for factors γ_ω, D_ω:

$$\gamma_\omega = \frac{\varphi}{\Gamma_{xx}} m_p \left\{ \chi H_1 + \frac{\alpha}{4} (G_1 + G_2) \right\}, \quad D_\omega = \frac{\varsigma}{2} \left(\frac{m_p}{\Gamma_{xx}} \right)^2 (\phi H_1 + G_1 + G_2)$$

Taking into account the relationships of the last section and Eqs. (5.7) and (5.8) for the coefficients in Eqs. (5.3)–(5.5), we find

$$Q = Q_0 \left[\alpha s_0 + \left(1 + \frac{\pi\sqrt{\tau} - 6}{8}\alpha \right) s_1 \right], \quad V = \frac{1}{5}Q_0 \left[\alpha s_0 + \left(1 - \frac{3}{4}\alpha \right) s_1 \right]$$

$$D_{\xi\omega} = \frac{h\,\varepsilon}{2\,\Gamma_{xx}}Q_0 \left\{ \alpha\,(1+\tau)\,s_0 + \left[\frac{\alpha}{4}\,(1+\tau) + \frac{\alpha}{4}\pi\sqrt{\tau} + 2\,(1-\alpha) \right] s_1 \right\}$$

where for the cone

$$Q_0 = \rho\,\kappa \left(\frac{h}{\pi} \right)^{1/2}, \quad s_0 = \frac{1}{2}\left(\frac{l_*}{3} - 1 \right), \quad s_1 = \frac{l_*}{3} - \frac{3}{l_*}$$

And for the hemisphere

$$Q_0 = -\frac{\rho}{2}\,(\pi h)^{1/2}\,R_0^3, \quad s_0 = \frac{1}{8}, \quad s_1 = 1$$

Thus, for longitudinally unsymmetrical bodies of revolution, the mixed diffusion coefficient $D_{\xi\omega}$ differs from zero, and the Fokker-Planck operator contains the second derivative $\partial^2 F_p / \partial \xi_p \partial \omega_p$. The gas temperature gradient results not only in thermospherical force, but also in torque $\mathbf{M}_T$ [the first equation of (5.4)].

6. CONCLUSIONS

Presented above is not only a more general and comprehensive kinetic equation derivation than the previous one [10–12], but also the summary of the explicit expressions for the coefficients of the collision operator obtained here and in previous papers [10–12] and the results from Ref. [12] are transformed into a more convenient form. Using these expressions, one can analyze the influence on the coefficients of the thermal nonequilibrium parameter τ, of the accommodation parameter α, and of the particle shape similar to Refs. [11, 12]. Certainly, it is necessary to investigate the importance of the technique and of the present results as well as of previous ones [8–12] for Brownian motion theory, for molecular-kinetic theory, and for gas suspensions dynamics.

Thereby, let us underline the following. At the accepted technique of derivation of the kinetic equation of the Boltzmann type, and then, of the Fokker-Planck operator, a considerable number of assumptions are made. However, the important necessary conditions of its validity hold true, namely, the operator vanishes on the equilibrium distribution function at the equilibrium conditions, at $\tau = 1$ the known expressions [10, 11] result from it. Consideration of the thermal nonequilibrium at $\tau \neq 1$ demonstrates the capabilities of this theory and provides additional opportunities for experimental and theoretical analysis of this technique applicability and of kinetic equations of the Boltzmann type in general.

ACKNOWLEDGMENT

REFERENCES

1. Klimontovitch, Yu. L., *Statistical Physics*, Nauka, Moscow, 1982.

2. Kuni, F. M., *Statistical Physics and Thermodynamics*, Moscow, Nauka, 1981.

3. Nigmatulin, R. I., *Dynamics of Multiphase Media*, Moscow, Nauka, 1987.

4. Pirumov, U. G. and Roslyakov, G. S., *Gas Dynamics of Nozzles*, Moscow, Nauka, 1990.

5. Varaksin, A. U., *Turbulent Gas Flow with Solid Particles*, Moscow, Fizmatlit, 2003.

6. Tsibarov, V. A., *Kinetic Method in the Theory of Gas Suspensions*, St. Petersburg, SPbGU Publ., 1997.

7. Rudyak, V. A., *Statistical Aerohydrodynamics of Homogeneous and Heterogeneous Media*, Vol. 1, Kinetic Theory, NGASU Publ., Novosibirsk, 2004.

8. Montgomery, D., Brownian motion from Boltzmann's equation, *Phys. Fluids*, vol. 14, no. 10, pp. 2088–2090, 1971.

9. Fernandez de la Mora, J. and Mercer, J. M., Modified Fokker–Plank equation for the motion of Brownian particles in a nonuniform gas, *Phys. Rev. A*, vol. 26, no. 4, pp. 2178–2186, 1982.

10. Boris, A. Yu. and Galkin, V. S., Kinetic description of Brownian motion of heated particles in rarefied gas, *Izv. AN USSR, MZhG.*, no. 2, pp. 157–161, 1986.

11. Galkin, V. S. and Rusakov, S. V., Fokker–Planck kinetic equation for Brownian free-molecular thermally nonequilibrium particles in nonhomogeneous gas, *Izv. Ross. Akad. Nauk, MZhG.*, no. 2, pp. 204–208, 2007.

12. Galkin, V. S. and Rusakov, S. V., Fokker–Planck operator for Brownian free-molecular thermally nonequilibrium nonspherical particles, *Izv. Ross. Akad. Nauk, MZhG.*, no. 1, pp. 180–188, 2008.

13. Happel, J. and Brenner, H., *Low Reynolds Number Hydrodynamics*, Prentice-Hall, Englewood Cliffs, NJ, 1965.

14. Curtiss, C. F., Kinetic theory of nonspherical molecules, *J. Chem. Phys.*, vol. 24. no. 2, pp. 225–241, 1956.

15. Vestner, H. and Halbritter, J., Torque on a small particle in a nongomogeneous monatomic gas, *Z. Naturforsch.*, vol. 36a, no 6, pp. 559–567, 1981.

16. Halbritter, J., Torque on a rotating ellipsoid in a rarefied gas, *Z. Naturforsch.* vol. 29a. no. 12, pp. 1717–1722, 1974.

17. Korn, G. A. and Korn, T. M., *Mathematical Handbook*, McGraw-Hill Book Company, New York, 1968.

EXPERIMENTAL STUDY OF THE JET FLOW CONTROL IN A VEHICLE AFTBODY

B. L. Zhirnikov, O. K. Kudin, & Yu. N. Nesterov[*]

Central Aerohydrodynamic Institute (TsAGI) 1, Zhukovsky str., Zhukovsky, 140180, Moscow region, Russia

[*]Address all correspondence to Yu. N. Nesterov E-mail: kash@dept.aerocentr.msk.su

Presented are the results of experimental investigation of the jet flow gas dynamic effect in order to control the thrust vector and to reduce the drag of the vehicle. The vehicle has a flat nozzle with an external expansion wall, being the part of the fuselage. The gas dynamic control method, based on the injection of additional air through the perforation in the expansion wall, is considered. The conclusions about the efficiency of gas dynamic control by means of various methods of additional air injection are drawn according to the weight tests and measured pressure distributions.

KEY WORDS: *discontinuous Galerkin method, finite volume method, high-order scheme*

1. INTRODUCTION

The fuselage aftbody surface of the vehicle, in which the power plant is integrated with the fuselage, is used as the wall of the nozzle with external expansion of the jet [1]. Depending on the flight mode, the various flow patterns are realized in the nozzle with the external expansion wall. At the cruise mode, such an aftbody allows to obtain the additional thrust. The thrust vector is directed straight forward and passes through the aircraft center of mass. However, at the initial flight stages, the expansion wall is the source of drag. At a nozzle pressure ratio corresponding to these flight conditions, the jet has the cell structure, attaches to the expansion wall, and propagates along it (Fig. 1a). The jet overexpansion results in the appearance of areas of negative pressure on the wall. The negative excess pressure on the wall gives rise to the appearance of the down-directed force. The effective thrust vector turns out not to be directed along the aircraft axis, but to be deflected down, which leads to the rise of a pitching moment. Due to the large area of the surface streamlined by the jet, this moment is so significant that it is difficult to counteract it by ordinary control elements. The necessity to find a gas dynamic control methods arises.

In this work, the gas dynamic method of control by means of the injection of additional air through the perforation in the expansion wall is considered. The concept of

(a)

(b)
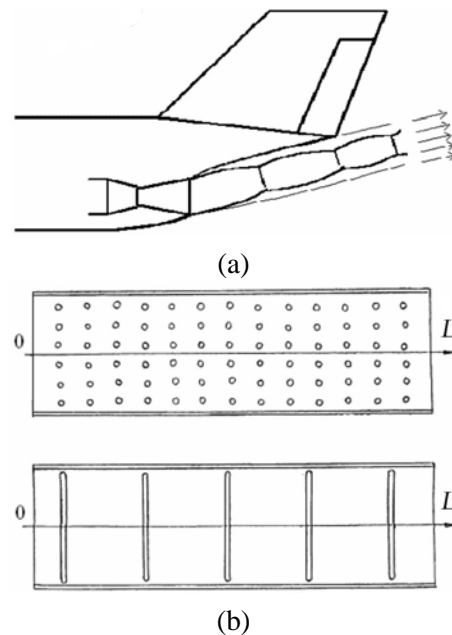
FIG. 1: (a) Flow pattern behind the nozzle at the off-design mode; (b) the expansion wall of the model nozzle with two perforations.

this method is to increase the wall pressure by the injection of additional air in the areas of negative pressure, or to convert the flow from the scheme with the jet attachment to the scheme with the separation of the jet from the wall and to connect the separation area with the ambient. The aim of this work is to estimate the efficiency of this flow control method from the viewpoint of the opportunity to remove the undesirable forces and of the required value of the additional airflow. This work is the extension of the investigations mentioned in Ref. [2].

2. THE MODEL—THE EXPERIMENTAL EQUIPMENT

The model consists of a flat nozzle with rectangular exit section, and of a flat plate adjoining to the long side of the nozzle exit section. The ratio of the sides in the nozzle exit section is 1:6 and the value M_a on the nozzle exit equals 1.9. The half-angle of the supersonic part of the nozzle is 10 deg. The plate of the $20.7h$ length (the height of the nozzle exit section is $h = 10$ mm) simulates the lower surface of the vehicle aftbody. The slope angle of the plate relative to the symmetry horizontal plane is 15 deg. Cutbacks of height $2h$ are installed on each side of the plate along all the length. Two replaceable plates differing by the form of the perforation for the injection of the additional air are used in the experiment (Fig. 1b). The first plate has the perforation of 78 circular holes of the same diameter $0.3h$. The holes are situated in 13 lines, by six holes in a line. The

distance between the lines is $1.5h$, and the distance between the holes in a line is $1h$. The total hole area is 0.92 of the nozzle exit area. The perforation on the second plate consists of five rectangular slots parallel to the long side of the nozzle exit section. The distance from the nozzle exit to the nearest slot is $1.5h$, the distance between the neighboring slots is $4.3h$, and the slot width is $0.2h$. The total perforation slots' area on the first plate is the same as on the second plate. The model structure allows to overlap partially the various perforation areas, and thus to change the place of the additional air injection. The air through the perforations was input normal to the plate surface from the input settling chamber, placed on top of the plate. The model design was presented in Ref. [2].

The experiments were carried out without external flow on the differential rig, equipped by two independent channels of the air input in order to create the main flow through the nozzle and the supplementary one in order to control the flow (Fig. 2a). The differential rig represents the vertical tube, fixed on the strain gauge balance, with the settling chamber as a T-shaped branching at the end. The airflow passes through the strain gauge balance, made in the form of a hollow cylinder, and further along the tube to the settling chamber, from which it goes into two oppositely directed nozzles—the test one and the balance compensated one. The balance nozzle develops the thrust that compensates the thrust of the model nozzle in the absence of the expansion wall. While using this measurement method, even a small change of thrust of the tested nozzle, being due to the influence of the expansion wall, can be measured to a high accuracy. Used as the balance nozzle is the axisymmetric nozzle with $M = 1.9$ on the section. The equality of the thrusts of the test nozzle and of the balance one in the absence of the plate was verified experimentally at all the considered modes. The model was attached to the settling chamber of the differential rig in such a way that the long side of the nozzle section and the plate, simulating the aftbody surface of the vehicle, were situated vertically. In addition, both measured thrust components, directed along and normal to the nozzle, are situated in the horizontal plane. The positive direction of the longitudinal component (forward along the vehicle) means an increase in the thrust of the test nozzle, and the positive value of the transverse component corresponds to the positive lift acting on the aftbody. Presented in Fig. 2b is the photo of the test model, installed on the settling chamber of the differential rig.

While using this technology of the experimental investigation, the loads from the supply channels are not transmitted to the strain gauge balance. However, in the system tube bellows, the "bursting" force arises in the channel of the additional air input. In spite of the fact that this force is directed normal to the plane of the measured forces, it creates the moment in the vertical plane owing to the shift of the tube of the additional air input. This moment influences the balance indications in measuring the longitudinal and transverse forces. The arms, which are affected by this "bursting" force, are by one order less than the arms of the measured longitudinal and transverse forces, but it is necessary to introduce the corrections for its influence. While taking into account the fact that the
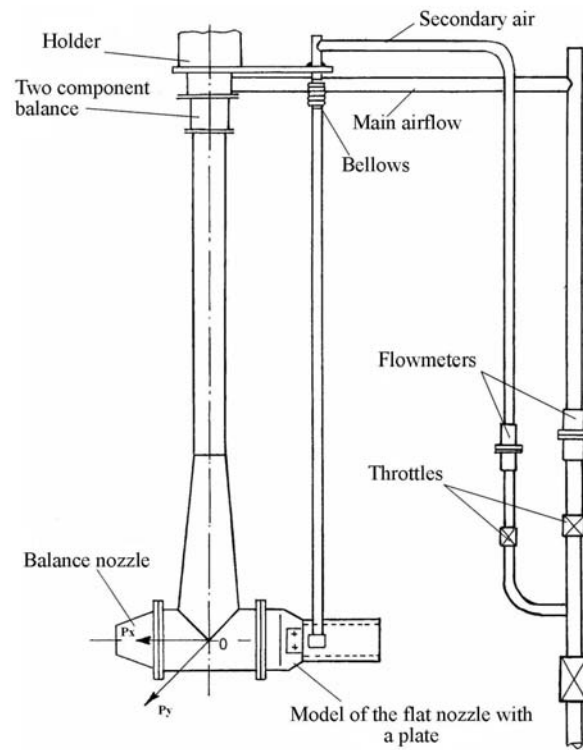
(a)

(b)

FIG. 2: (a) Scheme of differential rig and (b) photo of the model installed on the rig settling chamber.

influence of the bursting force uniquely depends on the pressure in the channel of the additional air input, the allowances were specified based on the balance measurements, performing during the air input through the perforation slots in the plate without the air injection through the test and balance nozzles. The allowances were specified for all the test modes.

The measurements of the pressure distribution along the plate axis were performed on the model along with the balance measurements. The pressure was measured by small indicators, installed directly on the plate.

The experiments with the test model were carried out successively for a range of constant values of the airflow through the main nozzle. At a given airflow through the nozzle, the pressure of the injection was changed discretely from a smaller value to a higher one and the data registration was made at every mode by the measuring-calculating system based on a personal computer.

3. RESULTS OF EXPERIMENTAL INVESTIGATIONS

While presenting the results of the experimental investigations, the following nomenclature was accepted in this work: P_x is the axial component of the total thrust in the layout with the expansion wall, P_y is the force acting on the aircraft layout in the vertical direction, and $\beta = \mathrm{arctg}(P_y/P_x)$ is the angle of the thrust vector deflection. All the forces were related to the thrust of the free nozzle without a plate P_n, which was obtained by calculation by the 1D theory, and the flow of the air, input through the perforation, was related to the flow through the nozzle G_{inp}/G_n. The experiments were carried out at various nozzle pressure ratios p_0/p_a, where p_0 is the total pressure in the settling chamber of the nozzle, and p_a is the ambient pressure. The results of the plate pressure measurements are presented as the distribution of the relative pressure $(p - p_a)/p_a$ along the length of the plate L/h. The distance L is counted off from the leading edge of the plate, adjoining to the nozzle section. The values $\Delta P_x = P_x - P_n$, described the plate influence, which are cited in this paper, are measured directly by the corresponding component of the strain gauge balance. Cited further are the results, allowing us to estimate the operating efficiency of the nozzle with the expansion wall at various methods of additional gas input to the expansion wall.

3.1. Gas Injection to the Expansion Wall with the Perforation of the Circular Holes

The experiments, carried out on this model without the injection of an additional air to the expansion wall, showed that the losses in the axial thrust component P_x could be $\sim 5\%$ of the computational thrust of the isolated nozzle, the vertical component of the effective thrust P_y was negative and in magnitude could be $\sim 24\%$ of the computational thrust, and the angle of the thrust vector deflection β came up to $\sim$ (–14 deg) [2]. Such behavior of the thrust components is associated with the appearance of a number of areas on the expansion wall, the pressure in which is less than the ambient pressure. The last fact can be explained by the overexpansion of the jet, having a cell structure at the considered modes. The longest area of negative pressure is situated directly behind the nozzle exit. The length of the area L depends on the nozzle pressure ratio and varies in the considered range of p_0/p_a as $L/h \sim (p_0/p_a)^{0.7}$ (Fig. 3a). The attempt to boost the
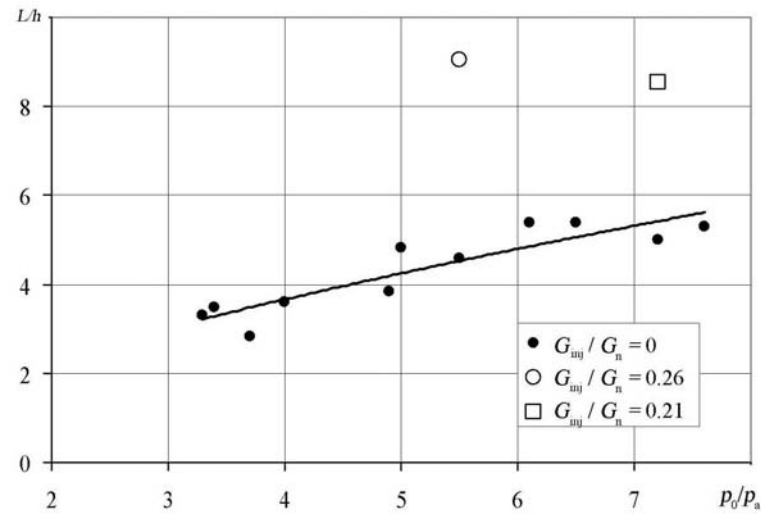
(a)
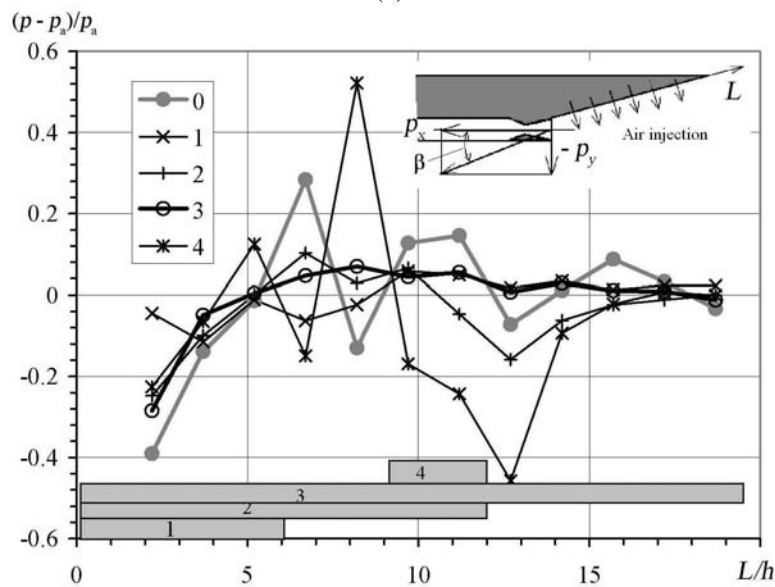
(b)

FIG. 3: Characteristics of the flow near the expansion wall without the injection of an additional air and with a local injection: (a) length of the area of negative pressure on the wall; (b) pressure distribution along the wall.

pressure in this area was made by local air injection through the four perforation lines, which are the nearest to the nozzle. The area of the injection holes in this case was $F/F_\Sigma = 0.3$, where F_Σ is the area of the entire perforation. The local injection raised the pressure in the area of negative pressure; however, it remained lower than the ambient

pressure, and the length of the area itself increased due to the injection. The light points in Fig. 3a illustrate the change in the sizes of the area of negative pressure at local injection of the additional air through the four lines of the holes. The change in the pressure profile along the plate at various injection characteristics can be followed up by the plot in Fig. 3b. The shadowed strips in the field of the plot indicate the length of the injection boundary along the axis L. The notations, accepted in Fig. 3b, correspond to the modes pointed out in Table 1.

The most acceptable pressure profile from all the investigated variants of the injection is realized at the injection through the entire perforation. The fact that the injection through the entire perforation is the most effective is confirmed also by the data of the balance measurements. The values $\Delta P_x, P_y, \beta$, obtained based on the balance measurements, at various modes of the perforation opening are shown in Fig. 4a. (Notations of the points in Fig. 4a correspond to the first three columns of Table 1.) Shown in Fig. 4b are the same values, recorded at the full-open perforation, but at various nozzle pressure ratios. In spite of the positive effect from the air injection to the expansion wall through the circular perforation, the evident shortcoming of this method of the thrust vector control is the necessity of the engagement of a large additional airflow.

3.2. Gas Injection Though the Circular Perforation to the Expansion Wall with the Flap

For the purpose of the possible decrease of the additional airflow, an attempt was made to separate the jet from the expansion wall by installing on it an additional element—the flap. The flap is installed directly behind the nozzle exit section. (In Fig. 5 the flap is highlighted by the dark filling.) The flap surface, adjoining the flow, is parallel to the symmetry plane of the main nozzle flow. Used in the experiment are the flaps of length $l/h = 2.5$ and 5. The transverse size of the flap is equal to the width of the nozzle exit section.

The experiments show that entire separation of the jet flow from the expansion wall did not take place. The thrust losses in the absence of additional airflow through the perforations can increase because of the base drag. However, the injection of additional

TABLE 1: Experimental data.

Mode notation	Injection length L/h	Relative perforation area F/F_Σ	Relative airflow of the injection G_{inj}/G_n	Nozzle pressure ratio p_0/p_a
0	—	—	—	7
1	6	0.3	0.21	7.2
2	12	0.6	0.2	7.6
3	19.54	1	0.21	6.5
4	9–12	0.23	0.39	7
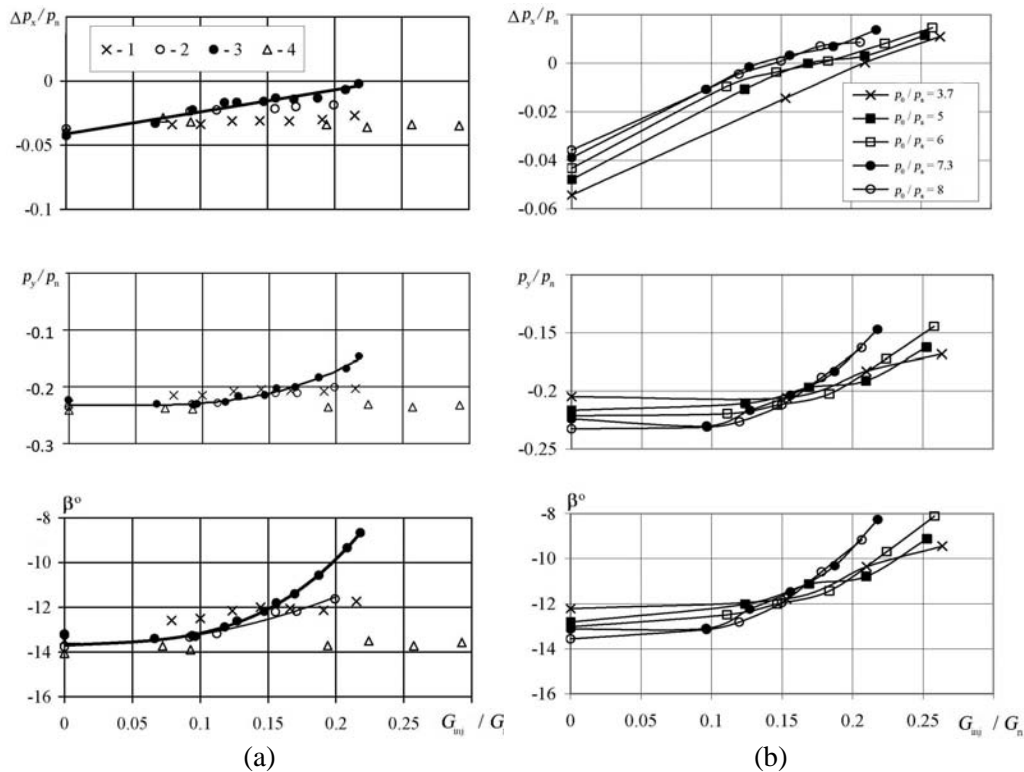
FIG. 4: Characteristics of the nozzle with the expansion wall: (a) at various localization of the injection; (b) at full-open perforation.

air through the perforations, remaining not overlapped by the flap, improves the characteristics of the nozzle with the expansion wall. Presented in Fig. 5 are the data of the characteristics of the nozzle with the expansion wall, on which the flaps of length l/h = 2.5 and 5 are installed. It is seen from the comparison of these data with the data in Fig. 4 that the characteristics of the nozzle with the flap are improved considerably at the equality of the injected airflows. The opportunity to decrease substantially undesirable deviation of the thrust vector at the real flows of the injected air arises. The presence of the flap removes the area of the pressure, being substantially lower than the atmospheric one, on the expansion wall and replaces it by the surface, which does not increase the component P_x, but contributes to the increase of P_y, which is associated with the flow turn toward the horizontal symmetry plane of the nozzle.

4. USE OF THE SLOT PERFORATION IN ORDER TO INJECT THE ADDITIONAL GAS TO THE EXPANSION WALL

Along with the circular perforations, the injection of additional air to the expansion wall through the slot perforations was considered. On the whole, the injection through
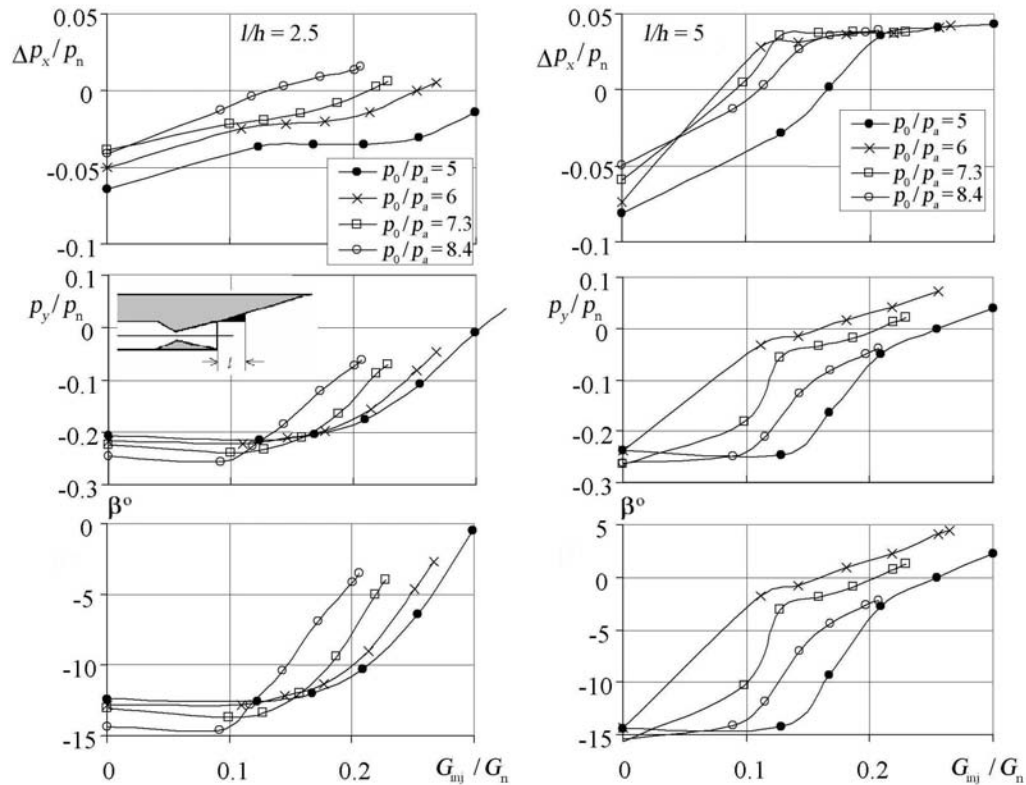
FIG. 5: Influence of the injection of an additional air to the expansion wall of the nozzle with a flap.

the slot perforations is more effective than the injection through the circular ones. As the absolute value of the angle β decreases by the same value, the relative flow of the injected air through the slots turns out to be lower than the flow through the circular holes. However, one does not observe the total neutralization of the negative influence of the expansion wall in this case. The data, obtained at the injection of additional air through the slots, are presented in Fig. 6. The results of the balance measurements are almost the same for the various nozzle pressure ratios within the range of $p_0/p_a = 4 \div 7$.

All the results for the circular and slot perforations mentioned above were obtained at subsonic nozzle pressure ratio drops on the perforations. While going to the supersonic nozzle pressure ratio, one can obtain more effective control. The abrupt increase of the injection effect was obtained, while inputting all the additional flow through one slot, being the closest to the nozzle exit section, at the supersonic nozzle pressure ratio on it (see Fig. 6). The numbers near the points indicate the values of the nozzle pressure ratio at which they were obtained. The increase of the injection effect is observed, starting with the airflow $G_{inj}/G_n \approx 0.1$.
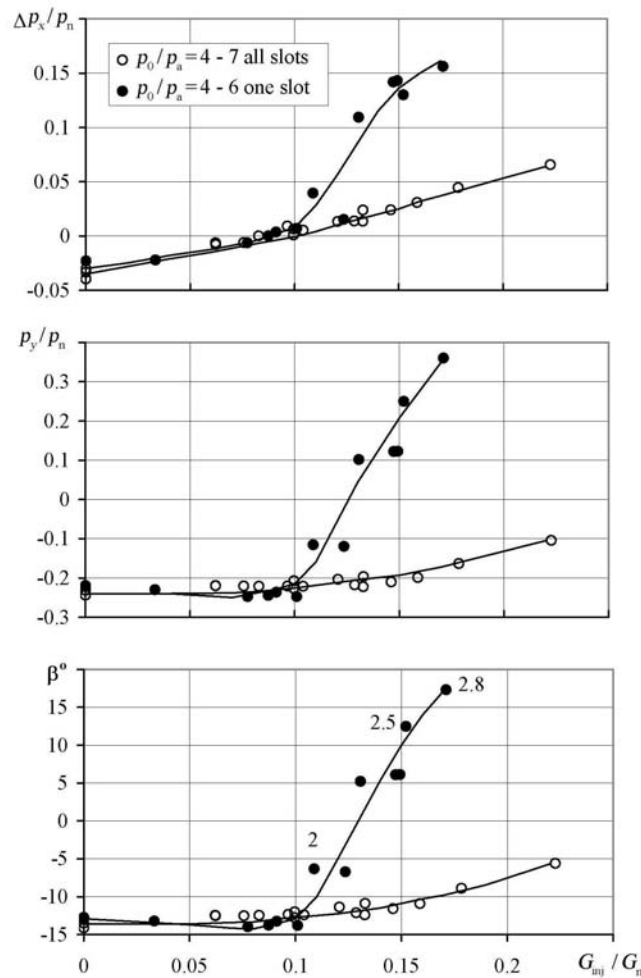
FIG. 6: Characteristics of the nozzle with slot perforations of the expansion wall.

As the measurements show, the pressure distribution along the expansion wall at the injection through one slot equalized and approached the ambient pressure. This fact allows us to draw the conclusion that the propagation of the main flow takes place with the flow separation from the wall. In addition, the positive $\Delta P_x, P_y, \beta$ are explained by the positive additions from the momentum of the jet, flowing out the slot. It should be noted that any increase of thrust is desirable only for the axial thrust component P_x, and the increase of P_y and, correspondingly, of β after their transition through zero will result in the rise of a negative pitching moment. So, one needs to exactly control the injected flow in order to avoid undesirable moments.

Thus, based on the data mentioned above, one can conclude that while using the nozzle with the external expansion wall, there is a possibility of gas dynamic thrust vector

control. Depending on the disposable flow of additional air, one can find an acceptable method of such control.

REFERENCES

1. Zeutzius, M., Beylich, A. E., Matsuo, S., and Setoguchi, T., Experimental investigation of a gas dynamic thrust vector control for hypersonic space planes, *JSME Int. J., Ser. B*, vol. 39, no. 1, pp. 101–111, 1996.
2. Zhirnikov, B. L., Kudin, O. K., and Nesterov, Yu. N., Experimental investigation of the gasdynamic method of the jet flow control, *TsAGI Sci. Trans.*, vol. XXXVII, no. 4, pp. 30–34, 2006.

TsAGI
Sience Journal

CONTENTS OF VOLUME 40

VOLUME 40, NUMBER 3   **2009**

VOLUME 40, NUMBER 4   **2009**

TsAGI
Sience Journal

SUBJECT INDEX TO VOLUME 40

TsAGI
Sience Journal
Author Index to Volume 40

.